

https://dspace.org/

Off-line parameter estimation for unmanned aerial vehicles after loss of control

Moyo, Makhosazana E

2020
https://hdl.handle.net/10539/31246

Downloaded from a DSpace repository. https://dspace.org/

Off-line Parameter Estimation for Unmanned Aerial Vehicles after Loss of Control

Makhosazana. E. Moyo
Student number: 740582

A project report submitted to the Faculty of Engineering and the Built Environment, University of the Witwatersrand, Johannesburg, in partial fulfilment of the requirements for the degree of Master of Science in Engineering.

Johannesburg, October 2020

Declaration

I declare that this project report is my own, unaided work, except where otherwise acknowledged. It is being submitted for the degree of Master of Science in Engineering in the University of the Witwatersrand, Johannesburg. It has not been submitted before for any degree or examination at any other university.

Signed this 21st day of October 2020



Makhosazana. E. Moyo
Student number: 740582

To my parents and sisters who continuously inspire me to pursue my dreams.

Acknowledgements

I would like to express gratitude to my supervisors, Prof Jimoh O. Pedro and Ms Aarti Panday for providing me with good advice, relevant reading material, encouragement and nuggets of wisdom. Their expertise was paramount to the success of this project. Additionally, I would like to thank SITA Air Transport Community Foundation for funding my studies and their unwavering support. This study would not have been possible without their assistance.

Abstract

Unmanned aerial vehicle (UAV) accidents are more prevalent than those in manned aircraft; however, not much work has been done in investigating these accidents. There is a need for the development of an inexpensive accident analysis tool that can be used to estimate UAV parameters before and after loss of control. A MATLAB/Simulink model of NASA's fixed-wing generic transport model (GTM) UAV was used to simulate loss of control and produce sensor data. The unscented and cubature Kalman filters were employed to estimate UAV kinematic and aerodynamic parameters before and after loss of control. Both these non-linear identification techniques adequately reconstructed the flight path of a UAV experiencing loss of control induced by control surface failure and experiencing sensor malfunction. Monte Carlo runs, root mean square errors and hypothesis testing at 5% level of significance revealed that the unscented Kalman filter (UKF) outperformed the cubature Kalman filter (CKF) in tracking the flight path of a UAV experiencing control surface hard-over, jam and float, as well as excessive sensor noise and sensor bias. The cubature Kalman filter however, had better performance under sensor blackout. Both the UKF and CKF successfully predicted all the aerodynamic force and moment coefficients and a majority of control surface deflections behind the loss of control or upset simulated in the MATLAB model. It was concluded that a combination of the flight path reconstruction results, predicted aerodynamic coefficients and estimated control surface inputs can be used to give insights into the reasons behind loss of control. It was determined that the UKF exhibits superior performance when compared to the CKF in systems experiencing excessive noise and highly non-linear environments. Unlike the CKF, the stability of the UKF decreased in situations where there were missing state data, which was the case in sensor blackout. The overall performance of the UKF and CKF was satisfactory, these parameter estimation techniques can be used in accident analysis.

Publications Arising from this Work

The following papers are being prepared from this work:

- Moyo ME, Pedro JO. Parameter Estimation for Sensor Blackout in Unmanned Aerial Vehicles using Cubature and Unscented Kalman filters. In preparation.
- Moyo ME, Pedro JO. Cubature and Unscented Kalman Filters in Control Surface Failure Detection for Unmanned Aerial Vehicles. In preparation.

Table of Contents

Declaration i

Acknowledgements iii

Abstract iv

Publications Arising from this Work v

Contents vi

List of Figures x

List of Tables xiii

List of Acronyms xiv

List of Symbols xv

1 Introduction 1

1.1 Research Background and Motivation 1

1.2 Problem Statement 2

1.3 Literature Review 2

1.3.1 Parameter estimation 2

1.3.2 Loss of control 4
1.3.2.1 Characterising loss of control 5
1.3.3 Unmanned aerial vehicle model 6
1.3.4 Parameter identification techniques 6
1.3.5 Kalman filters 7
1.3.5.1 Unscented and cubature Kalman filters 8
1.3.5.2 Limitations to Kalman filters 9
1.4 Gaps in Existing Literature 9
1.5 Envisaged Research Contributions to Knowledge 9
1.6 Research Objectives 10
1.7 Research Methodology 10
1.7.1 MATLAB/Simulink® model criteria for verification 11
1.7.2 Kalman filters criteria for validation 12
1.8 Research Report Outline 12
2 Aircraft Dynamic and Kinematic Model 14
2.1 Assumptions 14
2.2 Six Degrees-of-Freedom Equations of Motion 14
2.3 Forces and Moments Coefficients for Non-linear Motion 17
2.4 Thrust Model 18
2.5 Atmospheric Disturbance and Turbulence Model 20
3 Implementation of the Mathematical Model and Controller Design 23
3.1 GTM UAV System Parameters 23

3.2 Trim Conditions Prior to LOC . . . 24
3.3 Controller Design . . . 25
3.3.1 Controller justification . . . 25
3.3.2 PID controller model . . . 25
3.3.3 Complete simulink model . . . 27
3.3.4 Controlled behaviour . . . 28
3.4 Sensor Noise . . . 30
4 Kalman Filters . . . 32
4.1 General Kinematic, Input and Output Equations . . . 32
4.1.1 Kinematic and input equations . . . 32
4.1.2 Output equations . . . 34
4.2 Noise Considerations . . . 34
4.3 The Unscented Kalman Filter . . . 35
4.4 The Cubature Kalman Filter . . . 39
4.5 Parameter Estimation . . . 42
5 Verification and Validation of Simulation Model and Kalman Filters . . . 44
5.1 Simulation Model Verification . . . 44
5.2 Simulation Model Validation . . . 49
5.3 Kalman Filter Verification and Validation . . . 51
5.3.1 Flight path reconstruction . . . 51
5.3.2 Reconstruction statistics . . . 51
5.3.3 Kalman filter performance . . . 54

6 Results and Discussion 56
6.1 Induced Sensor Failure 56
6.1.1 Excessive sensor noise 56
6.1.2 Sensor bias 60
6.1.3 Sensor blackout 64
6.2 Induced Control Surface Failure 67
6.2.1 Jammed control surface 67
6.2.2 Control surface hard-over 70
6.2.3 Control surface float 73
6.3 Control Surface Deflection Estimation 76
6.3.1 Jammed rudder control surface 76
6.3.2 Elevator control surface hardover 78
6.3.3 Rudder control surface float 79
7 Conclusions and Recommendations 81
7.1 Conclusions 81
7.2 Recommendations 83
Appendices 84
Appendix 1 84
References 85

List of Figures

1 Reconstructed height of a free falling object 3

2 The generic transport model (GTM) UAV [35]. 6

3 Research approach 11

4 Aircraft body-axes and engine displacements relative to the aircraft cg (adopted from Nguyen et al., [48]). 15

5 Axes and transformation of the engine force and rotor components (adopted from Panday [54]). 15

6 Behaviour of aircraft after experiencing an atmospheric disturbance. 25

7 Schematic of the simulation model. 27

8 An overview of the interconnection of the aircraft model and control channels 27

9 Structure of the elevator control channel 28

10 A comparison of aircraft position, velocity and attitude for trim, disturbed and controlled flight. 29

11 Percentage change in actuator settings required to maintain level flight. . . . 30

12 Actuator settings required to maintain level flight. 31

13 An overview of the unscented Kalman filtering procedure. 39

14 An overview of the cubature Kalman filtering procedure. 42

15 Response to 0.0523rad (3°) elevator step reduction with all other control inputs held unchanged from their trimmed conditions. $\delta_a, \delta_r, \delta_e$ are in rad. 45

16 Response to an aileron doublet with an amplitude of 0.105rad (6°). All other control inputs held unchanged from their trimmed conditions. $\delta_a, \delta_r, \delta_e$ are in rad. 46

17 Response to a 0.105rad (6°) step-up rudder with all the other control inputs held unchanged from their trimmed conditions. $\delta_a, \delta_r, \delta_e$ are in rad. 47

18 Response to a 30% throttle increase with all the other control inputs held unchanged from their trimmed conditions. $\delta_a, \delta_r, \delta_e$ are in rad. 48

19 Quasi-steady push-over pull-up manoeuvre obtained from (a) the GTM UAV simulation model, (b) flight data [25]. 49

20 Time response of a yaw-roll doublet manoeuvre for (a) flight test data [49], (b) the GTM UAV simulation model. 50

21 Flight path reconstruction results for an aircraft experiencing wind disturbance. 52

22 RMSE values obtained for one hundred independent Monte Carlo runs. . . . 53

23 Frequency graph of the RMSE values obtained through the UKF 53

24 Decision criteria for right-tailed and left-tailed hypothesis test. 55

25 FPR results for GTM T2 UAV with wind disturbance and a 5% sensor error. 56

26 ARMSE for different n number of independent Monte Carlo runs with random noise functions, w and v at 0%, 2%, 5% and 10% sensor error budgets. 57

27 The RMSE values for fifty Monte Carlo runs with random noise functions w and v, and 5% sensor error budget. 58

28 Measured pitch rate with and without $0.01^o s^{-1}$ sensor bias. 61

29 Flight path reconstruction results for a GTM experiencing a $0.01^o s^{-1}$ sensor bias in the pitch rate measurement. 61

30 The RMSE for fifty Monte Carlo runs with random noise functions w and v, and a $0.01^o s^{-1}$ pitch rate bias. 62

31 FPR for an aircraft experiencing a GPS outage between $t = 40s$ and $t = 90s$. 64

32 The reconstructed results for the x state. 65

33 The state RMSE values for the GTM T2 UAV experiencing sensor blackout. . 65

34 FPR results for a UAV experiencing a $\delta_r = 10^o$ rudder deflection at time t= 20s 67

35 Reconstruction of the position of a UAV experiencing a $\delta_r = 10^o$ rudder deflection. 68

36 RMSE values for the GTM T2 UAV experiencing a a $\delta_r = 10^o$ rudder deflection. 68

37 Flight path reconstruction for an aircraft experiencing a 20° elevator hardover. 70

38 RMSE values for a GTM T2 UAV experiencing 20% elevator hardover. 71

39 Elevator, aileron, and ruder input disturbance applied in the simulation model. 73

40 Coupled rudder and aileron surface deflection resulting from a rudder float. . 74

41 FPR results for a GTM T2 UAV experiencing wind disturbance and a rudder float with a maximum amplitude of 10°. 74

42 Position of the GTM T2 UAV experiencing wind disturbance and a rudder float with a maximum amplitude of 10°. 75

43 Force and moment coefficients in the body-axes frame for a 10° rudder deflection. 77

44 Control inputs for a 10° rudder deflection. 77

45 Control inputs for a 10° jammed aileron input. 78

46 Force and moment coefficients in the body-axes frame for a 20° elevator hardover. 78

47 Control inputs for a 20° elevator hardover. 79

48 Force and moment aerodynamic coefficients in the body-axes frame for rudder float. 79

49 Control inputs for rudder float. 80

List of Tables

1 The engine specifications for a Jetcat P70 turbofan engine 19

2 Scale factors used in the dynamic scaling of the GTM UAV 19

3 Values of $V_{w|h=6m}$ for different turbulence levels [59] 22

4 Parameters of the GTM T2 UAV, adapted from Grauer and Morelli [60]. . . 23

5 Range for the control inputs 24

6 Trim conditions 24

7 Controller gains for the PID control law 26

8 Measurement resolutions for different error budgets; adopted from Grauer and Morelli [60] 31

9 Trim states used for the model verification process 44

10 Hypothesis tests comparing UKF and CKF performance for 0% sensor noise. 55

11 ARMSEs for n=50 and n=100 independent Monte Carlo runs for the GTM T2 UAV experiencing 0%, 2%, 5% and 10% sensor errors. 58

12 Hypothesis tests comparing UKF and CKF performance over fifty Monte Carlo runs for 5% sensor noise. 59

13 ARMSEs for n=50 and n=100 independent Monte Carlo runs for a GTM UAV with sensor bias. 62

14 Hypothesis tests comparing UKF and CKF performance over fifty Monte Carlo runs for sensor bias. 63

15 Hypothesis tests comparing UKF and CKF performance over fifty Monte Carlo runs for sensor blackout. 66

16 ARMSEs for n=50 and n=100 independent Monte Carlo runs for a GTM UAV experiencing GPS sensor blackout 66

17 Hypothesis tests comparing UKF and CKF performance over fifty Monte Carlo runs for a jammed rudder deflection of 10%. 69

18 ARMSEs for fifty Monte Carlo runs for a jammed surface deflection of 10° . 69

19 Hypothesis tests comparing UKF and CKF performance over fifty Monte Carlo runs for an elevator hardover of 20%. 72

20 ARMSEs for n=50 independent Monte Carlo runs for control surface hardover. 73

21 ARMSEs for n=50 independent Monte Carlo runs for floating control inputs δ_e, δ_a and δ_r 75

22 Trim states used for the model verification process 84

List of Acronyms

Acronyms	Description
ANN	Artificial neural network
ARMSE	Accumulated root mean square error
AvSSP	Aviation safety and security program
CKF	Cubature Kalman filter
DE	Differential evolution
DOF	Degrees-of-freedom
EKF	Extended Kalman filter
FPR	Flight path reconstruction
ICAO	International Civil Aviation Organisation
GA	Genetic algorithms
GPS	Global positioning system
GTM	Generic transport model
HIV	Human immunodeficiency virus
LOC	Loss of control
PID	Proportional-integral-derivative
PDF	Probability density funtion
PSO	Particle swarm optimisation
RPM	Revolutions per minute
RMSE	Root mean square error
UAV	Unmanned aerial vehicle
UKF	Unscented Kalman filter
UT	Unscented transformation

List of Symbols

Symbol	Description
a_x, a_y, a_z	Body-axes accelerations $[m.s^{-2}]$
a_n, b_n, c_n, d_n, e_n, f_n	Coefficients of aerodynamic force and moment coefficient equations [-]
b	Wing span [m]
$\bar{c}$	Mean aerodynamic chord [m]
cg	Centre of gravity [-]
C	Operational envelope
C_l	Aerodynamic rolling moment coefficient about the x-body axis [-]
C_m	Aerodynamic pitching moment coefficient about the y-body axis [-]
C_n	Aerodynamic yawing moment coefficient about the z-body axis [-]
C_x	Force coefficient, along the x-body axis [-]
C_y	Force coefficient, along the y-body axis [-]
C_z	Force coefficient, along the z-body axis [-]
$\mathbf{e}_i, \mathbf{e}_{i-1}$	Generators [-]
$\|e_k^n\|$	Absolute state error [-]
$f()$	State function
g	Acceleration due to gravity $[m.s^{-2}]$
G_{act}	Transfer function for actuator dynamics [-]
G_{eng}	Transfer function for throttle dynamics [-]
h	Altitude [m]
$h()$	Observation function
H_u, H_v, H_w	Dryden wind model translational transfer functions [-]
H_p, H_q, H_r	Dryden wind model rotational transfer functions [-]
I_T	Engine spinning rotors moment of inertia $[kg.m^2]$
I_{xx}, I_{yy}, I_{zz}	Roll, pitch and yaw moments of inertia $[kg.m^2]$
I_{xz}, I_{xy}, I_{yz}	Products of inertia $[kg.m^2]$
$J(X_n)$	Jacobian [-]
$k-1$, k, $k+1$	Corresponding filter steps [-]

K	GTM scaling factor [-]
K	Number of Kalman filter steps [-]
K_{a_*}	Aileron channel gains [-]
K_{e_*}	Elevator channel gains [-]
K_{r_*}	Rudder channel gains [-]
K_{T_*}	Thrust channel gains [-]
L	Length dimension [-]
L	Length of state vector [-]
L_u	Dryden wind model scale length of u_w [-]
L_v	Dryden wind model scale length of v_w [-]
L_w	Dryden wind model scale length of w_w $[m]$
m	Aircraft mass $[kg]$
M	Mass dimension [-]
M_r	Rank mean [-]
N	Number of Monte Carlo runs [-]
n	Monte Carlo run [-]
n_1, n_2	Sample size [-]
p	Aircraft roll rate $[^\circ s^{-1}]$
p_w, q_w, r_w	Rotational wind fluctuations $[^\circ s^{-1}]$
P_k	State covariance vector [-]
P_k^a	Augmented state covariance vector [-]
P_0	Initial covariance estimate [-]
Q_k	Process noise covariance vector [-]
$\bar{q}$	Dynamic pressure $[Nm^{-2}]$
q	Aircraft pitch rate $[^\circ s^{-1}]$
r	Aircraft yaw rate $[^\circ s^{-1}]$
R_k	Measurement noise covariance vector [-]
R_1	Sum of ranks for sample 1 [-]
s	Standard deviation [-]
s_{act}	Actuator transfer function root [-]
s_{eng}	Engine transfer function root [-]
S	Wing reference area $[m^2]$
t	Time $[s]$
T	Thrust $[N]$
T	Time dimension [-]
u	Aircraft translational velocity in the X direction $[ms^{-1}]$
u_w	Translational wind speed in the X direction $[ms^{-1}]$
$\mathbf{u}$	Input vector [-]

v	Aircraft translational velocity in the Y direction $[ms^{-1}]$
v_w	Translational wind speed in the Y direction $[ms^{-1}]$
$\mathbf{v}$	Measurement noise vector [-]
V	Total airspeed $[ms^{-1}]$
V_A	Total aerodynamic velocity $[ms^{-1}]$
V_o	Absolute velocity vector $[ms^{-1}]$
V_w	Wind speed $[ms^{-1}]$
w	Aircraft translational velocity in the Z direction $[ms^{-1}]$
$\mathbf{w}$	Process noise vector [-]
w_k	Random fluctuations in Markov process [-]
w_w	Translational wind speed in the Z direction $[ms^{-1}]$
W_x	X wind velocity component in the body-axes reference frame $[ms^{-1}]$
W_y	Y wind velocity component in the body-axes reference frame $[ms^{-1}]$
W_z	Z wind velocity component in the body-axes reference frame $[ms^{-1}]$
x	Aircraft position in the X direction $[m]$
x_{cg}	Centre of mass position $[m]$
x_k^a	Augmented state vector [-]
$\hat{x}_k$	A *posterior* state [-]
$\bar{x}$	Sample mean [-]
$\mathbf{x}$	State vector [-]
$x_\circ$	Initial state vector [-]
x_T	X-coordinate of the engine position with respect to the cg $[m]$
X_n, X_{n+1}	Consecutive Newton-Raphson iterations
y	Aircraft position in the Y direction $[m]$
$\hat{y}_k$	Updated observation vector [-]
$\mathbf{y}$	Observation vector [-]
y_T	Y-coordinate of the engine position with respect to the cg $[m]$
z	Aircraft position in the Z direction $[m]$
z_k	Measured output values [-]
z_T	Z-coordinate of the engine position with respect to the cg $[m]$
Z	Test statistic [-]

Greek Symbols

α	Angle of attack [°]
α	UKF primary scaling parameter [-]
α_1	Kurtosis coefficient [-]
α_2	Skewness coefficient [-]
β	Sideslip angle [°]

β	UKF secondary scaling factor [-]
δ_a	Aileron deflection [°]
δ_e	Elevator deflection [°]
δ_r	Rudder deflection [°]
δ_T	Throttle deflection [-]
δ_{Tmax}	Maximum throttle deflection [-]
η	Unscented Kalman filter weight vector [-]
κ	Tertiary scaling parameter [-]
λ	Scaling parameter [-]
γ	Flight path angle [°]
ω_T	Engine angular speed $[rads^{-1}]$
Ω_o	Angular velocity vector $[^\circ s^{-1}]$
Ω_w	Wind velocity vector $[^\circ s^{-1}]$
θ_k	Markov process noise parameter [-]
ξ_i	Cubature points [-]
ϕ	Roll angle [°]
θ	Pitch angle [°]
θ_r	Rank standard deviation [-]
ψ	Yaw angle [°]
ψ^i	Transformed sigma points [-]
ψ_w	Wind direction [°]
$\vartheta_{TY}, \vartheta_{TZ}$	Angular orientation of engine [°]
ρ	Air density $[kg.m^{-3}]$
ρ_0	Air density at sea level $[kg.m^{-3}]$
σ_u, σ_v	Dryden wind model turbulence intensities [-]
σ_w	Dryden wind model turbulence intensity $[ms^{-1}]$
τ	Time constant [s]
τ_a	Aileron actuator time constant [s]
τ_e	Elevator actuator time constant [s]
τ_k	Correlation time [s]
τ_r	Rudder actuator time constant [s]
τ_T	Thrust actuator time constant [s]
χ	Sigma-points vector [-]

1 Introduction

1.1 Research Background and Motivation

Unmanned aerial vehicle (UAV) accidents are more prevalent than those in manned aircraft [1, 2]; however, not much work has been done in investigating these accidents. Investigating UAV accidents may not be seen as a worthwhile exercise because the cost of UAVs is much less than that of manned aircraft and most UAV accidents do not result in loss of life [3, 4]. This has led to most UAV accident causes being classified as unknown [2]; adversely compromising safety in UAVs. Increasing the safety and reliability of UAVs will see them reach their full potential in the aviation industry [3, 5, 6, 7].

Most aircraft accidents are caused by loss of control [8, 9, 10, 11, 12]. There is a need for the development of an inexpensive accident analyses tool that can be used to determine UAV parameters at the point of loss of control. Parameter estimation has been used as a tool in accident analysis of manned aircraft for decades [13, 14, 15]. In this study, this tool will be employed to determine UAV aerodynamic parameters after loss of control.

UAV safety is a matter of concern. A poor safety record has restricted UAVs from reaching full potential [2, 3]. Accident analysis is an integral part of improving the safety record of any aircraft. Parameter estimation is a commonly used accident analysis tool. Not all aerodynamic and flight dynamic parameters are recorded during flight. This becomes a challenge when one has to reconstruct the aircraft behaviour after an upset has occurred. Modern day commercial aircraft have on-board sensors that record approximately 88 parameters, this is in stark contrast with the average 11 recorded by UAVs [15]. Due to payload requirements and cost constraints, there is a restriction to the number of on-board sensors in UAVs [16]. As such, there is a need for a tool to estimate unknown parameters from recorded ones.

Many UAV designers are resorting to using low-cost sensors in an effort to reduce cost. Low-cost sensors often suffer from blackouts, inaccuracies, high sensitivity to noise, low precision and degraded performance [17]. In extreme circumstances sensor malfunction may initiate loss of control [18]. Parameter estimation becomes a crucial tool to filter noise, and interpolate or extrapolate unknown values in sensor data. Identification techniques are used to infer unknown parameters from noisy, incomplete, inaccurate and uncertain measured data. Knowing the flight dynamic and aerodynamic parameters of the UAV before and after an upset has occurred will give insights into the causes of loss of control. If the reasons for accidents are known, steps can be taken to reduce reoccurrence [5]. Accident analysis warrants attention because recommendations from investigations play a pivotal role in aircraft regulation. This can be seen from how civil aviation regulations have advanced as a result of

recommendations given by accident investigators [3]. The same process is vital for UAVs to reach full potential.

1.2 Problem Statement

Not much work has been done in UAV accident investigations [2]. Accident analysis tools like parameter estimation have not been sufficiently developed to account for the non-linear and unstable nature of UAVs. Most parameter estimation tools are not valid for extremely non-linear and unstable UAV flight after loss of control [14, 19, 20]. There is little evidence that recently developed non-linear parameter estimation techniques have been used to determine UAV parameters after loss of control. This study will investigate how parameter estimation for highly non-linear and unstable UAV flight after loss of control can be achieved using recently and earlier developed non-linear identification techniques.

1.3 Literature Review

The use of UAVs in military and civil aviation has expanded drastically in the past decade. The driving factor for this growth is that UAVs can be used for dangerous, dirty, and mundane jobs [3, 5]. Despite this growth, a poor safety record has hindered UAVs from reaching full potential [3]. UAVs are more likely to be involved in accidents than manned aircraft; yet not much work has been done in investigating these accidents [2]. Parameter estimation is a tool that has been used in accident analysis for manned aircraft [13]. For the present work, the use of parameter estimation in UAV accident analysis will be investigated. In this section parameter estimation, loss of control as a factor in UAV accidents and non-linear identification techniques used to achieve the former will be described.

1.3.1 Parameter estimation

In off-line parameter estimation, unknown aircraft parameters that are not directly measured in flight are inferred from available recorded data post-flight. This data may be riddled with sensor noise and inaccuracies. Typical on-board sensors for UAVs are gyroscopes, accelerometers, barometers and GPS, more recently IMUs and magnetometers [21, 22]. Gyroscopes measure angular rates (p, q, r), accelerometers measure linear acceleration (a_x, a_y, a_z), whilst the barometer gives the altitude h. GPS gives position and velocity measurements with respect to the Earth. Identification techniques combine these measured parameters with dynamic and kinematic equations of the system to determine unknown parameters for different system inputs. It should be noted that there is no recorded sensor data available for

this study. As such, a MATLAB/Simulink® model simulating UAV motion will be used to produce the measured data.

Mulder et al., [13] described a two-step method for parameter estimation. The first step is flight path reconstruction. During this step, the time history of the aircraft state is determined from noisy, uncertain, incomplete and inaccurate sensor data using identification techniques. In the second step, unknown parameters are calculated from the respective full state vector at the time of interest using aerodynamic, kinematic and dynamic equations. Figure 1 shows the reconstructed height of a free falling object. The flight path was reconstructed from noisy and incomplete sensor data. In cases of missing data, unknown parameters are estimated using the latest known measurement [23]. This measurement is extrapolated to give the most probable parameter values for the sensor blackout period.

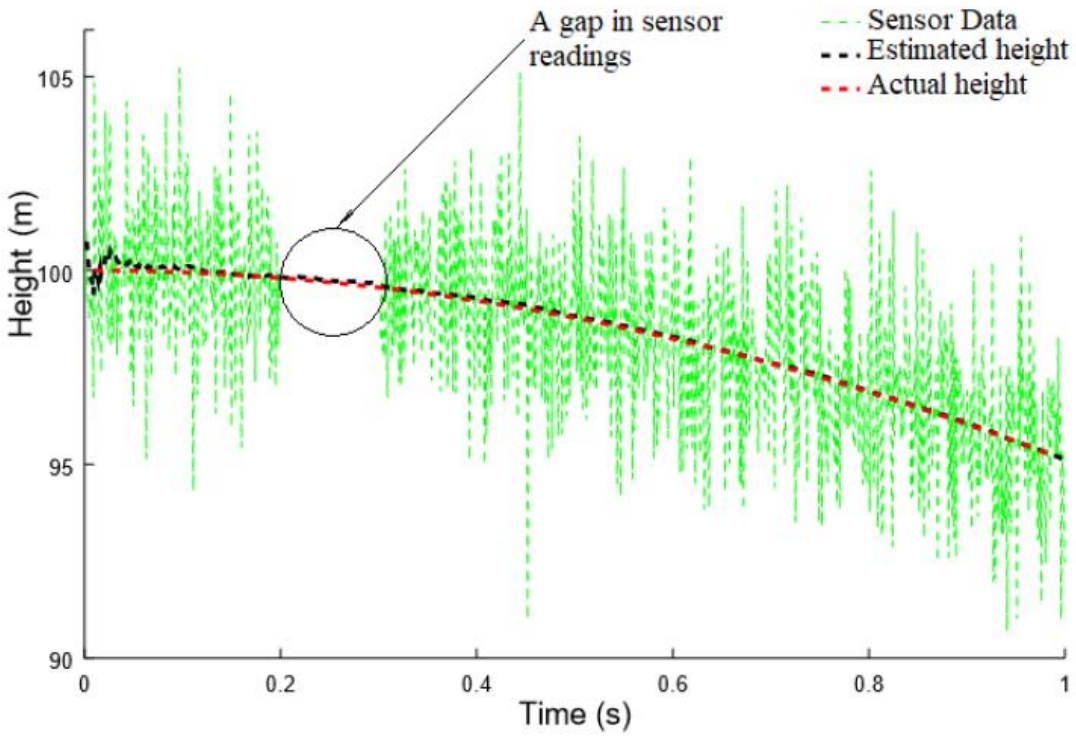

Figure 1: Reconstructed height of a free falling object

One of the earliest attempts of parameter estimation was done by Eulrich and Rynash [24]. They successfully determined aerodynamic control parameters of an F-4E aircraft using the iterated Kalman method. Many other researchers achieved the same fit for different aircraft using various identification techniques [14, 21, 25]. Although these studies adequately estimated manned aircraft parameters, the dynamic and kinematic equations used fall short when applied to UAVs in loss of control (LOC) [14, 19, 20]. The dynamic and kinematic equations used in [24] are linearised about nominal flight conditions. These equations do not cater for

the highly non-linear, coupled and asymmetric UAV after loss of control (LOC). Wind turbulence was also neglected for parameter estimation in manned aircraft, these effects cannot be ignored for the smaller UAV [19, 26].

More recently researchers have performed parameter estimation on UAVs [19, 25, 26]. In these studies wind turbulence effects were considered. Borup et al., [26] in particular showed how the Dryden wind turbulence simulator can be applied to UAV simulations. These researchers showed that the various identification techniques produce good parameter estimates when compared to actual flight data. Padayachee [25] used identification techniques to determine the non-linear aerodynamic parameters of a UAV. In his work, he compared his results to wind tunnel test data which he provided. This wind tunnel test data can be used to verify the MATLAB/Simulink® model and the identification techniques to be used in parameter estimation.

1.3.2 Loss of control

Most aviation accidents occur as a result of control loss [8, 9, 11, 12, 27]. Loss of control (LOC) occurs when the aircraft departs from the normal flight envelope [27]. Causes of LOC may be human error, external disturbances, structural failure, malfunctions in control, sensor and propulsion systems. These causes may happen independently or in combination. LOC is characterised by oscillatory motion, coupling of longitudinal and lateral-directional motion, high angular rates and asymmetric flight [28]. The system dynamics are highly non-linear and unstable after LOC. Coupling of longitudinal and lateral-directional motion will increase the number of unknown parameters, this may lead to a collapse of the identification technique [19, 24]. High angular rates may lead to short durations where the general dynamic, kinematic and aerodynamic equations are not valid [24]. As such there is a need for non-linear dynamic and kinematic equations that are true for larger flight regimes. These equations must accommodate asymmetric motion.

Sensor failure has led to the loss of several manned aircraft in history, the same can be said for UAVs [18]. Correct sensor operation is critical to UAV flight missions [19]. Excessive biases, inaccuracies, gaps in information as well as drift are some forms of sensor malfunction [17, 18]. If fault-tolerant control is not employed in a system, a malfunctioning sensor will continue sending feedback to the flight controller. The controller will in turn relay incorrect signals to actuators. This may affect control surface deflection and propulsion systems; inevitably compromising aircraft stability. For example if there is a 0.1 rad/s drift surge in the roll rate gyro, an aileron deflection will be employed to counter this non-existent change in roll rate. In a few seconds the UAV will be plunged into an uncontrollable roll.

Failure in control surfaces can be characterised by surface float, hard-over, lock-in-place and loss of effectiveness [18]. Float occurs when the control surface freely rotates without any input. Hard-over occurs when the control surface is jammed at the maximum angle of deflection, whilst in lock-in-place, the control surface is jammed at any angle of deflection less than the maximum. Loss of effectiveness occurs when the control surface is exposed to downwash that prevents it from carrying out its function. This study will focus on LOC caused by float, hard-over and lock-in-place because aircraft designers usually design against loss of effectiveness. There are many reasons that may be behind control surface failure. These reasons include leaks in hydraulic systems, electronic and controller failure. These different reasons of failure will not be modelled in the MATLAB/Simulink® model, only the end effect of control surface failure will be taken into consideration.

1.3.2.1 Characterising loss of control

Given that loss of control is a vital part of this study, it has to be fully defined. A general definition of loss of control is the significant departure of the aircraft from the flight envelope. In a study by Wilborn and Foster [29], loss of control was quantified using 2D parameter spaces. The authors used 5 flight envelopes to classify loss of control. The same envelopes are used to specify loss of control in this study. These flight envelopes are [29]:

1. Adverse aerodynamic envelope: parameters are angle of attack vs sideslip angle.
2. Unusual attitude envelope: parameters are bank angle vs pitch angle.
3. Structural integrity envelope: parameters are normal load factor vs normalised air speed.
4. Dynamic pitch control envelope: parameters are dynamic pitch attitude ($\theta + \dot{\theta} \triangle t$) vs percentage pitch control command.
5. Dynamic roll control envelope: parameters are roll attitude ($\phi + \dot{\phi} \triangle t$) vs percentage lateral control command.

Kwatny et al., [30] used simulations and wind tunnel tests to model loss of control, whilst Murch and Foster [31] modelled loss of control through simulations. Both studies used the adverse aerodynamic and the unusual attitude envelope to define loss of control. Kwatny et al., [30] defined a flight envelope as a set of state constraints and provided the operational envelope for the GTM UAV:

$$C = \left\{(V, \gamma) | 27ms^{-1} \leq V \leq 73ms^{-1}, -22^{\circ} \leq \gamma \leq 22^{\circ}\right\},$$

where V and γ are the airspeed and flight path angle respectively. Wilborn and Foster [29] made an observation that vehicle upset is usually a feature of loss of control. They identified the following five vehicle upset events: abnormal attitude, velocities, flight trajectory, uncontrolled descent and stall. These definitions and envelopes will be used in this study to identify the point of loss of control.

1.3.3 Unmanned aerial vehicle model

The use of UAVs has grown in both the civil and military aviation. UAV accidents are not subject to much scrutiny because most of these accidents do not result in loss of human life [2]. Some work has been done in loss of control prevention and recovery, notably by NASA's Aviation Safety and Security Program (AvSSP) [9, 11, 27, 32]. Researchers in this program developed a 5.5% dynamically-scaled version of a large full-scale civil transportation jet [33] called the NASA generic transport model (GTM) UAV. This UAV will be used in this study. It is a fixed-wing, twin-turbine UAV. It has been used by several UAV researchers [32, 34, 35]. There is substantial published geometrical, flight test and wind tunnel data on the GTM UAV. Kwatny et al., [30] and Gill et al., [36] provided trim conditions of the GTM UAV obtained through MATLAB/Simulink®. Non-linear simulations of the GTM UAV are available in the public domain [35]. Figure 2 shows the generic transport model (GTM) that will be used during this study.



Figure 2: The generic transport model (GTM) UAV [35].

1.3.4 Parameter identification techniques

Numerous parameter estimation methods have been developed by researchers over the past decades. The most common of these are the artificial neural network (ANN)-based methods, output error method, filtering approach and equation error methods [37]. Pispitsos et al., [15] successfully used the artificial neural network-based method to determine the surface

control deflections of an F-16 after an air crash. Despite their success in using the ANN-based method as an accident analysis tool, the ANN-based method needs to be trained with previously available flight data prior to it being used as an identification tool [15]. The ANN-based method has to be trained with this data before recorded data from the crashed aircraft can be analysed. The performance of the ANN-based method hinges on the quality and quantity of the previous flight data. Given the variety of UAVs in industry, it is impractical to use the ANN-based method in this study. Though the research by Pispitsos et al., [15] will not be directly applicable to the current study, it shows that it is possible to retrieve unmeasured parameters from measured data using identification techniques after an air crash.

The output error method has been used by some researchers [20, 38]. This method produces adequate and accurate results for the flight state vector, however it assumes no system noise [13]. Wind turbulence effects are considered as system noise. It has already been established in Section 1.3.1 that wind turbulence effects cannot be ignored when dealing with UAVs. Over and above this, the output error method is better suited to estimate parameters for stable flight. As a result, the output error method is not considered appropriate for this study. On the other hand, filtering approaches like the Kalman filter are suitable for less stable flight. Kalman filters account for both process and measurement noise including wind turbulence [13]. Kalman filters have been proven to give accurate results in previous work, as such they will be the identification technique of choice in this study.

1.3.5 Kalman filters

The use of Kalman filter methods in parameter estimation has been extensively studied over the past decades [13, 20, 25, 39]. Kalman filters are optimal estimators that can be used to identify parameters from noisy, inaccurate, incomplete, uncertain and indirect sensor measurements. There are many variations of the Kalman filter, the most prominent is the Extended Kalman Filter (EKF) [17, 40, 41]. It deals with non-linear systems by linearisation about a local point. This variation of the Kalman filter is versatile, computationally efficient and easy to implement. However, it collapses if the system is highly non-linear, unstable and if initial measurements are far from correct values [17]. It also diverges if there are too many unknown parameters [41]. The presence of a large number of parameters for non-linear UAV motion after LOC cannot be avoided, as such the EKF is not suitable for this study.

Researchers have made extensions to the Kalman filter method in order to address the problem of divergence and collapse when working with non-linear and unstable systems. The unscented Kalman filter (UKF) and cubature Kalman filter (CKF) are products of this research [15, 40, 42]. Rigatos [41] used the EKF, UKF and CKF in parameter estimation for UAVs. He observed that the UKF is more accurate than EKF in all cases. There are other

researchers who have reached the same conclusion [23, 43]. Teixeira et al., [43] showed that the UKF is less prone to noise when compared to the EKF. Rigatos [41] also showed that the CKF converged 20% faster than the UKF. In some cases CKF produced improved estimations when compared to the UKF. Both UKF and CKF are less likely to diverge when dealing with highly non-linear systems. Arasaratnam [42] asserts that the CKF will not collapse when the number of unknown parameters increases. Given the performance of the UKF and CKF when dealing with non-linear systems and a large number of parameters, these identification techniques will be used to estimate UAV parameters after loss of control in this work.

1.3.5.1 Unscented and cubature Kalman filters

As discussed above, the unscented and cubature Kalman filter methods will be used to estimate parameters of a UAV after loss of control has occurred. Although these methods carry out parameter estimations in different ways, both algorithms are based on the classical Kalman stochastic equations. The initial starting point for both methods is:

$$x_k = f(x_{k-1}, u_{k-1}) + w_{k-1}, \tag{1.1}$$

$$y_k = h(x_k) + v_k, \tag{1.2}$$

$$with\ k = 1, \ldots, N\ ,$$

where x_{k-1} and x_k represent the full aircraft state vector at the k-1th and kth time step respectively; u_{k-1}, y_k, w_{k-1} and v_k are the control input, observation vector, process and observation noise respectively. The variable $f()$ represents the set of equations that govern the motion being investigated; whilst, $h()$ is the system of equations relating the state vector and observation vector. The identification techniques will give the time history of the full aircraft state vector. The full state vector of the UAV is:

$$x = [V, \beta, \alpha, p, q, r, \phi, \theta, \psi, x_i, y_i, z_i],$$

where β and α are the sideslip angle and angle of attack, and p, q and r are angular rates. ϕ, θ and ψ are Euler angles that describe the aircraft attitude, and x_i, y_i, and z_i give the position of the UAV. Aerodynamic equations will be used to determine other unknown parameters like control inputs, forces and moments. These parameters will give a clearer picture of the UAV motion prior and after loss of control; suggestions of what caused loss of control can then be made.

1.3.5.2 Limitations to Kalman filters

The underlying assumption of all Kalman filters is that the noise distribution is Gaussian [13, 25, 39]. It is also assumed that the noise is white. In real applications the noise probability density function (PDF) may not follow a Gaussian distribution especially for non-linear flight. Given that there are several sources of noise; noise intensity may be different over a range of frequencies, making the white noise assumption invalid. In the unscented Kalman filter, a set of sigma points are constructed. These points capture the true process and observation distributions [44]. Similarly in the cubature Kalman filter, cubature points represent the distributions more accurately.

If results from the Kalman filters are not satisfactory, applying smoothers or iterated filter algorithms will improve these results [43]. Employing a smoothing step in the reverse direction of any Kalman filter may result in more accurate estimates [13]. Smoothing, which is also known as interpolation can be applied iteratively until a minimum error requirement has been satisfied [45, 46]. Iterated filter algorithms improve Kalman filter results by applying local iterations for each Kalman filter step.

1.4 Gaps in Existing Literature

The following gaps in literature have been identified;

a. Little work has been done in using the cubature Kalman filter for parameter estimation in UAVs.

b. Though the unscented Kalman filter has been used in parameter estimation for UAVs, none of the studied works used the UKF in parameter identification after loss of control.

c. There is little evidence that parameter estimation has been used to determine the causes of UAV failure.

1.5 Envisaged Research Contributions to Knowledge

This study will investigate the use of the unscented Kalman filter as well as the recently developed cubature Kalman filter in parameter estimation of a UAV after loss of control. After the completion of this study the following contributions to knowledge are expected:

- An inexpensive accident analysis tool will be available for UAV accident investigators.

- When utilised correctly this tool will help designers improve UAV safety features, hence reducing the occurrence of future accidents.
- Recommendations from accident investigators will help improve UAV regulation from its current uncertain state to a state similar to that of manned aircraft.

These contributions will see UAVs used in more roles than at present.

1.6 Research Objectives

The objectives of this research are to:

a. Determine how the flight path of a UAV that has experienced loss of control can be reconstructed.

b. Establish how results obtained in flight path reconstruction can be used to give insights into reasons behind the loss of control.

c. Assess the stability and performance of the parameter identification techniques.

1.7 Research Methodology

To adequately address the research objectives, both the unscented and cubature Kalman filters will be used to determine unknown parameters from measured data, kinematic and dynamic equations. In order to capture the unstable and non-linear nature of UAV motion, non-linear equations of motion will be derived. These equations will account for asymmetric flight. Ouellette [8], Arruda [47], Nguyen et al., [48] derived dynamic and kinematic equations for asymmetric flight. These equations will be used in this study.

There is no sensor data available for a UAV that has experienced LOC in this study. As such, a MATLAB/Simulink® model will be used to simulate the response of a UAV before and after loss of control. This model will provide the measured data. Typical UAV sensors give measurements for angular rates (p, q, r), linear acceleration (a_x, a_y, a_z), altitude h, the velocity and position of a UAV with respect to the Earth (V_E, x_E, y_E, z_E). The unscented and cubature Kalman filter methods will then be used to estimate parameters of a UAV before and after loss of control has occurred. Suggestions to the causes of loss of control will then be given. Figure 3 shows how these different parameter estimation tools interact to form the research approach.

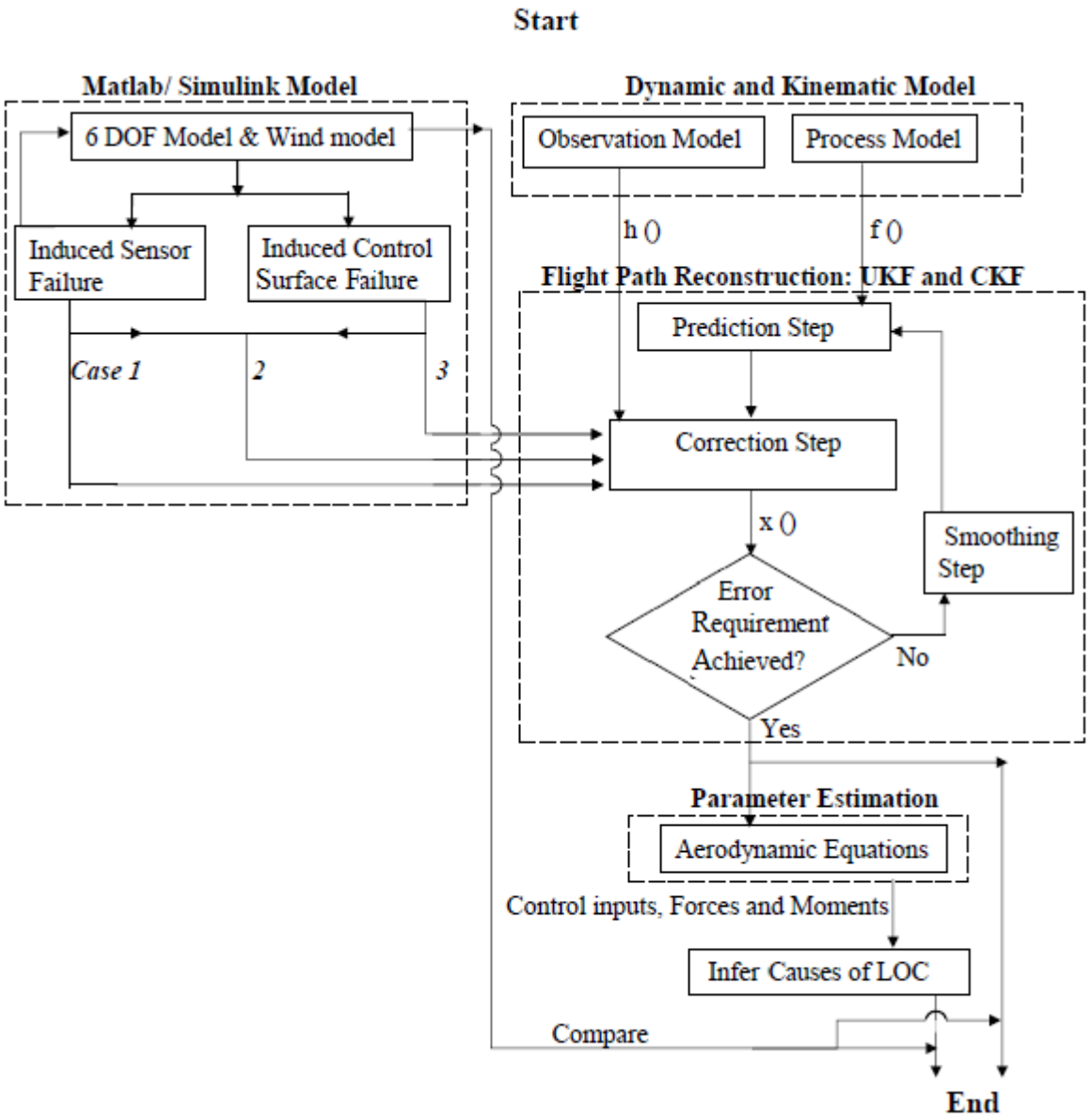

Figure 3: Research approach

1.7.1 MATLAB/Simulink® model criteria for verification

A zero test will be used to verify the MATLAB/Simulink® model. If all resultant forces and moments are set to zero, the velocity and altitude of the aircraft in the MATLAB/Simulink® model must be maintained. A response other than a zero change in the velocity and altitude will show that the model has not been set up correctly. After verification of the MATLAB/Simulink® model, trim conditions for the GTM UAV will be compared to those obtained by Kwatny et al., [30] and Gill et al., [36] under similar conditions. Additionally, results obtained from the simulation will be compared to the general response expected from a 6 DOF simulation of its nature obtained for step, doublet and pulse control inputs. To

further verify the MATLAB/Simulink® model, the non-linear flight response of GTM UAV is compared to wind tunnel and flight test data provided by Padayachee [25], and Cunningham et al., [49] respectively, for the same forms of excitation.

1.7.2 Kalman filters criteria for validation

To validate the Kalman filters, flight path reconstruction is performed. If the UKF and CKF estimate parameters adequately then these algorithms have been set up correctly. Monte Carlo analysis is used to determine the filter performance under unmodelled instrumentation errors, through the use of various random coloured noise functions w and v [46]. Consequently, Monte Carlo simulation runs will be used to check the accuracy of estimated parameters, robustness to bias as well as Kalman filter divergence [46, 50, 51]. The accumulated root mean square error (ARMSE) will be used to compare the performance of the unscented Kalman filter and cubature Kalman filter [52]. Equation (1.3) shows how the accumulated root mean square error is calculated. N and K are the number of Monte Carlo runs and total number of time steps respectively. $\|e_k^n\|^2$ is the squared state error which is calculated by squaring the difference between the estimated state and the true state values. The performance of a parameter estimator is expressed by its variance properties [37]. As a result, the root mean square error (RMSE) is calculated at each Monte Carlo run; the mean and standard deviation values are recorded per N number of Monte Carlo runs. These RMSE values will be used in hypothesis testing to compare the performance of the UKF and CKF for each state.

$$ARMSE = \sqrt{\frac{1}{N}\frac{1}{K}\sum_{n=1}^{N}\sum_{k=1}^{K}\|e_k^n\|^2} \tag{1.3}$$

1.8 Research Report Outline

This report is organised as follows:

- Chapter 2: The aircraft dynamic and kinematic model is discussed. In this chapter, six DOF equations of a UAV aircraft are derived; these equations are the bases of the MATLAB/Simulink model. The atmospheric disturbance and thrust models are also presented in this chapter.
- Chapter 3: The MATLAB/Simulink model is developed. System parameters, trim conditions and sensor noise considerations are stated in this chapter. PID control laws

are applied to the simulink model to maintain steady-level flight in the presence of atmospheric disturbances and small perturbations about the trim state.

- Chapter 4: The general kinematic, input and output equations are derived. Cubature and unscented Kalman filters are synthesised and implemented in this chapter. Noise considerations with reference to the cubature and unscented Kalman filters are established.

- Chapter 5: Verification and validation of the MATLAB/Simulink® model and Kalman filters are carried out.

- Chapter 6: Results are presented and discussed. The cubature and unscented Kalman filter algorithms are used to reconstruct the flight path of the UAV simulated in the MATLAB/Simulink model. Results obtained in flight path reconstruction are used to calculate control inputs, force and moment coefficients. Suggestions of reasons behind the loss of control are given. Additionally, the performance of the cubature and unscented Kalman filters is analysed using independent Monte Carlo simulation runs, accumulated root mean square error and hypothesis testing.

- Chapter 7: Conclusions are made from the results and discussions presented in Chapter 6. Recommendations for future work are also given in this chapter.

2 Aircraft Dynamic and Kinematic Model

The aircraft dynamic and kinematic model is used for both the MATLAB/Simulink® model and the Kalman filters. This model is non-linear in order to capture the true non-linear nature of UAV motion. In this section, the mathematical expressions representing the aircraft dynamic and kinematic model for non-linear flight, the atmospheric disturbance and thrust models are derived. All assumptions made during this exercise are also stated.

2.1 Assumptions

The general aircraft six degrees-of-freedom (DOF) equations of motion are accompanied by assumptions a to c. Additional assumptions d to i, relevant to this study have been added. The following key assumptions are made in this work;

a. The aircraft is a rigid body, as such aeroelastic effects are negligible.

b. Cxz is a plane of symmetry hence I_{yz} and $I_{xy} = 0$; $I_{xz} \neq 0$.

c. Airframe damage does not occur, as such there is no cg shift during flight.

d. Mass remains relatively constant for the time durations being investigated.

e. Any angular misalignment between the engine and the body axes is negligible ($\vartheta_{TZ} = \vartheta_{TY} \approx 0$), as such any contribution to forces in the y and z direction is not significant.

f. The line of action of the engine thrust component is aligned to the aircraft cg ($z_T = y_T \approx 0$), as such aerodynamic moment is also negligible.

g. The effect of engine spinning rotors is negligible ($I_T\omega_T \approx 0$).

h. The accelerometers, gyroscopes and GPS receivers are located at the aircraft centre of gravity.

2.2 Six Degrees-of-Freedom Equations of Motion

There are twelve general equations of aircraft motion. After applying the assumptions made in Section 2.1, the final equations of motion (2.1) to (2.7) represent the unsteady motion of an aircraft. These body-axes equations of motion were adopted from Etkin and Reid [53].

The schematic of the body-axes frame of reference and that of the axes of the engine with reference to the body-axes is shown in Figures 4 and 5 respectively.

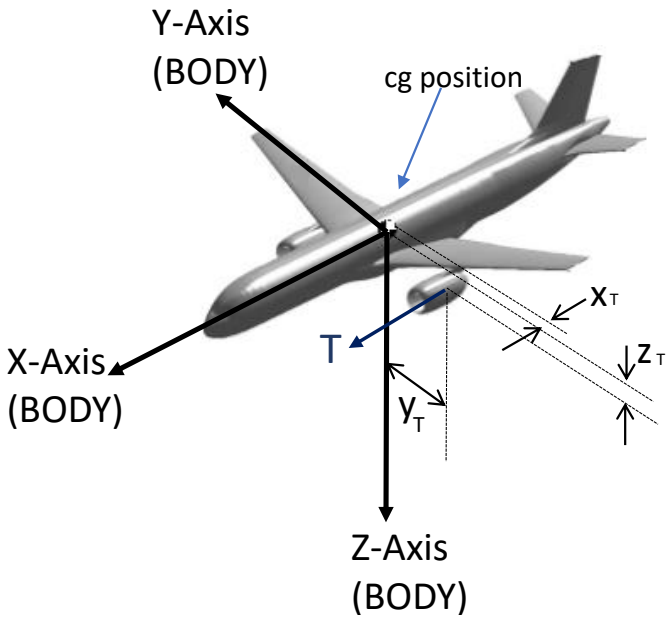

Figure 4: Aircraft body-axes and engine displacements relative to the aircraft cg (adopted from Nguyen et al., [48]).

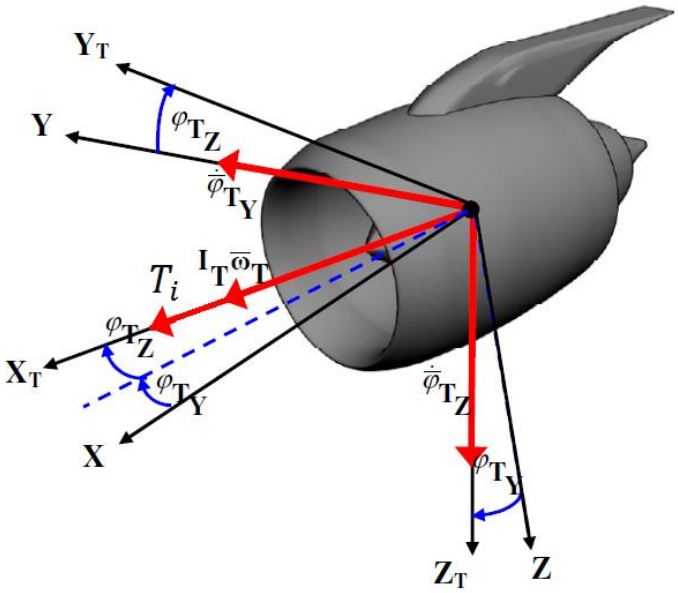

Figure 5: Axes and transformation of the engine force and rotor components (adopted from Panday [54]).

The twelve general equations of aircraft motion are as follows.

The force equations are:

$$m(\dot{u} + qw - rv) = -mgsin\theta + \sum_{i=1}^{n} T_i cos\varphi_{TY} cos\varphi_{TZ} - \frac{1}{2}\rho V_A^2 S C_x,$$

$$m(\dot{v} + ru - pw) = mgcos\theta sin\phi + \sum_{i=1}^{n} T_i sin\varphi_{TZ} + \frac{1}{2}\rho V_A^2 S C_y, \tag{2.1}$$
$$m(\dot{w} + pv - qu) = mgcos\theta cos\phi - \sum_{i=1}^{n} T_i cos\varphi_{TZ} sin\varphi_{TY} + \frac{1}{2}\rho V_A^2 S C_z,$$

where m is the aircraft mass, g is the acceleration due to gravity, u, v and w are the x, y and z components of the aircraft translational velocity relative to the surrounding air, and $\dot{u}$, $\dot{v}$ and $\dot{w}$ are the corresponding accelerations. C_x, C_y and C_z are the aerodynamic force coefficients in the body-axes. The variables p, q and r are the angular rates, ϕ, θ and ψ are the Euler angles, and T, φ_{TY} and φ_{TZ} are the engine thrust and angular positions of the engine respectively. While ρ, V and S represent air density, airspeed and wing reference area respectively. V_A is the total aerodynamic velocity calculated using the airspeeds and the wind velocity components, W_x, W_y and W_z, in the body-axes reference frame:

$$V_A = \sqrt{(u - W_x)^2 + (v - W_y)^2 + (w - W_z)^2}). \tag{2.2}$$

When assumption (f) is applied, the following is true: φ_{TY} and $\varphi_{TZ} \approx 0$, $cos\varphi_{TY} = cos\varphi_{TZ} \approx 1$ and $sin\varphi_{TY} = sin\varphi_{TZ} \approx 0$. Then Equation (2.1) becomes:

$$\begin{aligned} m(\dot{u} + qw - rv) &= -mgsin\theta + \sum_{i=1}^{n} T_i - \frac{1}{2}\rho V_A^2 S C_x, \\ m(\dot{v} + ru - pw) &= mgcos\theta sin\phi + \frac{1}{2}\rho V_A^2 S C_y, \\ m(\dot{w} + pv - qu) &= mgcos\theta cos\phi + \frac{1}{2}\rho V_A^2 S C_z. \end{aligned} \tag{2.3}$$

The moment equations are:

$$\begin{aligned} I_x\dot{p} - (I_y - I_z)qr - I_{xz}(\dot{r} + pq) &= \sum_{i=1}^{n} I_T\omega_T(rsin\varphi_{TZ} + qcos\varphi_{TY}sin\varphi_{TY}) - \\ &\sum_{i=1}^{n} T_i(y_T cos\varphi_{TZ} sin\varphi_{TY} + z_T sin\varphi_{TZ}) + \frac{1}{2}\rho V_A^2 S b C_l, \\ I_y\dot{q} - (I_y - I_x)pr - I_{xz}(r^2 - p^2) &= \sum_{i=1}^{n} T_i(z_T cos\varphi_{TZ} cos\varphi_{TY} + x_T cos\varphi_{TZ} sin\varphi_{TY}) \\ &- \sum_{i=1}^{n} I_T\omega_T(rcos\varphi_{TZ}cos\varphi_{TY} + pcos\varphi_{TY}) + \frac{1}{2}\rho V_A^2 S\bar{c} C_m, \\ I_z\dot{r} - (I_x - I_y)qp - I_{xz}(\dot{p} - rq) &= \sum_{i=1}^{n} T_i(x_T sin\varphi_{TZ} - y_T cos\varphi_{TZ} cos\varphi_{TY}) \\ &+ \sum_{i=1}^{n} I_T\omega_T(qcos\varphi_{TZ}cos\varphi_{TY} - psin\varphi_{TZ}) + \frac{1}{2}\rho V_A^2 S b C_n, \end{aligned} \tag{2.4}$$

where I_x, I_y and I_z are the roll, pitch and yaw moments of inertia, I_{xz} is the product of inertia, and I_T and ω_T represent the engine spinning rotors moment of inertia and angular rates respectively. While x_T, y_T and z_T are the coordinates of the engine position with respect to the centre of gravity, and b and $\bar{c}$ are the aircraft wing span and mean aerodynamic chord. When assumption (g) and (h) are applied in addition to assumption (f), then $z_T = y_T \approx 0$ and $I_T\omega_T \approx 0$. Equation (2.4) simplifies to:

$$\begin{aligned} I_x\dot{p} - (I_y - I_z)qr - I_{xz}(\dot{r} + pq) &= \frac{1}{2}\rho V_A^2 SbC_l, \\ I_y\dot{q} - (I_y - I_x)pr - I_{xz}(r^2 - p^2) &= \frac{1}{2}\rho V_A^2 S\bar{c}C_m, \\ I_z\dot{r} - (I_x - I_y)qp - I_{xz}(\dot{p} - rq) &= \frac{1}{2}\rho V_A^2 SbC_n. \end{aligned} \tag{2.5}$$

The kinematic equations are:

$$\begin{aligned} \dot{\phi} &= p + (qsin\phi + rcos\phi)tan\theta, \\ \dot{\theta} &= qcos\phi - rsin\phi, \\ \dot{\psi} &= (qsin\phi + rcos\phi)sec\theta. \end{aligned} \tag{2.6}$$

The navigational equations are:

$$\begin{aligned} \dot{x}_E &= ucos\theta cos\psi + v(sin\phi sin\theta cos\psi - cos\phi sin\psi) + w(cos\phi sin\theta cos\psi + sin\phi sin\psi), \\ \dot{y}_E &= ucos\theta sin\psi + v(sin\phi sin\theta sin\psi + cos\phi cos\psi) + w(cos\phi sin\theta sin\psi - sin\phi cos\psi), \\ \dot{z}_E &= -usin\theta + vsin\phi cos\theta + wcos\phi cos\theta, \end{aligned} \tag{2.7}$$

where $\dot{x}_E$, $\dot{y}_E$ and $\dot{z}_E$ give the rate of change of the aircraft position with respect to the Earth.

2.3 Forces and Moments Coefficients for Non-linear Motion

The equations of motion (2.1) to (2.7), represent both linear and non-linear flight. For linear flight, coefficients of the equations for C_x, C_y, C_z, C_l, C_m and C_n are constant. However, for non-linear flight which is the subject of this study, these coefficients are non-linear functions of α, β, δ_e, δ_a and δ_r [55]. Kwatny et al., [30] gave details of how the force and moment coefficients of the GTM vary with α, β, δ_e, δ_a and δ_r when modelling non-linear flight. Equations (2.8) to (2.13) show the functions of C_x, C_y, C_z, C_l, C_m and C_n for non-linear flight about the body-axes frame of reference. The polynomial coefficients of these functions a_n, b_n, c_n, d_n, e_n and f_n are given in Appendix 1.

$$C_x(\alpha,\delta_e) = -a_0 + a_1\alpha + a_2\alpha^2 - a_3\alpha^3 - a_4\alpha^4 + a_5\alpha^5 + \frac{q\bar{c}(a_6 + a_7\alpha + a_8\alpha^2)}{2V_A} + a_9\alpha\delta_e + a_{10}\alpha^3\delta_e - a_{11}\alpha^5\delta_e - a_{12}\delta_e^2 + a_{13}\alpha^2\delta_e^2 - a_{14}\alpha^4\delta_e^2 - a_{15}\alpha\delta_e^3 + a_{16}\alpha^3\delta_e^3 - a_{17}\alpha^5\delta_e^3 \tag{2.8}$$

$$C_y(\beta,\alpha,\delta_r) = -b_0\beta + b_1\beta^3 + \frac{rb(b_2 + b_3\alpha + b_4\alpha^2)}{2V_A} + \frac{pb(b_5\alpha + b_6\alpha^2 - b_7\alpha^3)}{2V_A} + b_8\delta_r \tag{2.9}$$

$$C_z(\alpha,\delta_e) = -c_0 - c_1\alpha + c_2\alpha^2 - c_3\alpha^3 - c_4\alpha^4 + c_5\alpha^5 + \frac{q\bar{c}(-c_6 - c_7\alpha - c_8\alpha^2)}{2V_A} - c_9\delta_e - c_{10}\alpha^2\delta_e + c_{11}\alpha^4\delta_e - c_{12}\alpha\delta_e^2 + c_{13}\alpha^3\delta_e^2 - c_{14}\alpha^5\delta_e^2 + c_{15}\delta_e^3 - c_{16}\alpha^2\delta_e^3 + c_{17}\alpha^4\delta_e^3 \tag{2.10}$$

$$C_l(\beta,\alpha,\delta_r,\delta_a) = -d_0\beta - d_1\alpha\beta + d_2\beta^3 - d_3\beta^5 + \frac{rb(d_4 + d_5\alpha + d_6\alpha^2)}{2V_A} + \frac{pb(-d_7 - d_8\alpha + d_9\alpha^2 + d_{10}\alpha^4)}{2V_A} - d_{11}\delta_a + d_{12}\delta_r \tag{2.11}$$

$$C_m(\alpha,\beta,\delta_e) = e_0 - e_1\alpha - e_2\beta^4 + \frac{q\bar{c}(-e_3 + e_4\alpha + e_5\alpha^2)}{2V_A} - e_6\delta_e - e_7\alpha\delta_e^2 - e_8\delta_e^3 \tag{2.12}$$

$$C_n(\alpha,\beta,\delta_r) = f_0 - f_1\beta^3 + \frac{rb(-f_2 - f_3\alpha - f_4\alpha^2)}{2V_A} + \frac{pb(-f_5 - f_6\alpha + f_7\alpha^2 + f_8\alpha^3)}{2V_A} - f_9\delta_r + f_{10}\beta\delta_r \tag{2.13}$$

The aerodynamic angle of attack, α and sideslip angle, β are given by:

$$\alpha = sin^{-1}\left(\frac{w - W_z}{V_A}\right),$$
$$\beta = sin^{-1}\left(\frac{v - W_y}{V_A}\right). \tag{2.14}$$

2.4 Thrust Model

As discussed in Section 1.3.3, the GTM UAV is a 5.5% dynamically-scaled model of a large aircraft. The GTM UAV uses two Jetcat P70 turbofan engines. The engine specifications for a Jetcat P70 turbofan engine are provided in Table 1. These engine specifications and the

Table 1: The engine specifications for a Jetcat P70 turbofan engine

Specifications	Value
Idle RPM	35 000rev/min
Max RPM	123 000rev/min
Thrust at idle RPM	3.33 N
Thrust at max RPM	70 N
Fuel consumption at static thrust	0.2268kg/min

thrust model developed in this section are used in the MATLAB/Simulink for the turbofan engine system.

The GTM UAV used in this study was developed by Jordan et al., [33]. Table 2 shows how the dimensional scaling was achieved. The scaling factor K is equal to 0.055.

Table 2: Scale factors used in the dynamic scaling of the GTM UAV

Property	Dimension	Scaling factor
Length	L	K
Mass	M	K^3
Response	T	$\sqrt{K}$
Area	L^2	K^2
Volume	L^3	K^3
Weight	MLT^{-2}	K^3
Moment of inertia	ML^2	K^5
Velocity	LT^{-1}	$\sqrt{K}$
Acceleration	LT^{-2}	1

Jordan et al., [33] did not provide a thrust model for the GTM UAV, as a result, a similar scaling exercise is done to determine GTM UAV thrust. The variation of thrust with altitude is given by:

$$T = \left(\frac{\rho}{\rho_0}\right)^{0.7} (AV^2 + BV + C)\frac{\delta_T}{\delta_{Tmax}}. \tag{2.15}$$

The coefficients A, B and C for a typical turbofan engine are equal to -2.338, 574 and 65260 respectively [54]. δ_T and ρ represent throttle deflection and air density respectively. In order to determine the variation of GTM UAV thrust with velocity and altitude, the thrust model for a full-scale aircraft in Equation (2.15) is scaled accordingly. This is done by first scaling up the GTM UAV velocity, applying this velocity to Equation (2.15). Finally, the thrust

obtained is scaled down for the GTM UAV. The scaling factors established by Jordan et al., [33] are used in this exercise. Steps followed to obtain the thrust model are as follows:

Step 1: Scale up of GTM UAV velocity

$$V_{largeaircraft} = \frac{V_{GTM}}{\sqrt{K}} \tag{2.16}$$

Step 2: Apply Equation (2.15)

Step 3: Scale down the large aircraft thrust

$$T_{GTMo} = T_{largeaircraft} \times K^3 \tag{2.17}$$

Step 4: Account for the different altitudes

$$T_{GTM} = T_{GTMo} \times \frac{Density_{GTM}}{Density_{aircraft}} \tag{2.18}$$

Equation (2.15) and this scaling method are used to develop the simulation thrust model.

2.5 Atmospheric Disturbance and Turbulence Model

The equations of motion, Equations (2.1) to (2.7), presented in Section 2.2 are sufficient to represent flight if there is no atmospheric disturbance, however this is hardly the case in actual flight [53, 55]. Wind velocity has a vital influence on UAV performance, as such assuming a zero wind field is erroneous [26, 56]. The International Civil Aviation Organisation (ICAO) standard atmosphere also known as the windshear model, can be applied to represent a typical wind profile due to the Earth's boundary layer. The windshear model is given by [55, 57]:

$$V_w = V_w|_{h=9.15m} \times \frac{h^{0.2545} - 0.4097}{1.347} \qquad 0 < h < 300m,$$

$$V_w = 2.86585 \times V_w|_{h=9.15m} \qquad h \geq 300m. \tag{2.19}$$

$V_w|_{h=9.15m}$ is the wind speed at an altitude of 9.15m, in this study this velocity is varied to represent light, moderate and severe wind speeds. The components of wind velocity in the body axes are given by Equation (2.20). The angle ψ_w is the direction of the wind vector with respect to the Earth and ψ is the heading. This angle is 0° if the wind is blowing from North to South.

$$u_w = V_w cos(\psi_w - \pi) cos\psi + V_w sin(\psi_w - \pi) sin\psi \tag{2.20}$$

$$v_w = -V_w cos(\psi_w - \pi) sin\psi + V_w sin(\psi_w - \pi) cos\psi \tag{2.21}$$

The windshear model does not take into account random fluctuations in translational and rotational velocity. Von Karman and Dryden wind models are used to represent turbulence. The Dryden wind model is more convenient to simulate, as such it is preferred by researchers [58]. The Dryden wind model generates random fluctuations by filtering white noise through set of transfer functions to give a turbulence velocity, that is a coloured noise. The result of this exercise gives the translational and rotational fluctuations; u_w, v_w, w_w and p_w, q_w, r_w respectively [57, 58]. The Dryden wind model for turbulence is given by the following transfer functions:

$$H_u(s) = \sigma_u \sqrt{\frac{2L_u}{\pi V}} . \frac{1}{1 + sL_u/V},$$

$$H_v(s) = \sigma_v \sqrt{\frac{L_v}{\pi V}} . \frac{1 + \sqrt{3}L_v s/V}{(1 + L_v s/V)^2},$$

$$H_w(s) = \sigma_w \sqrt{\frac{L_w}{\pi V}} . \frac{1 + \sqrt{3}L_w s/V}{(1 + L_w s/V)^2}, \tag{2.22}$$

$$H_p(s) = \sigma_w \sqrt{\frac{0.8}{V}} . \frac{(\pi/4b)^{1/6}}{L_w^{1/3}(1 + (4b/\pi V)s)},$$

$$H_q(s) = \frac{(s/V)}{1 + (4b/\pi V)s} . H_w(s),$$

$$H_r(s) = \frac{(s/V)}{1 + (3b/\pi V)s} . H_v(s),$$

where σ_u, σ_v, σ_w and L_u, L_v, L_w represent turbulence intensities and scale lengths respectively. In this study, atmospheric disturbance is modelled by the superposition of the windshear profile in Equation (2.19) and the Dryden wind model. This will provide a realistic wind model for the simulation; and is similar to work done by Borup et al., [26]. Gage, gave equations to calculate turbulence intensities and scale lengths [59]. The turbulence intensities and scale lengths are a function of altitude. Equation (2.23) shows how the turbulence intensities are calculated for altitudes less than 1000ft (304.9m).

$$\begin{aligned} \sigma_w &= 0.1 V_{w|h=6m}, \\ \sigma_u = \sigma_v &= \frac{\sigma_w}{(0.177 + 0.000823h)^{0.4}}, \end{aligned} \tag{2.23}$$

where $V_{w|h=6m}$ is the wind velocity at a height of 6m. Similar to the parameter $V_{w|h=9.15m}$, in the windshear profile, this velocity is varied to model light, moderate and severe turbulence. Table 3 shows the widely accepted values of $V_{w|h=6m}$.

Table 3: Values of $V_{w|h=6m}$ for different turbulence levels [59]

Turbulence level	$V_{w\|h=6m}$
Light	$7.717m/s$
Moderate	$15.433m/s$
Severe	$23.150m/s$

For altitudes less than 1000ft (304.9m) the scale lengths are given by:

$$L_w = h, \tag{2.24}$$

$$L_u = L_v = \frac{h}{(0.177 + 0.000823h)^{1.2}}.$$

For altitudes greater than 2000ft (609.8m), values of turbulence intensities are obtained from look-up tables; and all scale lengths are constant and equal to 533.4 m. For the intermediate altitudes, interpolation is used to estimate the values of turbulence intensities and scale lengths. Ultimately, these different wind components are added to the aircraft translational and rotational velocities through the vector addition:

$$V_A = V_o - W = [u \quad v \quad w]^T - [W_x \quad W_y \quad W_z]^T, \tag{2.25}$$

$$\Omega_A = \Omega_o - \Omega_w = [p \quad q \quad r]^T - [p_w \quad q_w \quad r_w]^T,$$

where V_o is the absolute velocity vector, W is the wind vector in the body-axes, Ω_o is the angular velocity vector, and Ω_w represents the wind angular velocity vector.

3 Implementation of the Mathematical Model and Controller Design

The kinematic and dynamic model, thrust, atmospheric disturbance and turbulence models derived in Section 2 are used to simulate the non-linear flight of the GTM UAV in MATLAB/Simulink® prior and post loss of control is initiated. This model provides the aircraft sensor measurements for the parameter estimation exercise. GTM UAV parameters, control criterion, structure of the simulation model and noise considerations are discussed in this chapter.

3.1 GTM UAV System Parameters

There is a number of versions of the GTM UAV. The GTM UAV developed in the work done by Jordan et al., [33] and whose geometry was later probed by Grauer and Morelli, [60] is used in this study. This UAV is called the GTM T2. Table 4 shows the geometric and mass parameters of the GTM T2 UAV used in the MATLAB simulation model.

Table 4: Parameters of the GTM T2 UAV, adapted from Grauer and Morelli [60].

Property	Symbol	Value	Units
Centre of gravity position	x_{cg}	0.25	$\%\bar{c}$
Wing span	b	2.0875	m
Mean aerodynamic chord	$\bar{c}$	0.2790	m
Wing area	S	0.5483	m^2
Mass	m	22.4979	kg
Roll inertia	I_{xx}	1.7992	kgm^2
Pitch inertia	I_{yy}	5.7676	kgm^2
Yaw inertia	I_{zz}	7.3946	kgm^2
Roll/ yaw coupling inertia	I_{xz}	0.1627	kgm^2

Péni et al., [35] provide a transfer function describing actuator and throttle dynamics of the GTM UAV; these are shown in Equation (3.1) and (3.2) respectively. The corresponding roots are: s_{act} = -10π and the complex pair s_{eng} = -0.668 $\pm$ 0.534i; when the negative reciprocals of the real part of the roots are taken, the time constants are given by τ_{act} = 0.03s and τ_{eng} = 1.5s. The actuator time constant, 0.03s is stated in the work by Péni et al., [35]; whereas the engine time constant calculated falls in the range of 0.85s to 1.96s that is obtained by Cunningham et al., [49]; who extensively studied the dynamics of the GTM T2.

$$G_{act} = \frac{10\pi}{s + 10\pi} \tag{3.1}$$

$$G_{eng} = \frac{0.1474s + 0.7314}{s^2 + 1.336s + 0.7314} \tag{3.2}$$

The control inputs for the Simulink model are [δ_e, δ_a, δ_r, δ_T]^T. The ranges of these control inputs are given in Table 5 [30], the corresponding time constants are also given.

Table 5: Range for the control inputs

Property	Range	Time constant
Elevator	$-40° \leq \delta_e \leq 20°$	0.03 sec lag
Aileron	$-20° \leq \delta_a \leq 20°$	0.03 sec lag
Rudder	$-30° \leq \delta_r \leq 30°$	0.03 sec lag
Thrust	$0 \leq \delta_T \leq 1$	1.5 sec lag

3.2 Trim Conditions Prior to LOC

For the purpose of parameter estimation and controller design, the non-linear aircraft model was trimmed in MATLAB/Simulink®. These trim conditions provide the initial conditions of the parameter estimation exercise before loss of control is initiated. In this task, it is assumed that there are no atmospheric disturbances. The trim conditions obtained are given in Table 6. These trim conditions are compared to those obtained via simulation by Kwatny et al., [30] and Gill et al., [36].

Table 6: Trim conditions

Property	Units	Simulation Results	Kwatny et al.,	Gill et al.,
V	ms^{-1}	45.0762	45.7178	47.3400
α	deg	2.999	2.966	3
δ_T	-	0.124	0.102	0.221
δ_e	deg	4.03	1.725	2.58
δ_a	deg	2.352x10^{-8}	0	-0.004
δ_r	deg	-1.0133 x10^{-8}	0	0.009

Though the trim conditions obtained during the simulation are comparable to those obtained by Kwatny et al., [30] and Gill et al., [36] there are some significant differences in the elevator, aileron and rudder deflection required to maintain trim conditions. Variances in the trim conditions may be due to different thrust models used, as well as a difference in engine

orientation applied in the different simulation models. It is assumed that the engine axes are in line with the body-axes in this work as well as in that of Kwatny et al., [30]; Gill et al., [36] however did not.

3.3 Controller Design

3.3.1 Controller justification

If wind conditions are not considered, the GTM UAV model maintains steady-level flight when trimmed. However, as discussed in Sections 1.3.1 and 2.5 wind is vital when modelling UAV flight; for this reason the atmospheric disturbance model derived in Section 2.5 is applied to the MATLAB simulation. When atmospheric disturbance is imposed, the UAV aircraft departs from steady-level flight; as shown in Figure 6.

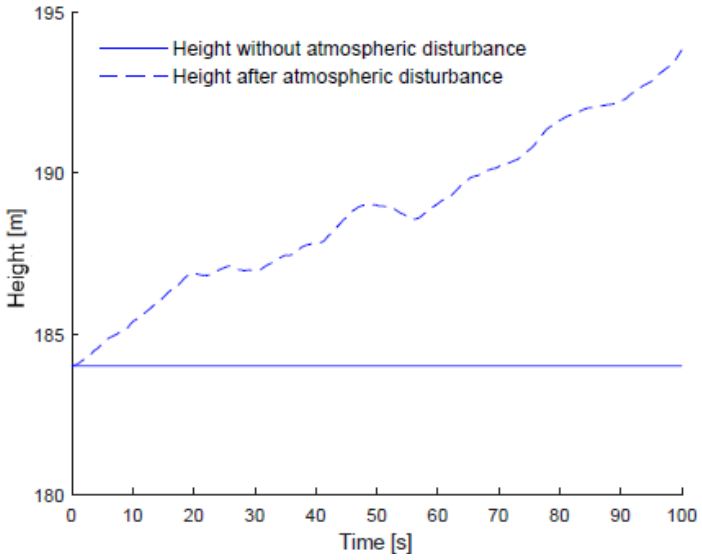

Figure 6: Behaviour of aircraft after experiencing an atmospheric disturbance.

As a consequence of the aircraft behaviour shown in Figure 6, a flight control system is applied to maintain steady-level flight in the presence of the atmospheric disturbances and small perturbations about the trim state.

3.3.2 PID controller model

A PID control law is employed for the aircraft control system for its simplicity. Equations (3.3) to (3.6) express the control laws used for this flight control system. There are four control channels that correspond to the four inputs $[\delta_e, \delta_a, \delta_r, \delta_T]$.

Elevator channel

$$\begin{aligned}\tau_e\dot{\delta_e} + \delta_e = K_{e\theta}(\theta_c - \theta) + K_{eq}(q_c - q) + K_{e\alpha}(\alpha_c - \alpha) + K_{ez_e}(z_{ec} - z_e) \\ + K_{e_{I\theta}}\int(\theta_c - \theta)dt + \delta_{e_0}\end{aligned} \tag{3.3}$$

Aileron channel

$$\begin{aligned}\tau_a\dot{\delta_a} + \delta_a = K_{a\phi}(\phi_c - \phi) + K_{ap}(p_c - p) + K_{a\psi}(\psi_c - \psi) + K_{ar}(r_c - r) \\ + K_{ay_e}(y_{ec} - y_e) + K_{a_{I\phi}}\int(\phi_c - \phi)dt + K_{a\beta}(\beta_c - \beta) + \delta_{a_0}\end{aligned} \tag{3.4}$$

Rudder channel

$$\begin{aligned}\tau_r\dot{\delta_r} + \delta_r = K_{r\phi}(\phi_c - \phi) + K_{rp}(p_c - p) + K_{r\psi}(\psi_c - \psi) + K_{rr}(r_c - r) \\ + K_{ry_e}(y_{ec} - y_e) + K_{r_{I\phi}}\int(\phi_c - \phi)dt + K_{r\beta}(\beta_c - \beta) + \delta_{r_0}\end{aligned} \tag{3.5}$$

Thrust channel

$$\begin{aligned}\tau_T\dot{\delta_T} + \delta_T = K_{T\theta}(\theta_c - \theta) + K_{Tq}(q_c - q) + K_{T\alpha}(\alpha_c - \alpha) \\ + K_{Tz_e}(z_{ec} - z_e) + K_{Tx_e}(x_{ec} - x_e) + K_{T_{IV}}\int(V_c - V)dt \\ + K_{T_V}(V_c - V) + K_{T_{\dot{V}}}(\dot{V}_c - \dot{V}) + \delta_{T_0}\end{aligned} \tag{3.6}$$

The subscript c in the variables ϕ_c, θ_c, ψ_c, p_c, q_c, r_c, x_{ec}, y_{ec}, z_{ec}, α_c , β_c, V_c and $\dot{V}_c$ indicates the state commands used to attain the desired conditions. τ_* and K_* are the corresponding actuator time constants and gains for each control channel respectively. Values of these actuator time constants are discussed in Section 3.1, whilst the PID gains are tuned manually. Table 7 shows the values obtained for the controller gains. The desired conditions used for the controller tuning exercise were the trim conditions discussed in Section 3.2.

Table 7: Controller gains for the PID control law

Elevator Channel		Aileron Channel		Rudder Channel		Thrust Channel	
Symbol	Value	Symbol	Value	Symbol	Value	Symbol	Value
K_{eq}	-0.1	K_{ap}	-15	K_{rp}	-0.1	K_{Tq}	0.008
$K_{e\alpha}$	-5.1	$K_{a\psi}$	-20	$K_{r\phi}$	-0.25	$K_{T\alpha}$	-4
K_{ez_e}	-0.0001	K_{ar}	-10	$K_{r\psi}$	-1.5	K_{Tz_e}	-0.003
$K_{e\theta}$	-0.9	$K_{a\phi}$	-80	K_{rr}	-0.008	$K_{T\theta}$	0.1
$K_{e_{I\theta}}$	-0.016	K_{ay_e}	-0.015	K_{ry_e}	-0.0045	$K_{T_{I\theta}}$	-0.01
		$K_{a_{I\phi}}$	-80	$K_{r_{I\phi}}$	-0.025	K_{T_V}	0.005
		$K_{a\beta}$	-0.05	$K_{r\beta}$	-1.8	$K_{T_{\dot{V}}}$	-0.01
						$K_{T_{IV}}$	0.001

3.3.3 Complete simulink model

The PID control laws described in Equations (3.3) and (3.6), and the gains acquired from the manual tuning exercise, were applied to the basic 6-DOF aircraft mathematical model. A schematic of how the basic 6-DOF model interacts with the control system developed is shown in Figure 7.

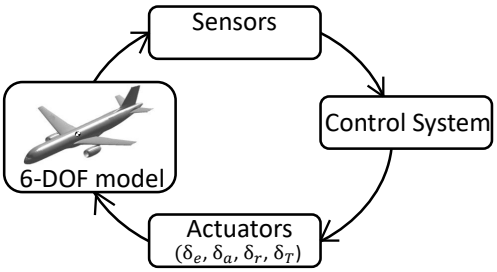

Figure 7: Schematic of the simulation model.

An overview of the simulation aircraft model and the control channels is shown in Figure 8.

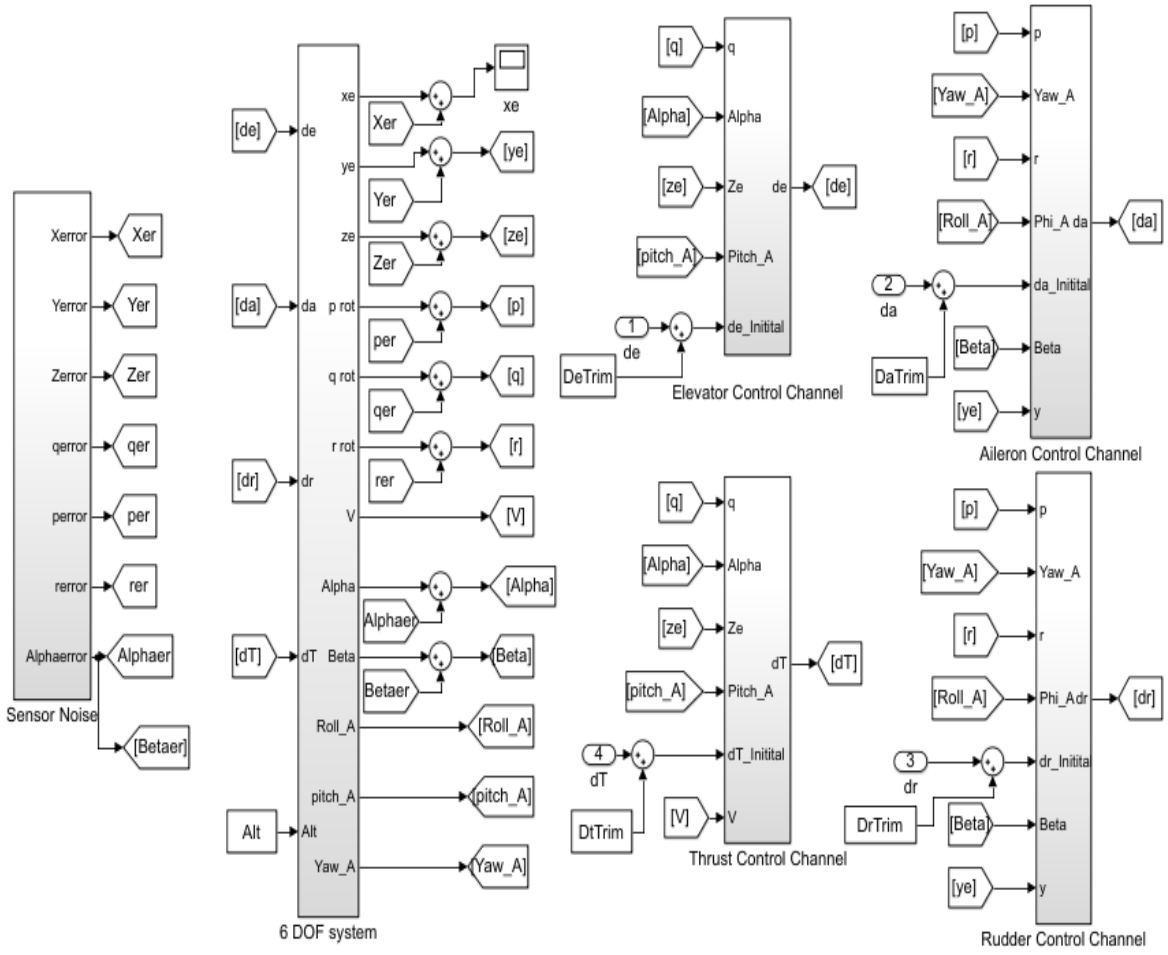

Figure 8: An overview of the interconnection of the aircraft model and control channels

A more detailed outline of the elevator control channel structure is shown in Figure 9. The aileron, thrust and rudder control channels have a similar structure.

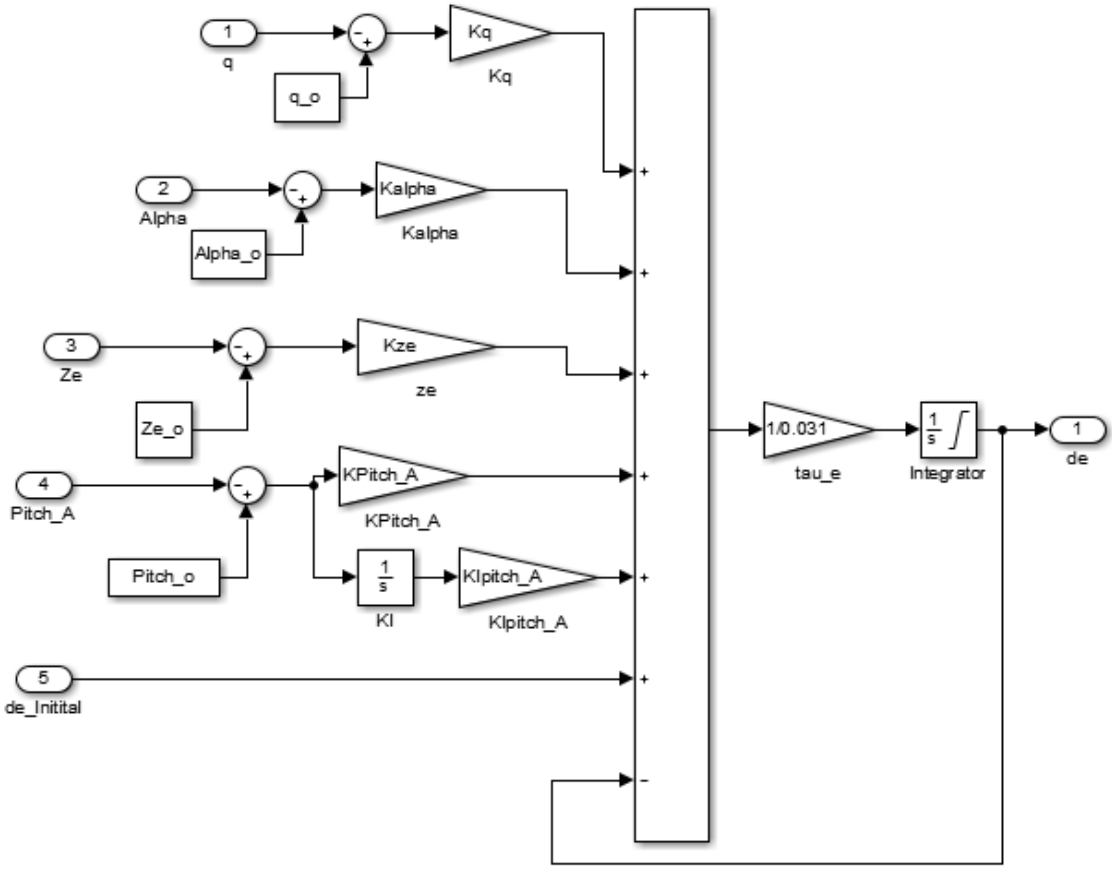

Figure 9: Structure of the elevator control channel

3.3.4 Controlled behaviour

The control gains presented in Table 7 were applied to the control law. Figure 10 shows a comparison of the aircraft response for trim conditions, atmospheric disturbance and PID-controlled flight. The controlled aircraft can maintain its relative flight path, velocity and attitude under atmospheric disturbance. This control system minimises the effect of wind disturbance on the aircraft flight path. The effect of atmospheric disturbance is minimal for the aircraft attitude. On the other hand, wind significantly affected aircraft position.

In order to maintain flight path, velocity and attitude under atmospheric disturbance the control surfaces are deflected. Figure 11 shows the percentage change in controller deflection and throttle setting required to maintain steady position, attitude and velocity. The percentage change in controller deflection for the elevator is small, which means not much elevator deflection is required to correct for wind disturbance. This makes for an effective elevator.

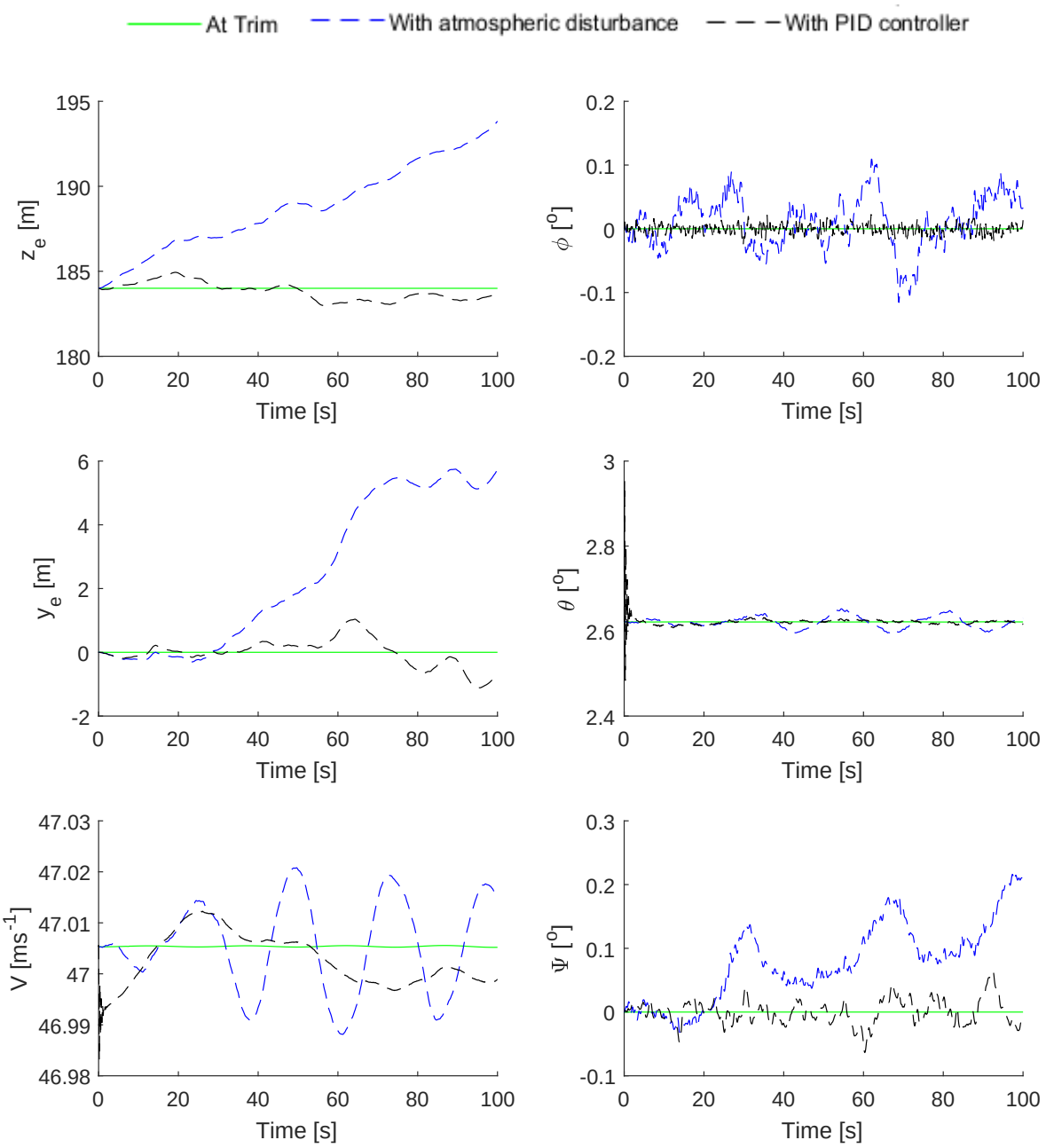

Figure 10: A comparison of aircraft position, velocity and attitude for trim, disturbed and controlled flight.

The same can be said for the throttle setting, however, the percentage difference in aileron and rudder deflection are significantly high. This may be because of the manner in which this percentage change is calculated. The difference of the deflections at trim and after controller implementation flight is divided by the deflection at trim. In the case of aileron and rudder surface deflection, the values at trim are small, in the order of 1^{-10}. Division by these small numbers result in the large magnitude of the percentage change in deflection.

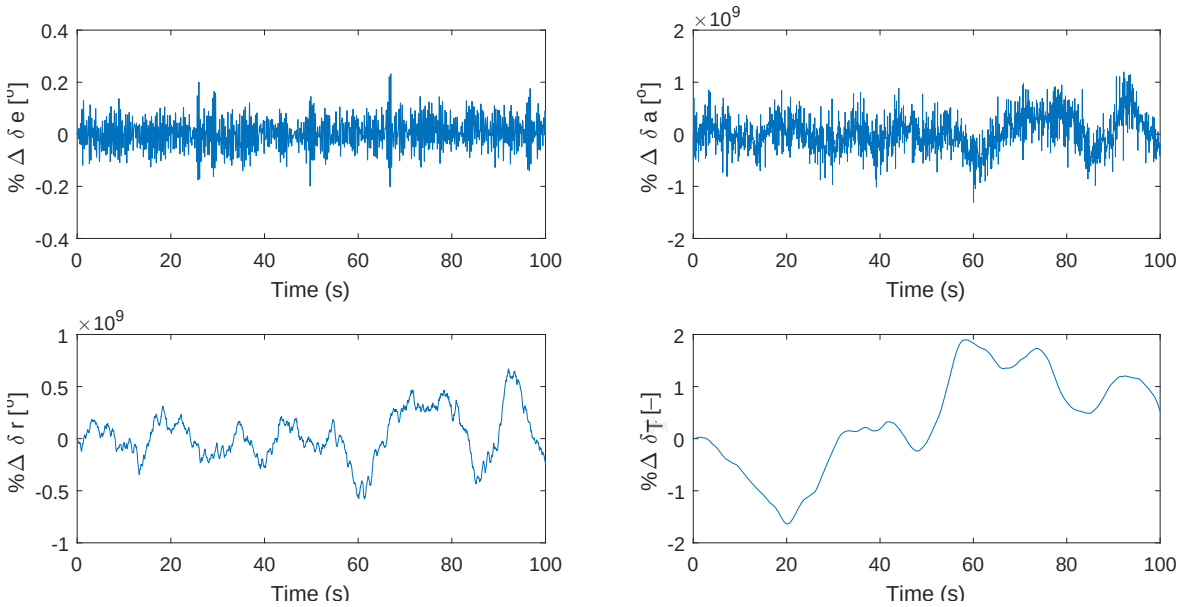

Figure 11: Percentage change in actuator settings required to maintain level flight.

The actual magnitudes of the control surface deflections and throttle settings needed to maintain steady flight in the presence of atmospheric disturbance are shown in Figure 12. It can be noted that the elevator deflected $\pm$ 0.01^o from its initial trim conditions, whilst the aileron and rudder had a $\pm$ 0.6^o and $\pm$ 0.2^o deflection respectively. There is also a small change in throttle settings. These small deviations show that the control surfaces are effective.

3.4 Sensor Noise

Typically, measured data exhibits some form of noise, bias errors, drift and resolution errors. Noise is defined as undesired fluctuations in the measured data; which may be attributed to power plant, mechanical vibrations, electronics noise and thermal fluctuations [61]. Such noise is unpredictable, accordingly the sensor noise is modelled as a random signal with different intensities to model light, moderate and severe noise conditions. Grauer and Morelli extensively studied the different sensor resolutions for the GTM UAV [60]. They presented the maximum sensor resolution error limits to attain different error budgets for modelling accuracy. The maximum resolution errors for 2%, 5% and 10% levels of different modelling

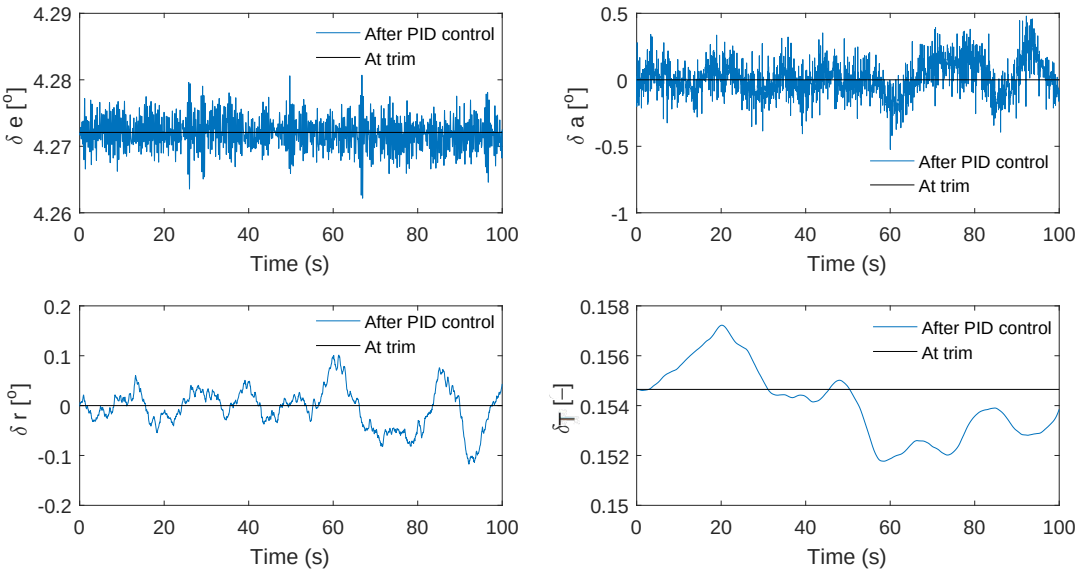

Figure 12: Actuator settings required to maintain level flight.

accuracies are given in Table 8. These sensor errors are modelled in MATLAB Simulink as random fluctuations with the resolution errors for the different error budgets as the maximum and minimum values.

Table 8: Measurement resolutions for different error budgets; adopted from Grauer and Morelli [60]

Measurement	Symbol	2%	5%	10%	Units
Air Flow Angles	α, β	0.1014	0.2024	0.4048	deg
Dynamic Pressure	$\bar{q}$	0.0435	0.7060	10.9396	$N/m^2(Pa)$
Gyroscopes	p, q, r	1.8707	4.2064	5.5439	deg/s
Accelerometers	a_x, a_y, a_z	0.0127	0.0262	0.0524	m/s^2
Potentiometers	$\delta_e, \delta_a, \delta_r$	0.0389	0.2457	0.4526	deg

4 Kalman Filters

The unscented Kalman and cubature Kalman filters are used for parameter estimation in this work. The bulk of this chapter shows how these filters are used to predict unknown parameters from measured data. The kinematic, input and output equations that are essential to the filtering exercise are derived at the beginning of this chapter. Steps taken to perform both the cubature and unscented Kalman filters are presented as well.

4.1 General Kinematic, Input and Output Equations

In spite that the unscented Kalman and cubature Kalman filters achieve parameter estimation via different methods, both filters are non-linear stochastic state estimators. The general discrete time non-linear state-space system is given by:

$$\begin{aligned} \mathbf{x}_k &= f(\mathbf{x}_{k-1}, \mathbf{u}_k, \mathbf{w}_k), \\ \mathbf{y}_k &= h(\mathbf{x}_k, \mathbf{u}_k, \mathbf{v}_k), \end{aligned} \tag{1.1}$$

where the non-linear function f, is the state vector function that governs aircraft motion; it is usually referred to as the kinematic equation. The function h, is the observation vector function that gives the relationship between the kinematic equation and the aircraft measured response. The vectors $\mathbf{x}$, $\mathbf{u}$ and $\mathbf{y}$ represent the state, input and observation vectors respectively. The input vector $\mathbf{u}$, gives the measured values of inputs. The relationship between these different vectors and their respective vector functions are derived and discussed in this section. The equations presented in this section have been adopted from work done by Klein and Morelli [62] and that done by Mulder et al., [13].

4.1.1 Kinematic and input equations

The translational, rotational and kinematic equations have been presented in Section 2.2. The aerodynamic and thrust forces in the translational kinematic equations are replaced by the body-axes accelerations (a_x, a_y, a_z) as shown in Equation (4.1). This ensures that only kinematic quantities appear in the translational kinematic equations. In addition, this is done because the body-axes accelerations are directly measured in flight through the accelerometer.

$$a_x = \frac{1}{m}\left(T + \frac{1}{2}\rho V^2 S C_x\right)$$

$$a_y = \frac{0.5}{m}\rho V^2 S C_y \tag{4.1}$$
$$a_z = \frac{0.5}{m}\rho V^2 S C_z$$

The rotational kinematic equations remain unchanged as shown in Equation (4.4). It should be noted that the angular velocities p, q and r are also measured kinematic inputs. The input vector to the state vector is given as [24, 43, 62]:

$$\mathbf{u} = [a_x \quad a_y \quad a_z \quad p \quad q \quad r]^T. \tag{4.2}$$

There are no major changes to the position kinematic equations, a minor difference is that the altitude h is given by $-z_E$. Unlike in the work done by Klein and Morelli [62], the aircraft position x_E and y_E is included in the state vector. Though x_E and y_E do not have any bearing on the stability and control of an aircraft, their values are used to track the position of the aircraft after loss of control has occurred. Given that the state vector is, $\mathbf{x} = [u \quad v \quad w \quad \phi \quad \theta \quad \psi \quad x_E \quad y_E \quad h]^T$, the derivative of the state vector is, $\dot{\mathbf{x}} = [\dot{u} \quad \dot{v} \quad \dot{w} \quad \dot{\phi} \quad \dot{\theta} \quad \dot{\psi} \quad \dot{x}_E \quad \dot{y}_E \quad \dot{h}]^T$. The final state vector function, f, representing the aircraft translational, rotational and position kinematics are as follows:

Translational kinematics:

$$\begin{aligned} \dot{u} &= rv - qw - gsin\theta + a_x, \\ \dot{v} &= pw - ru + gcos\theta sin\phi + a_y, \\ \dot{w} &= qu - pv + gcos\theta cos\phi + a_z. \end{aligned} \tag{4.3}$$

Rotational kinematics:

$$\begin{aligned} \dot{\phi} &= p + (qsin\phi + rcos\phi)tan\theta, \\ \dot{\theta} &= qcos\phi - rsin\phi, \\ \dot{\psi} &= (qsin\phi + rcos\phi)sec\theta. \end{aligned} \tag{4.4}$$

Position kinematics:

$$\begin{aligned} \dot{x}_E &= ucos\theta cos\psi + v(sin\phi sin\theta cos\psi - cos\phi sin\psi) + w(cos\phi sin\theta cos\psi + sin\phi sin\psi), \\ \dot{y}_E &= ucos\theta sin\psi + v(sin\phi sin\theta sin\psi + cos\phi cos\psi) + w(cos\phi sin\theta sin\psi - sin\phi cos\psi), \\ \dot{h} &= -\dot{z}_E = usin\theta - vsin\phi cos\theta - wcos\phi cos\theta. \end{aligned} \tag{4.5}$$

The Kalman filtering exercise starts with aircraft at steady state, hence the initial state conditions, $\mathbf{x}_o$ are taken as trim conditions.

4.1.2 Output equations

The output equations give the relationship between the aircraft measured quantities and the state vector in the kinematic equations. As discussed in Section 1.7, typical aircraft sensors are accelerometer, rate gyro, flow vane and altimeter. The output equations are unique to the available aircraft sensors. For this study, the measured vector is given by:

$$\mathbf{y}_{measured} = [V \quad \beta \quad \alpha \quad a_x \quad a_y \quad a_z \quad q \quad p \quad r \quad x_E \quad y_E \quad h]^T. \tag{4.6}$$

The measured values a_x, a_y, a_z, p, q and r are considered as the inputs of the kinematic equation; as such are not included in the observation vector. The observation vector is hence given by, $\mathbf{y} = [V \quad \beta \quad \alpha \quad x_E \quad y_E \quad h]$. The relationship between the measured quantities and the state, also known as the observation function, h, is given by:

$$\begin{aligned} V &= \sqrt{u^2 + v^2 + w^2}, \\ \alpha &= tan^{-1}\left(\frac{w}{u}\right), \\ \beta &= sin^{-1}\left(\frac{v}{\sqrt{u^2 + v^2 + w^2}}\right). \end{aligned} \tag{4.7}$$

There is a direct relationship between the measured position quantities and the position in the state vector, as such the position component of the output vector is simply given by Equation (4.8).

$$\begin{aligned} x_E &= x_E \\ y_E &= y_E \\ h &= -z_E \end{aligned} \tag{4.8}$$

4.2 Noise Considerations

The general non-linear state-space system is given by Equation (4.9). The variables $\mathbf{w}$ and $\mathbf{v}$ represent the process and measurement noise respectively, and are considered to be non-additive noise in this equation.

$$\dot{\mathbf{x}}_k = f(\mathbf{x}_{k-1}, \mathbf{u}_k, \mathbf{w}_k) \tag{4.9}$$
$$\mathbf{y}_k = h(\mathbf{x}_k, \mathbf{u}_k, \mathbf{v}_k)$$

The noise vectors are usually assumed to be additive to simplify calculations; this results in Equation (4.10):

$$\dot{\mathbf{x}}_k = f(\mathbf{x}_{k-1}, \mathbf{u}_k) + \mathbf{w}_k, \tag{4.10}$$
$$\mathbf{y}_k = h(\mathbf{x}_k, \mathbf{u}_k) + \mathbf{v}_k.$$

Rhudy et al., [63] used data from multiple flight tests and simulations to compare these two noise assumptions. They established that there was a small difference between the results obtained from the two noise assumptions. The authors however recommend that the non-additive noise assumption be used in Kalman filtering exercises because it represents the noise characteristics of a system more accurately, and performs slightly better than the additive noise assumptions. Consequently, a non-additive noise assumption is made in this study. The non-additive noise assumption is tackled by augmenting the noise vector and its corresponding covariance vector to the state and its covariance vector respectively; this is further discussed in Sections 4.3 and 4.4.

4.3 The Unscented Kalman Filter

The unscented Kalman filter makes use of the unscented transformation (UT) to estimate the parameters of non-linear models. It utilises statistical linearisation rather than the linearisation of a dynamic model. The UT uses sigma-points constructed from the *a priori* known state condition, x_{k-1}, to give the true state distribution, x_k. These sigma-points are first transformed by feeding them through both the state and observation vector functions. The transformed sigma-points are then used to predict the *a posteriori* state condition, which in turn is used to calculate the full-filtered state vector. The step by step procedure for the UKF is discussed in this section [44].

Step 1: Calculate scaling parameters and weights vectors
The sigma-points are constructed with the aid of scaling parameters. These parameters, α, β and κ influence the spread of the sigma-points. The primary scaling parameter, α varies between 1 and 1×10^{-4}. A larger α gives a wide spread of the sigma-points, whilst a smaller α gives a narrower spread. The default primary parameter is set to 1. The secondary scaling factor, β, is used to consolidate the prior state distribution, it is usually set to 2 which is the optimum value for a Gaussian distribution. The tertiary scaling parameter, κ, is used to reduce the predicted errors. This parameter can be fine-tuned, the optimal value of κ is

$3 - L$, for $L < 3$, otherwise κ is set to 0 [44, 64, 65]. L is the length of the state vector. In many studies, the default value of κ is 0 [44, 62]. The three parameters are used to calculate a fourth scaling parameter λ, as shown in Equation (4.11). These scaling parameters are assumed to be constant throughout the filtering exercise [44]:

$$\lambda = \alpha^2(L + \kappa) - L. \tag{4.11}$$

The scaling parameters; α, β, κ and λ are used to determine weight vectors. The vectors are used to give the weighted average of the predicted mean state and observation vectors. These weight vectors are given by:

$$\eta_0^m = \frac{\lambda}{L + \lambda}, \tag{4.12}$$

$$\eta_0^c = \frac{\lambda}{L + \lambda} + 1 - \alpha^2 + \beta,$$

$$\eta_i^m = \eta_i^c = \frac{1}{2(L + \lambda)} \qquad i = 1, ..., 2L. \tag{4.13}$$

Step 2: Determine noise covariance vector Q_k and R_k
The processes and measurement noise vectors, w_k and v_k are assumed to be independent of each other, white and Gaussian in nature with covariance matrices Q_k and R_k respectively [44, 62, 64]. The process and measurement covariances, Q_k and R_k are given by:

$$Q_k = E[w_k w_k^T], \tag{4.14}$$

$$R_k = E[v_k v_k^T].$$

In this study it is assumed that there is no prior knowledge of both noise distributions; as such the values of the covariances Q_k and R_k are assumed to be unknown. An initial estimate is given for the first step.

Step 3: Initialise state and covariance values for $i = 0$
The UAV model is initially in straight and level flight prior to the initiation of loss of control. As such the initial state vector, x_0 for the Kalman filter are the aircraft trim conditions presented in Section 3.2. The choice of initial state error covariance matrix, P_0, is significant. A small initial estimate of P_0 shows high confidence in the initial condition, x_0. Whilst a larger P_0, infers high uncertainty in x_0.

$$\begin{aligned} \hat{x_0} &= x_{trim} = E[x_0] \\ P_0 &= E[(x_0 - \hat{x_0})(x_0 - \hat{x_0})^T] \end{aligned} \tag{4.15}$$

These initial estimates are used as the *a priori* estimation, x_{k-1}, for the first step of the filtering exercise. It should be noted that since it is assumed that the noise is non-additive, the state vector is augmented to the process and measurement noise vectors. The augmented state vector is hence given as:

$$x_k^a = \begin{bmatrix} x_k \\ w_k \\ v_k \end{bmatrix}. \tag{4.16}$$

Similarly, the state vector covariance is augmented to the process and measurement noise vectors, Q_k and R_k. It should be noted that the new value of L is the sum of the state, process noise, and measurement noise vectors:

$$P_x^a = \begin{bmatrix} P_k & 0 & 0 \\ 0 & Q_k & 0 \\ 0 & 0 & R_k \end{bmatrix}. \tag{4.17}$$

Step 4: Generate sigma-points

The state vector and scaling parameters are used to construct the state and noise sigma-points:

$$\chi_{k-1}^a = \begin{bmatrix} \chi_{k-1}^x \\ \chi_{k-1}^w \\ \chi_{k-1}^v \end{bmatrix} = \begin{bmatrix} \hat{x}_{k-1}^a & \hat{x}_{k-1}^a + \sqrt{L+\lambda}\sqrt{P_{k-1}^a} & \hat{x}_{k-1}^a - \sqrt{L+\lambda}\sqrt{P_{k-1}^a} \end{bmatrix}, \tag{4.18}$$

where $\sqrt{P_{k-1}^a}$ is given by Equation (4.19). The process and measurement noise vectors are independent of each other. As such there are no non-diagonal components to the P_{k-1}^a matrix:

$$\sqrt{P_{k-1}^a} = \begin{bmatrix} \sqrt{P_{k-1}} & 0 & 0 \\ 0 & \sqrt{Q_{k-1}} & 0 \\ 0 & 0 & \sqrt{R_{k-1}} \end{bmatrix}. \tag{4.19}$$

Step 5: Prediction transformation

The augmented sigma-points vector, χ_{k-1}^a is split into the state, process and measurement noise sigma-points. The state and process sigma-points are then propagated in the kinematic equation, f, derived in Section 4.1.1; producing the transformed state sigma-points. A new state vector mean is calculated from the transformed sigma-points matrix and weighted vectors. The corresponding state-vector covariance matrix is given in Equation (4.22). These

are the *a priori* conditions for this filtering exercise.

$$\chi^{x,(i)}_{k|k-1} = f\left(\chi^{x,(i)}_{k-1}, u_{k-1}, \chi^{w,(i)}_{k-1}\right), \quad i = 0, 1, ..., 2L \tag{4.20}$$

$$\hat{x}_{k|k-1} = \sum_{i=0}^{2L} \eta_i^m \chi^{(i)}_{k|k-1} \tag{4.21}$$

$$P_{k|k-1} = \sum_{i=0}^{2L} \eta_i^c \left(\chi^{x,(i)}_{k|k-1} - \hat{x}_{k|k-1}\right)\left(\chi^{x,(i)}_{k|k-1} - \hat{x}_{k|k-1}\right)^T, \quad i = 0, 1, ..., 2L \tag{4.22}$$

Step 6: Observation update

The output sigma-points vector is generated by propagating the state vector and measurement sigma-points through the output equations derived in Section 4.1.2. This is the transformed output sigma-points matrix:

$$\psi^i_{k|k-1} = h\left(\chi^{x,(i)}_{k|k-1}, u_k, \chi^{v,(i)}_{k-1}\right), \quad i = 0, 1, ..., 2L. \tag{4.23}$$

The transformed output sigma-points matrix are used to determine the updated output, output covariance and cross covariance matrix with the use of weighted vectors, η_i^m and η_i^c:

$$\hat{y}_{k|k-1} = \sum_{i=0}^{2L} \eta_i^m \psi^{(i)}_{k|k-1}, \tag{4.24}$$

$$P^{yy}_k = \sum_{i=0}^{2L} \eta_i^c \left(\psi^{(i)}_{k|k-1} - \hat{y}_{k|k-1}\right)\left(\psi^{(i)}_{k|k-1} - \hat{y}_{k|k-1}\right)^T, \qquad i = 0, 1, ..., 2L, \tag{4.25}$$

$$P^{xy}_k = \sum_{i=0}^{2L} \eta_i^c \left(\chi^{(i)}_{k|k-1} - \hat{x}_{k|k-1}\right)\left(\psi^{(i)}_{k|k-1} - \hat{y}_{k|k-1}\right)^T, \qquad i = 0, 1, ..., 2L. \tag{4.26}$$

Step 7: Measurement update

The output covariance and cross covariance matrices are then used to calculate the Kalman gain; which in turn is used to determine the *a posteriori* state and covariance matrices. The Kalman gain is used to scale the difference between the actual measured output values, z_k and the statistically predicted output value $\hat{y}_{k|k-1}$:

$$K_k = P^{xy}_k \left(P^{yy}_k\right)^{-1}, \tag{4.27}$$

$$\hat{x}_k = \hat{x}_{k|k-1} + K_k\left(z_k - \hat{y}_{k|k-1}\right), \tag{4.28}$$

$$P_k = P_{k|k-1} - K_k P^{yy}_k K_k^T. \tag{4.29}$$

The *a posteriori* values are then used in the next filtering step as the previous estimate; x_k becomes x_{k-1} and P_k, P_{k-1}. These vectors are re-augmented with the noise and covariance

vectors to account for the non-additive noise. The values of the process and measurement noise are always set to 0 [66]. The method described in this section is then repeated for the rest of the time steps. Figure 13 shows a simplified schematic overview of the unscented Kalman filter.

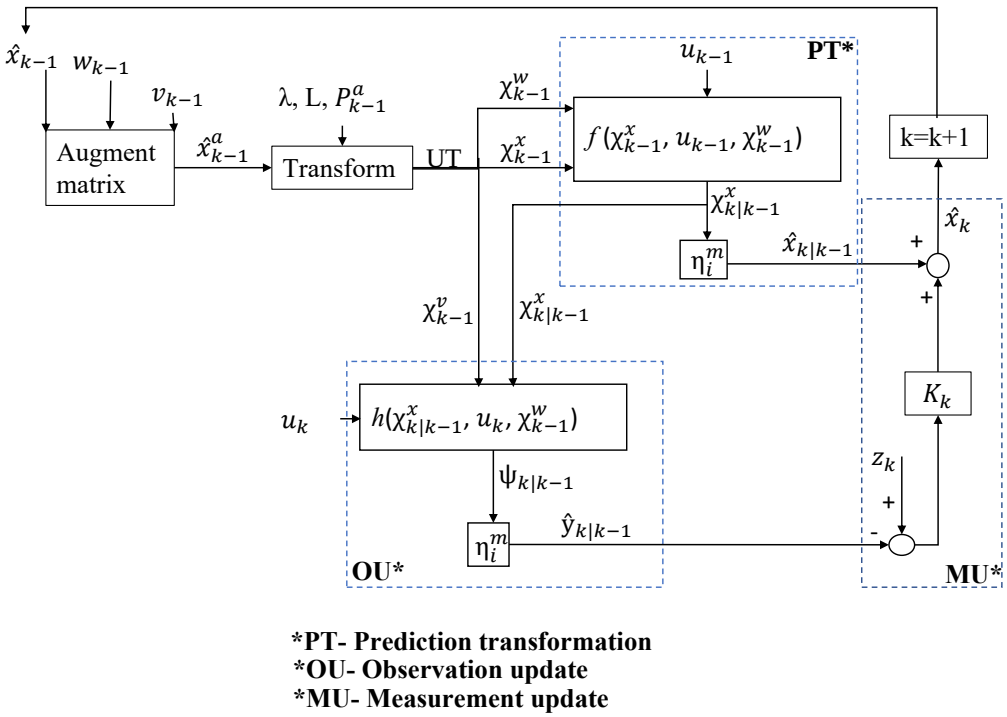

Figure 13: An overview of the unscented Kalman filtering procedure.

4.4 The Cubature Kalman Filter

The cubature Kalman filter is the closest approximation to the Bayesian filter. It utilises integration to estimate the state vector and the corresponding state vector covariance matrices [42, 44, 67]. The key assumption to the cubature filter is that the state vector follows a normal distribution, $x_k = N(\hat{x}_{k|k}, P_{k|k})$. When calculating the *a priori* conditions $x_{k|k-1}$, the following integration is solved:

$$\hat{x}_{k|k-1} = \int_{\Re^n} f(x_{k-1}, u_{k-1}) N(x_{k-1}, \hat{x}_{k-1|k-1}, P_{k-1|k-1}) dx_{k-1}, \tag{4.30}$$

where $f(x_{k-1}, u_{k-1})$ is the kinematic equation. Similar expressions can be derived for $P_{k|k-1}$, $\hat{y}_k$, $P^{zz}_{k|k-1}$ and $P^{xz}_{k|k-1}$. To calculate the values of the integrals, these integrations are transformed into spherical-radial integration form and the spherical-radial rule is applied. Work done by Arasaratnam shows how this transformation is done [42]. Numerical integration is used to approximate the values of $\hat{x}_{k|k-1}$, $P_{k|k-1}$, $\hat{y}_k$, $P^{zz}_{k|k-1}$ and $P^{xz}_{k|k-1}$. Like in the unscented

Kalman filter, an augmented state and covariance vector is formulated for the cubature Kalman filter to deal with non-additive noise [68]. The following steps are taken during cubature Kalman filtering:

Step 1: Initialise the state vector and the corresponding covariance vector
As in the unscented Kalman filtering case, the initial values of the state and covariance vectors are assumed to be known and taken as the trim conditions. These initial conditions are taken as the *a priori* conditions, $x_0 = \hat{x}_{k-1|k-1}$ and $P_0 = P_{k-1|k-1}$. The Cholesky decomposition is used to factorise the state covariance in order to generate the square root of $P_{k-1|k-1}$. The square root of the augmented covariance matrix $P^a_{k-1|k-1}$, is denoted as $S^a_{k-1|k-1}$, this factorisation is given by:

$$P^a_{k-1|k-1} = S^a_{k-1|k-1} S^{aT}_{k-1|k-1}. \tag{4.31}$$

Step 2: Generate cubature sigma-points
The state vector and square root of the state covariance are used to construct cubature sigma-points. The cubature points ξ_i are as a result of the numerical integration which is derived in Arasaratnam's work [42]:

$$\xi_i = \begin{cases} \sqrt{n}\mathbf{e}_i, & i = 1, 2, 3, ..., n, \\ -\sqrt{n}\mathbf{e}_{i-1}, & i = n+1, n+2, n+3, ..., 2n, \end{cases} \tag{4.32}$$

$$\chi^a_{i,k-1|k-1} = S^a_{k-1|k-1}\xi_i + \hat{x}^a_{k-1|k-1} \qquad i = 1, 2, ..., m \quad where \quad m = 2L. \tag{4.33}$$

where $\mathbf{e}_i$ and $\mathbf{e}_{i-1}$ are generators that are in the form of unit vectors with 1 at the ith and $(i-1)$th positions respectively [68, 69, 70]. For example, $\mathbf{e} \in \mathbf{R}^n$ is given as:

$$\left\{ \begin{pmatrix} 1 \\ 0 \\ \vdots \\ 0 \end{pmatrix}_1, \begin{pmatrix} 0 \\ 1 \\ \vdots \\ 0 \end{pmatrix}_2, \cdots, \begin{pmatrix} 0 \\ 0 \\ \vdots \\ 1 \end{pmatrix}_n, \begin{pmatrix} -1 \\ 0 \\ \vdots \\ 0 \end{pmatrix}_{n+1}, \begin{pmatrix} 0 \\ -1 \\ \vdots \\ 0 \end{pmatrix}_{n+2}, \cdots, \begin{pmatrix} 0 \\ 0 \\ \vdots \\ -1 \end{pmatrix}_{2n} \right\}. \tag{4.34}$$

Step 3: Propagate the cubature sigma-points
The augmented cubature sigma-points are split into the state, process and measurement noise sigma-points. The state cubature sigma-points along with the input vector are then propagated into the input function. These new generated points are then used to construct the non-augmented predicted state, $\hat{x}_{k|k-1}$ with the aid of the cubature point weight ω_i:

$$\chi^*_{i,k|k-1} = f(\chi_{i,k-1|k-1}, u_{k-1}) \qquad i = 1, 2, ..., m, \tag{4.35}$$

$$\hat{x}_{k|k-1} = \omega_i \sum_{i=1}^{m} \chi^*_{i,k|k-1}, \tag{4.36}$$

where $\omega_i = \frac{1}{m}$.

Step 4: Estimate the predicted state error covariance

The predicted state, cubature point weight and process covariance are used to estimate the predicted state error covariance:

$$P_{k|k-1} = \omega_i \sum_{i=1}^{m} \chi^*_{i,k|k-1} \chi^{*T}_{i,k|k-1} - \hat{x}_{k|k-1} \hat{x}^T_{k|k-1}. \tag{4.37}$$

Step 5: Observation update

The predicted state and covariance vectors are then used to calculate the measurement cubature points:

$$P_{k|k-1} = S_{k|k-1} S^T_{k|k-1}, \tag{4.38}$$

$$\chi_{i,k|k-1} = S_{k|k-1} \xi_i + \hat{x}_{k|k-1} \qquad i = 1, 2, ..., m, \tag{4.39}$$

$$\psi_{i,k|k-1} = \mathbf{h}(\chi_{i,k|k-1}, u_k) \qquad i = 1, 2, ..., m, \tag{4.40}$$

$$\hat{y}_{k|k-1} = \omega_i \sum_{i=1}^{m} \psi_{i,k|k-1}, \tag{4.41}$$

$$P_{zz,k|k-1} = \omega_i \sum_{i=1}^{m} \psi_{i,k|k-1} \psi^T_{i,k|k-1} - \hat{y}_{k|k-1} \hat{y}^T_{k|k-1}. \tag{4.42}$$

The cross variance is also calculated:

$$P_{xz,k|k-1} = \omega_i \sum_{i=1}^{m} \chi_{i,k|k-1} \psi^T_{i,k|k-1} - \hat{x}_{k|k-1} \hat{y}^T_{k|k-1}. \tag{4.43}$$

Step 6: Measurement update

The cubature Kalman gain is calculated from the output covariance, and cross covariance. This Kalman gain is then used to determine the *a posteriori* state and state covariance vectors that are used as the previous conditions in the next step of the cubature Kalman filter. Similarly, these vectors are re-augmented with the noise and covariance vectors to account for the non-additive noise in the next time step.

$$K_k = P_{xz,k|k-1} P^{-1}_{zz,k|k-1} \tag{4.44}$$

$$\hat{x}_{k|k} = \hat{x}_{k|k-1} + K_k (z_k - \hat{y}_{k|k-1}) \tag{4.45}$$

$$P_{k|k} = P_{k|k-1} - K_k P_{zz,k|k-1} K_k^T \tag{4.46}$$

A simplified schematic overview of the cubature Kalman filter is shown in Figure 14.

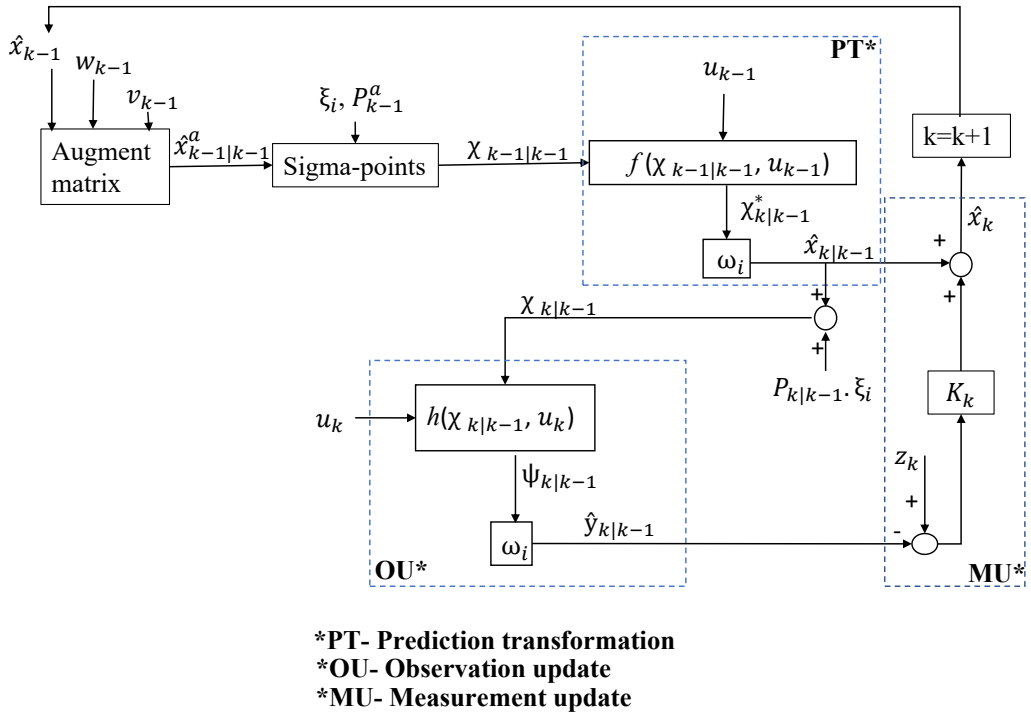

Figure 14: An overview of the cubature Kalman filtering procedure.

4.5 Parameter Estimation

After employing the Kalman filters to reconstruct the state of the GTM T2 UAV, these states are used to calculate unknown parameters at the point of LOC and after LOC has occurred. The states calculated by both the UKF and the CKF are used to calculate the force and moment coefficients: C_x, C_y, C_z, C_l, C_m and C_n; that can then be used to determine the control surface deflection experienced by the GTM UAV. The following equations are solved simultaneously to determine δ_e, δ_a and δ_r:

$$\begin{aligned} 0 = &-C_x(\alpha, \delta_e) - a_0 + a_1\alpha + a_2\alpha^2 - a_3\alpha^3 - a_4\alpha^4 + a_5\alpha^5 + \frac{q\bar{c}(a_6 + a_7\alpha + a_8\alpha^2)}{2V} + a_9\alpha\delta_e \\ &+ a_{10}\alpha^3\delta_e - a_{11}\alpha^5\delta_e - a_{12}\delta_e^2 + a_{13}\alpha^2\delta_e^2 - a_{14}\alpha^4\delta_e^2 - a_{15}\alpha\delta_e^3 + a_{16}\alpha^3\delta_e^3 - a_{17}\alpha^5\delta_e^3, \end{aligned} \tag{2.8}$$

$$0 = -C_y(\beta, \alpha, \delta_r) - b_0\beta + b_1\beta^3 + \frac{rb(b_2 + b_3\alpha + b_4\alpha^2)}{2V} + \frac{pb(b_5\alpha + b_6\alpha^2 - b_7\alpha^3)}{2V} + b_8\delta_r, \tag{2.9}$$

$$0 = -C_z(\alpha, \delta_e) - c_0 - c_1\alpha + c_2\alpha^2 - c_3\alpha^3 - c_4\alpha^4 + c_5\alpha^5 + \frac{q\bar{c}(-c_6 - c_7\alpha - c_8\alpha^2)}{2V} - c_9\delta_e \\ - c_{10}\alpha^2\delta_e + c_{11}\alpha^4\delta_e - c_{12}\alpha\delta_e^2 + c_{13}\alpha^3\delta_e^2 - c_{14}\alpha^5\delta_e^2 + c_{15}\delta_e^3 - c_{16}\alpha^2\delta_e^3 + c_{17}\alpha^4\delta_e^3, \tag{2.10}$$

$$0 = -C_l(\beta, \alpha, \delta_r, \delta_a) - d_0\beta - d_1\alpha\beta + d_2\beta^3 - d_3\beta^5 + \frac{rb(d_4 + d_5\alpha + d_6\alpha^2)}{2V} \\ + \frac{pb(-d_7 - d_8\alpha + d_9\alpha^2 + d_{10}\alpha^4)}{2V} - d_{11}\delta_a + d_{12}\delta_r, \tag{2.11}$$

$$0 = -C_m(\alpha, \beta, \delta_e) + e_0 - e_1\alpha - e_2\beta^4 + \frac{q\bar{c}(-e_3 + e_4\alpha + e_5\alpha^2)}{2V} - e_6\delta_e - e_7\alpha\beta^2 - e_8\beta^3, \tag{2.12}$$

$$0 = -C_n(\alpha, \beta, \delta_r) + f_0 - f_1\beta^3 + \frac{rb(-f_2 - f_3\alpha - f_4\alpha^2)}{2V} + \frac{pb(-f_5 - f_6\alpha + f_7\alpha^2 + f_8\alpha^3)}{2V} \\ - f_9\delta_r + f_{10}\beta\delta_r. \tag{2.13}$$

The Newton-Raphson method is used to determine the values of the δ_e, δ_a and δ_r deflections. The polynomial coefficients of these functions a_n, b_n, c_n, d_n, e_n and f_n are given in Appendix 1 and the values of p, q and r, α, β and V are reconstructed by the UKF and CKF. The general formula for the Newton-Raphson method is given in Equation (4.47). In the case of δ_a and δ_r, the equations are coupled. The Newton-Raphson method for multiple variables is used to solve for δ_a and δ_r, the general formula is given in Equation (4.48). X_{n+1} and X_n are the consecutive control surface deflections calculated in the iterative method, $f(X_n)$ is the set of force and moment equations stated in Equations (2.8) to (2.13) and $J(X_n)$ is the Jacobian matrix of these expressions respectively:

$$X_{n+1} = X_n + \frac{f(X_n)}{f'(X_n)}, \tag{4.47}$$

$$X_{n+1} = X_n + [J(X_n)]^{-1}.f(X_n). \tag{4.48}$$

5 Verification and Validation of Simulation Model and Kalman Filters

Results obtained from the MATLAB simulation model are compared to published data for verification and validation in this chapter. Verification checks if the mathematical model in the MATLAB simulation is representative of the different flight regimes. Results obtained from the simulation will be compared to the general response expected from a 6 DOF simulation of its nature. It should be noted that verification and validation of the aircraft simulation is carried out on a clean aircraft model that does not include the control system, because the controller alters the general dynamics of an aircraft. Sinha and Ananthkrishan [71] provided simulation results for several flight regimes. Verification of the Kalman filters will be achieved by performing flight path reconstruction, and comparing results to the measured data obtained in the simulation. On the other hand, validation examines how realistic the MATLAB simulation and estimated results are for flight regimes. To achieve this, MATLAB simulation results are compared to flight test data obtained by Padayachee [25], and Cunningham et al., [49].

5.1 Simulation Model Verification

Two straight and level trim states are used in this verification process of the non-linear GTM T2 UAV model. Time responses obtained from various control inputs are compared to the general response expected from similar 6 DOF simulations. In this section, a series of simulation results obtained from pulse, step, doublet and sinusoidal control inputs are presented. These trim states are shown in Table 9.

Table 9: Trim states used for the model verification process

Property	Units	Trim State 1	Trim State 2
h	m	356	356
V	ms^{-1}	45.0762	35.358
α	deg	2.999	5.364
δ_T	-	0.124	0.65
δ_e	deg	4.03	5.576
δ_a	deg	2.352x10^{-8}	4.9256x10^{-8}
δ_r	deg	-1.0133 x10^{-8}	-1.9356x10^{-8}

The first trim state represents a low thrust and high velocity flight regime, whilst trim state 2 is the trim condition for high thrust and low velocity. The response to a 0.0523rad (3°) elevator step reduction applied to trim state 1 is shown in Figure 15. All the other control

inputs are held unchanged from their trimmed conditions. As expected, after the elevator step input a new stable steady-state is attained. The disturbance results in a higher angle of attack and a lower Mach number. Additionally, there are no changes in lateral-directional variables. This is consistent with results obtained by Sinha and Ananthkrishan [71] for a similar trim state.

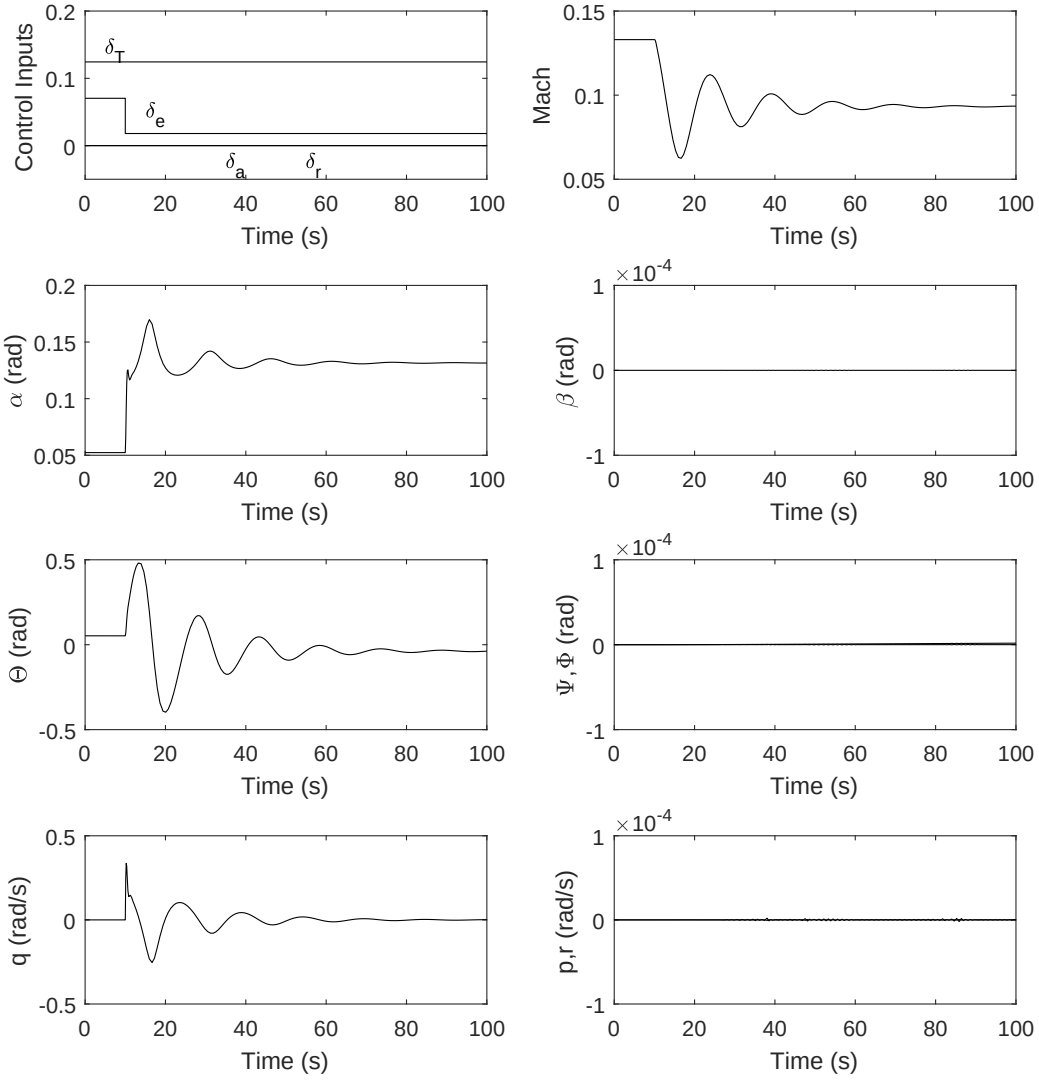

Figure 15: Response to 0.0523rad (3°) elevator step reduction with all other control inputs held unchanged from their trimmed conditions. $\delta_a, \delta_r, \delta_e$ are in rad.

A doublet aileron input of an amplitude of 0.105rad (6°) with a period of 3s is applied to trim state 2. The elevator, rudder and throttle inputs are kept unchanged. The aileron upset excited both longitudinal and lateral-directional variables. Figure 16 shows the time history obtained. Similar results are obtained by Sinha and Ananthkrishan [71].

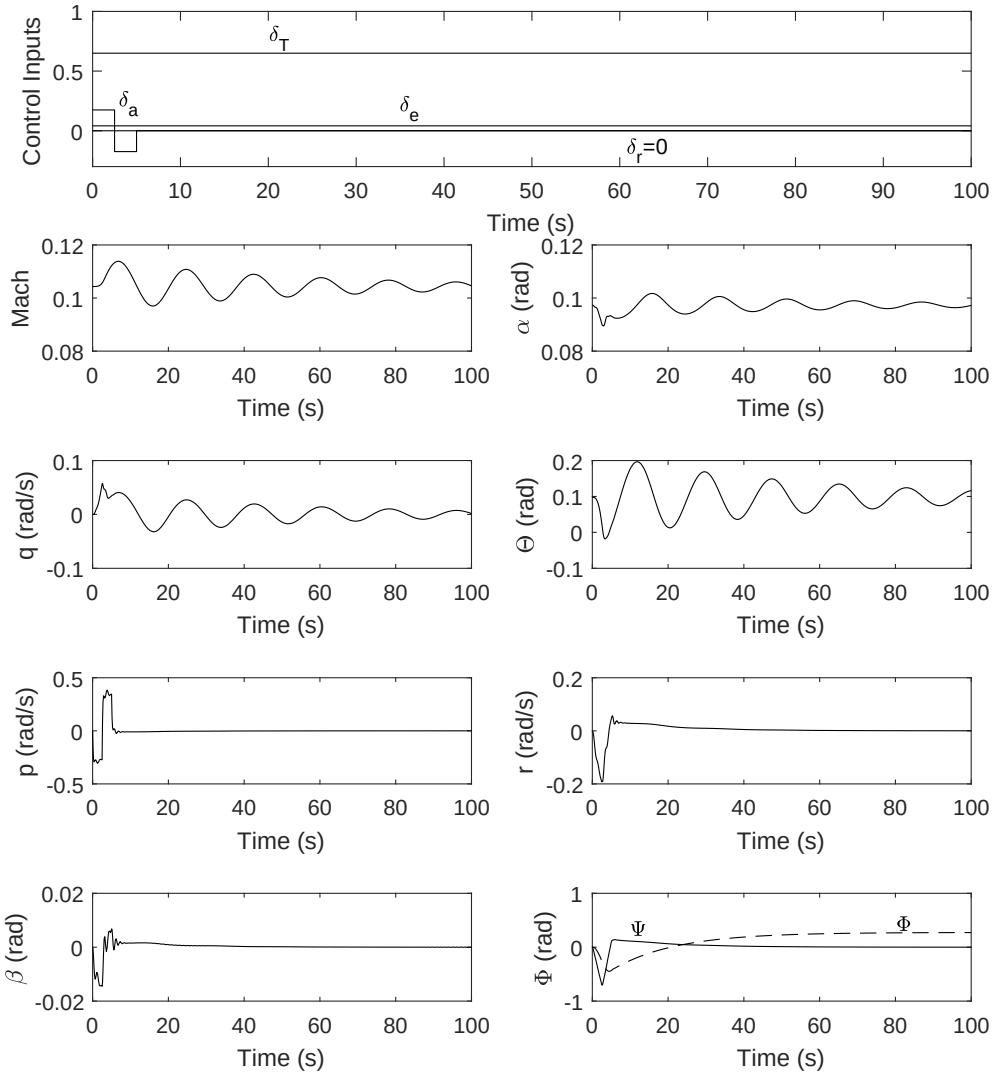

Figure 16: Response to an aileron doublet with an amplitude of 0.105rad (6°). All other control inputs held unchanged from their trimmed conditions. $\delta_a, \delta_r, \delta_e$ are in rad.

A 0.105rad (6°) step-up rudder input is introduced at t=5s to trim state 2. This manoeuvre corresponds to a hard-left rudder. The aircraft pitches down steeply, yaws and banks to the left. A new steady state is attained for each variable. This is shown in Figure 17a. A plot of the x, y and z position in Figure 17b shows that the hard-left rudder upset results in a steep spin. These time responses are consistent with those obtained by Sinha and Ananthkrishan [71].

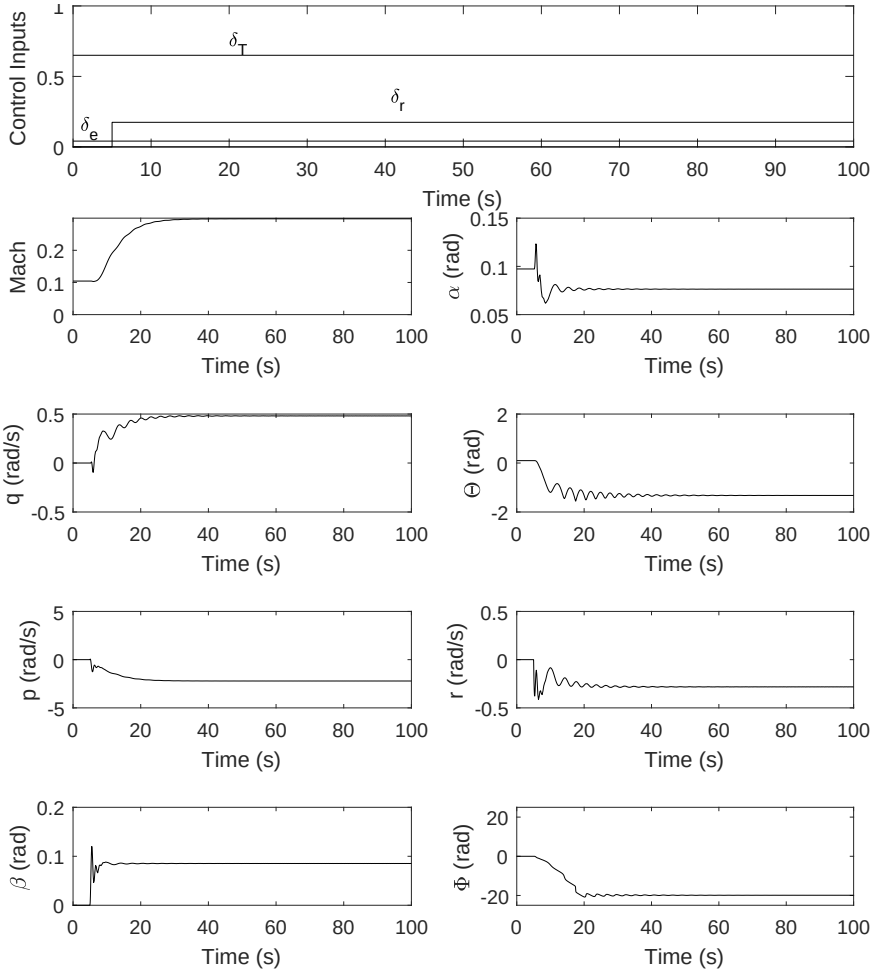

(a)

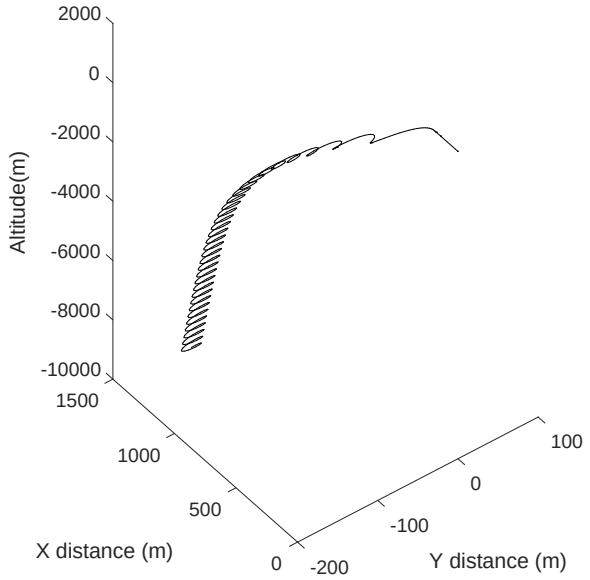

(b)

Figure 17: Response to a 0.105rad (6°) step-up rudder with all the other control inputs held unchanged from their trimmed conditions. $\delta_a, \delta_r, \delta_e$ are in rad.

A throttle step-up input is applied whilst keeping all the other inputs constant. This results in a steady climb as seen from the height, h in Figure 18a. There is a marginal change in flight path angle, speed and angle of attack. Figure 18b shows the time history of all the variables obtained from this control upset. This response is typical for a throttle step-up [71].

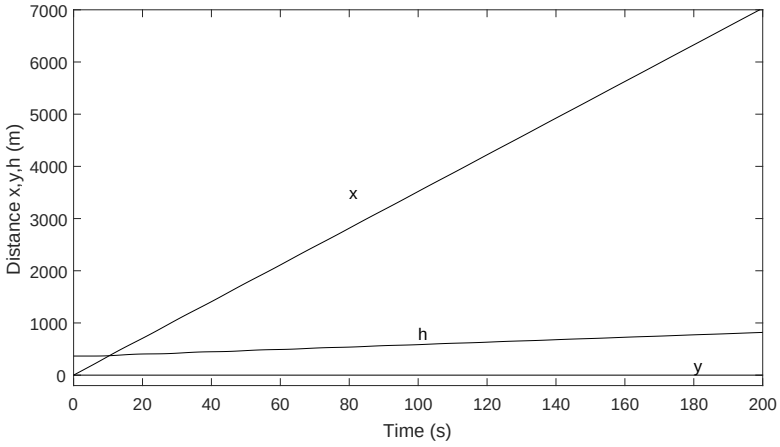

(a)

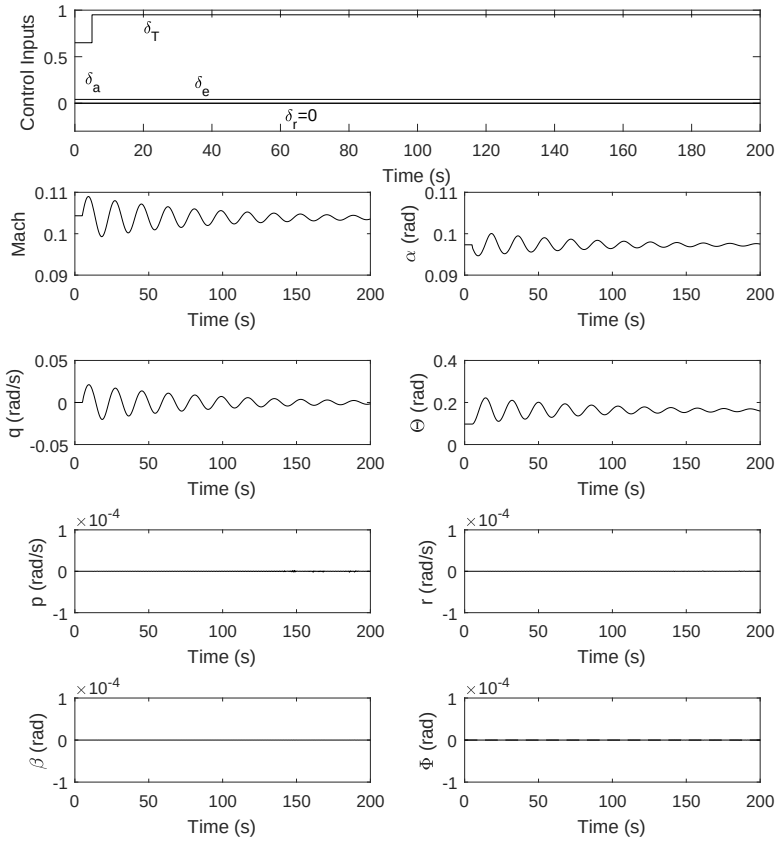

(b)

Figure 18: Response to a 30% throttle increase with all the other control inputs held unchanged from their trimmed conditions. $\delta_a, \delta_r, \delta_e$ are in rad.

5.2 Simulation Model Validation

To validate the GTM T2 UAV simulation model, the time response is compared to flight test data presented in the work done by Padayachee [25]. In his study, he provided the flight data of a quasi-steady push-over pull-up manoeuvre of a fixed wing small low-cost UAV. This manoeuvre was achieved through applying a sinusoidal elevator input of amplitude of (3°). The same was done in the GTM UAV simulation model and the results obtained are shown in Figure 19a. Figure 19b shows the UAV response to a quasi-steady push-over pull-up manoeuvre obtained flight test. A comparison of these results shows that the time responses from the simulation model are relatively similar to the flight data.

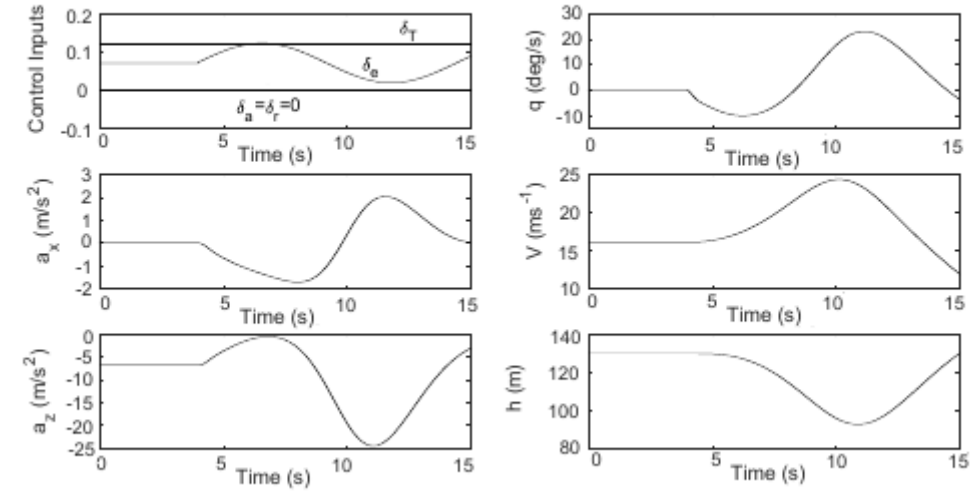

(a)

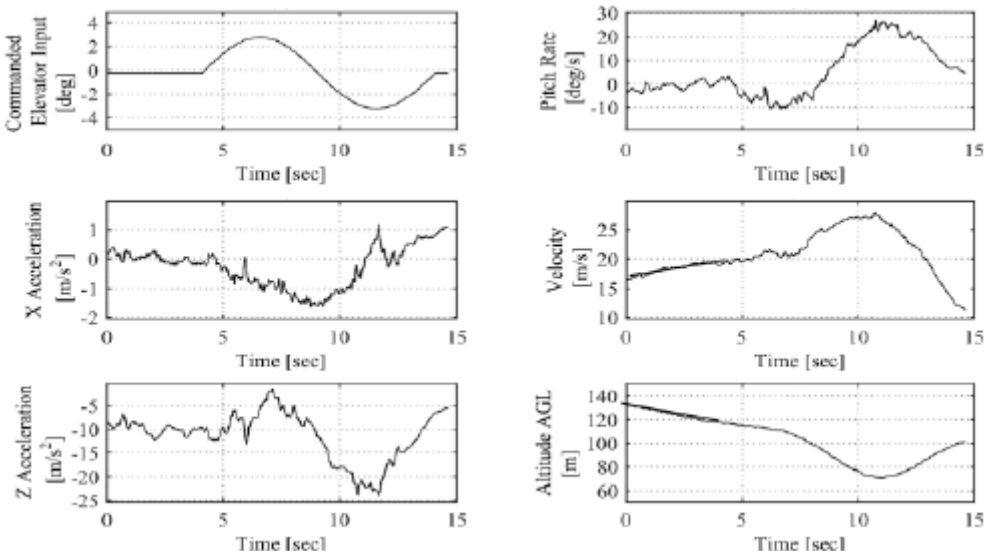

(b)

Figure 19: Quasi-steady push-over pull-up manoeuvre obtained from (a) the GTM UAV simulation model, (b) flight data [25].

Additionally, Cunningham et al., [49] provided flight data and simulation results for a yaw-roll doublet manoeuvre performed by a UAV with similar dimensions to the GTM T2. These researchers induced control upsets on a S-2 UAV which is a sub-scale, single engine jet transport aircraft. The time response obtained for this exercise is shown in Figure 20a [49]. A similar manoeuvre is performed on the GTM UAV simulation for additional validation, results are shown in Figure 20b.

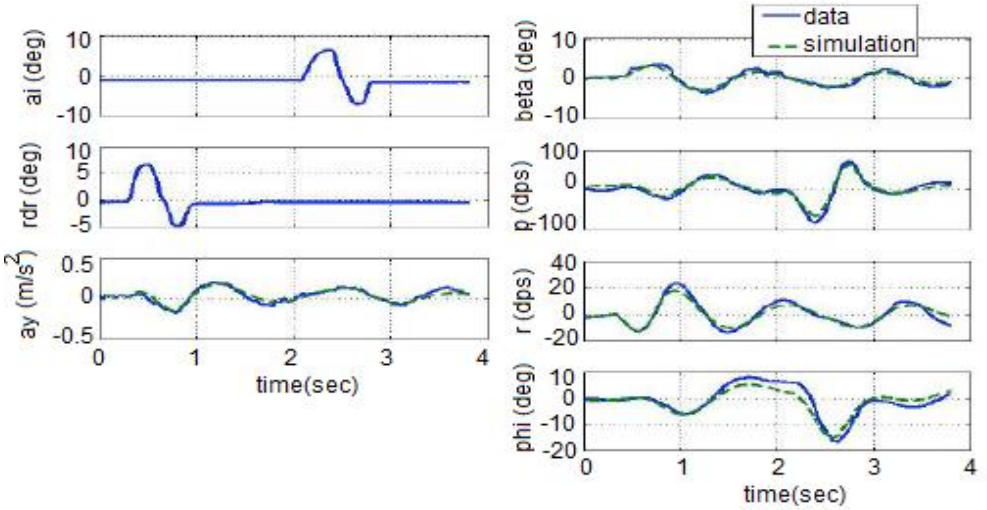

(a)

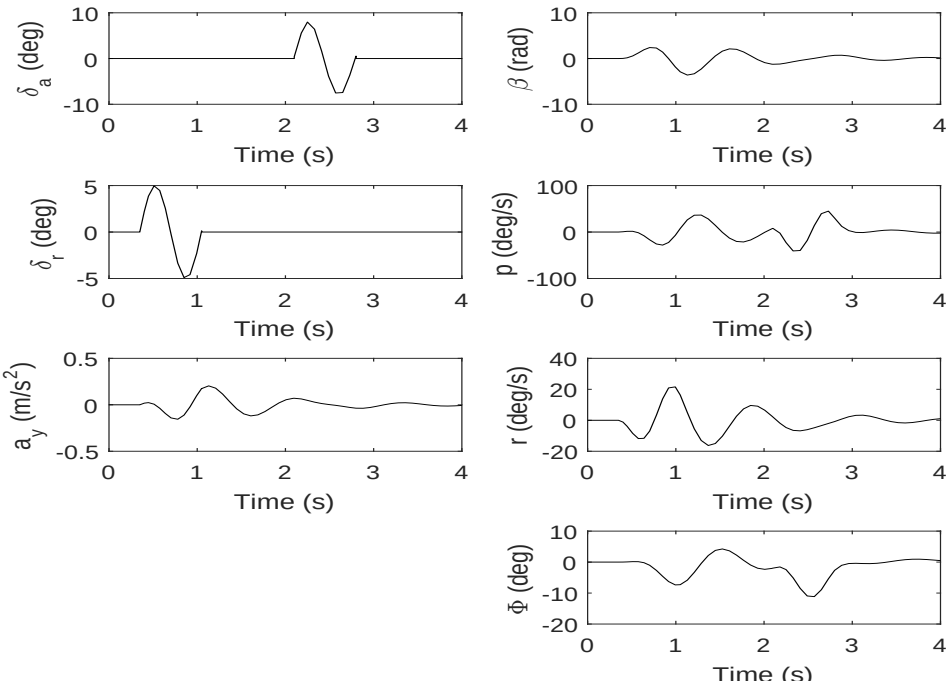

(b)

Figure 20: Time response of a yaw-roll doublet manoeuvre for (a) flight test data [49], (b) the GTM UAV simulation model.

The time response obtained from these various control input upsets is comparable to flight test data and the general expected time history of 6 DOF simulations. As such, the simulation model produces results that are similar to data measured in non-linear flight for comparable UAVs.

5.3 Kalman Filter Verification and Validation

In order to verify and measure the performance of the unscented and cubature Kalman filters, flight path reconstruction (FPR) is conducted. ARMSE values are calculated to quantify the performance of the two Kalman filters. Additionally, hypothesis testing is performed to compare the mean RMSEs of CKF and UKF reconstructed states.

5.3.1 Flight path reconstruction

The measured data obtained from the simulation model was collected for a controlled aircraft with Dryden wind disturbance. The FPR results obtained from the unscented and cubature Kalman filter are presented in Figure 21. Both filters adequately reconstructed the flight path of the GTM T2 UAV.

5.3.2 Reconstruction statistics

The mean and standard deviation values, $\bar{x}$ and s, of the state RMSEs of the CKF and UKF for one hundred independent, random Monte Carlo runs are used to test the null hypothesis $H_\circ$: $\bar{x}_{CKF} = \bar{x}_{UKF}$ against the alternative hypothesis H_1: $\bar{x}_{CKF} > \bar{x}_{UKF}$ or $\bar{x}_{CKF} < \bar{x}_{UKF}$. The general formula used in hypothesis testing for comparing sample means is given by [62]:

$$Z = \frac{\bar{x}_{CKF} - \bar{x}_{UKF}}{\sqrt{\frac{{s_{UKF}}^2}{n} + \frac{{s_{CKF}}^2}{n}}}. \tag{5.1}$$

A key assumption made when using Equation (5.1) is that the errors follow a normal distribution [62]. It is hence important to determine if the RMSE values are normally distributed [72]. Figure 22 shows the RMSE values obtained for one hundred independent Monte Carlo runs with random process and measurement noise values, w and v.

The normal distribution is bell-shaped and symmetric; this is confirmed by checking the data Kurtosis and skewness coefficients. A normal distribution has a skewness coefficient of zero and a Kurtosis of three. In order to discern if the RMSEs obtained from the Monte Carlo simulation follow a normal distribution, a frequency versus RMSE graph for each state

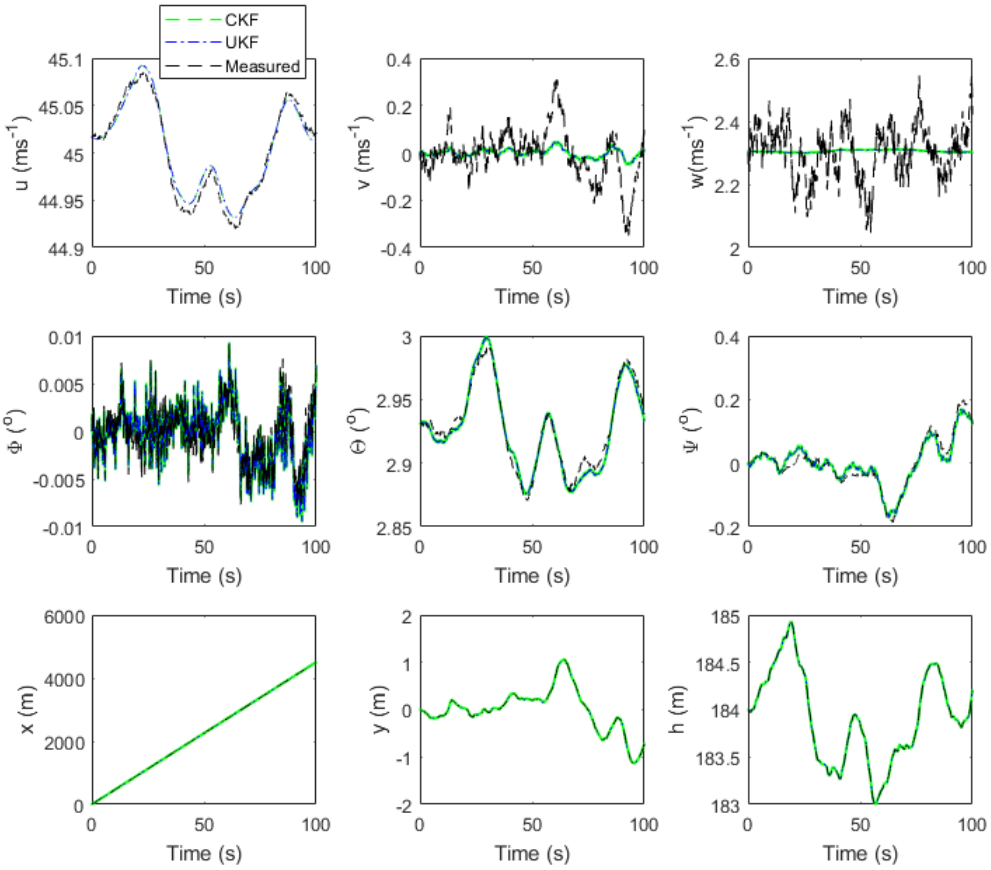

Figure 21: Flight path reconstruction results for an aircraft experiencing wind disturbance.

reconstructed using the unscented Kalman filter is presented in Figure 23, and the Kurtosis and skewness coefficients provided. A similar pattern was observed for the RMSEs obtained using data reconstructed by the cubature Kalman filter, and similar conclusions were drawn regarding the distribution of the errors. In this figure, α_1 and α_2 represent the Kurtosis and skewness coefficient respectively.

The Kurtosis coefficient defines how thick or thin the tails of the distribution are; it measures the difference between the maximum and minimum frequencies. A Kurtosis coefficient of less than three describes a distribution with thinner tails than the normal distribution, anything greater than three indicates thicker tails. The closer the skewness coefficient is to zero, the more symmetric the distribution is. The observed frequency versus RMSE data shows that though some state RMSE distributions may be approximated as normal, a majority of the RMSE distributions are highly skewed and exhibit large Kurtosis values. As a result, using Equation (5.1) for hypothesis testing is erroneous. Consequently, a non-parametric hypothesis test is to be carried out instead. One such test is the Wilcoxon two-sample rank-sum, it does not require a prior knowledge of the distribution. The Wilcoxon two-sample rank-sum test is used to compare the mean RMSE values for states reconstructed by the CKF and UKF. In this test, both data sets are combined, ranked in ascending order and the ranks added

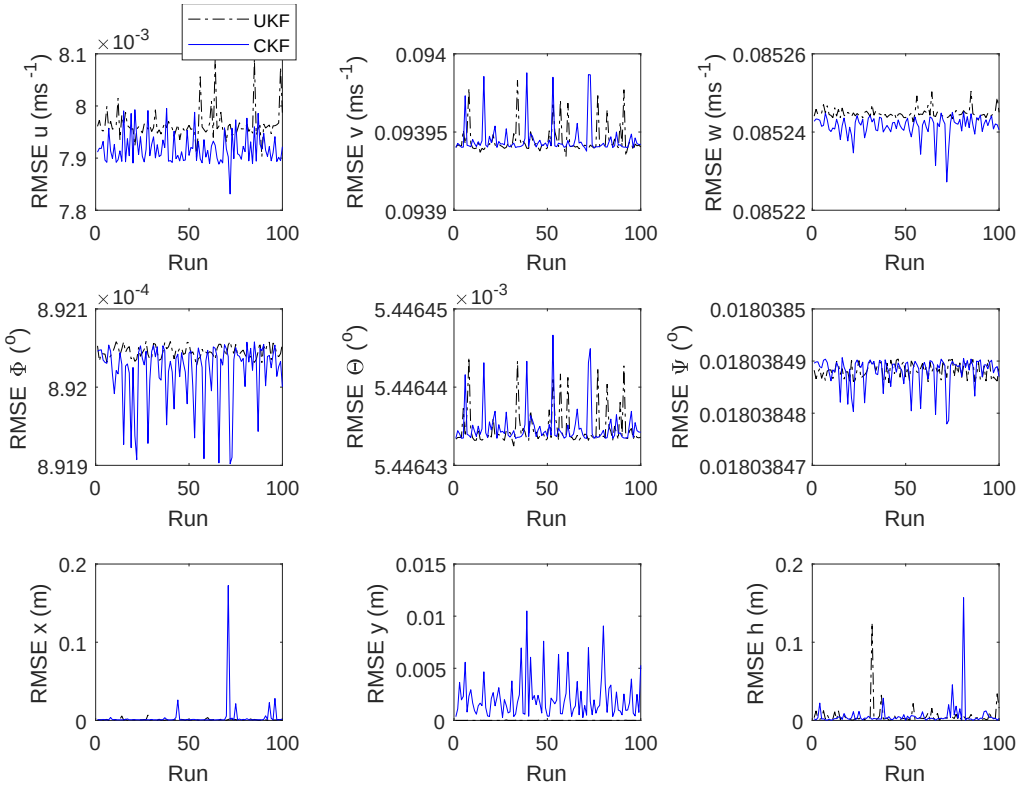

Figure 22: RMSE values obtained for one hundred independent Monte Carlo runs.

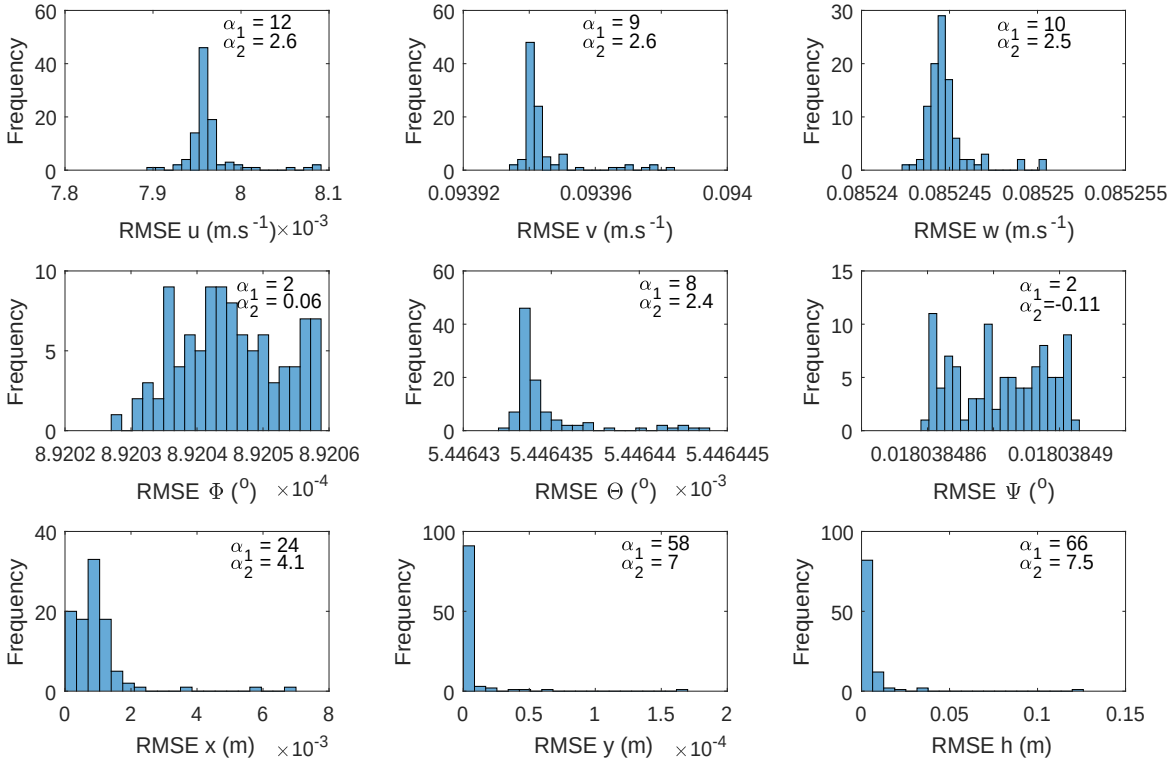

Figure 23: Frequency graph of the RMSE values obtained through the UKF

for each filter method. A mean and standard deviation of the ranks is calculated through Equation (5.2) and (5.3) respectively. The test statistic, Z, is now calculated using Equation (5.4) instead.

$$M_r = \frac{n_1(n_1 + n_2 + 1)}{2}, \tag{5.2}$$

$$\theta_r = \sqrt{\frac{n_1 n_2(n_1 + n_2 + 1)}{12}}, \tag{5.3}$$

$$Z = \frac{R_1 - M_r}{\theta_r}, \tag{5.4}$$

where n_1 and n_2 are the sample sizes of the two samples, and R_1 is the rank sum.

5.3.3 Kalman filter performance

ARMSE values provide an indication of the overall performance of the two filters. This value is however influenced by larger state measurements; in this case x, y and h states have higher-order errors as compared to those obtained in the angular states, such as ϕ, θ and ψ. As a result, hypothesis testing provides a better insight into the CKF and UKF performance when reconstructing the individual states. The Wilcoxon two-sample rank-sum hypothesis test is used to compare the performance of the UKF and CKF performance in reconstructing states presented in Section 5.3. A right-tailed test is used to determine if the performance of the CKF is inferior to that of the UKF. Whereas, a left-tailed test is used to show if the CKF is superior to that of the UKF. The decision criteria used in this study is shown in Figure 24.

Results from the Wilcoxon two-sample rank-sum hypothesis test are presented in Table 10.

Hypothesis testing revealed that at 5% level of significance, the UKF outperformed the CKF in reconstructing the states; ψ, x and y. Whilst the CKF outperformed the UKF in tracking the three states: u, w and ϕ. The filters performed equivalently for v and h states. The ARMSE values calculated for the CKF and UKF over the one hundred Monte Carlo runs to determine the overall filter performance. The RMSE values were summed up for all states, $(u, v, w, \phi, \theta, \psi, x, y, z\ )$. The ARMSE values for the CKF and UKF are 19.29 and 19.48 respectively. These values are similar and low, given the magnitudes the states, hence the overall filter performance is equivalent and adequate.

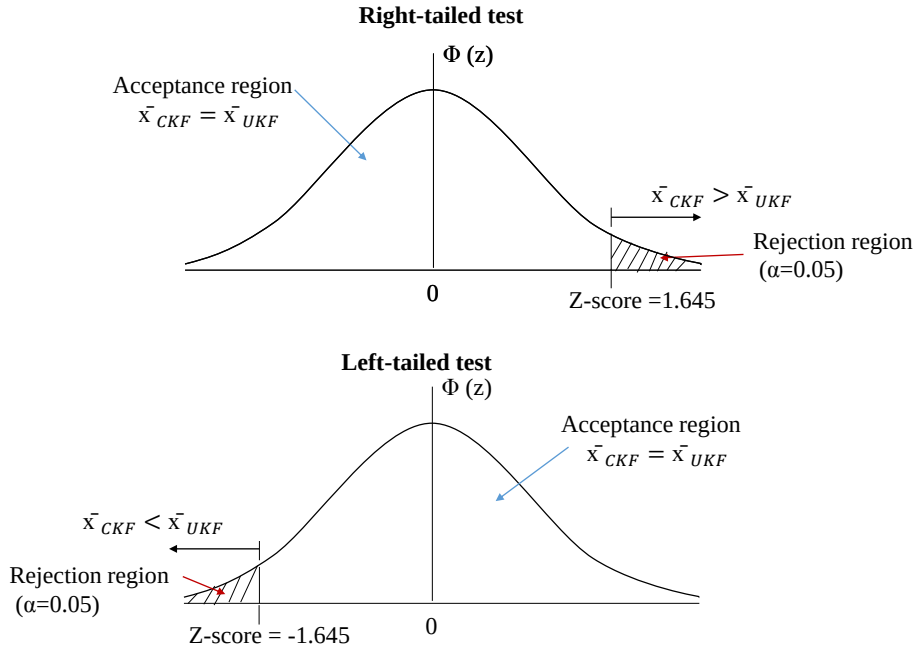

Figure 24: Decision criteria for right-tailed and left-tailed hypothesis test.

Table 10: Hypothesis tests comparing UKF and CKF performance for 0% sensor noise.

$H_\circ$: $\bar{x}_{CKF} = \bar{x}_{UKF}$

H_1: $\bar{x}_{CKF} > \bar{x}_{UKF}$ and $\bar{x}_{UKF} > \bar{x}_{CKF}$ for U, w and ϕ state only

Level of significance: 5%, $\alpha = 0.05$

Z-score = 1.645, reject $H_\circ$ if Test score > Z-score, otherwise accept $H_\circ$

State	Test score	Decision
$u\ (m.s^{-1})$	-2.85	Reject H_o, $\bar{x}_{uCKF} < \bar{x}_{uUKF}$
$v\ (m.s^{-1})$	1.37	Accept H_o, $\bar{x}_{vCKF} = \bar{x}_{vUKF}$
$w\ (m.s^{-1})$	-7.083	Reject H_o, $\bar{x}_{wCKF} < \bar{x}_{wUKF}$
$\phi\ (^\circ)$	-4.58	Reject H_o, $\bar{x}_{\phi CKF} < \bar{x}_{\phi UKF}$
$\theta\ (^\circ)$	1.35	Accept H_o, $\bar{x}_{\theta CKF} = \bar{x}_{\theta UKF}$
$\psi\ (^\circ)$	1.86	Reject H_o, $\bar{x}_{\psi CKF} > \bar{x}_{\psi UKF}$
$x\ (m)$	2.72	Reject H_o, $\bar{x}_{xCKF} > \bar{x}_{xUKF}$
$y\ (m)$	8.61	Reject H_o, $\bar{x}_{yCKF} > \bar{x}_{yUKF}$
$h\ (m)$	0.65	Accept H_o, $\bar{x}_{zCKF} = \bar{x}_{zUKF}$

6 Results and Discussion

6.1 Induced Sensor Failure

In this section FPR results are presented. The ARMSEs and RMSEs calculated from Monte Carlo runs with random coloured noise functions w and v are used to quantify and compare the performance of the CKF and UKF. Hypothesis testing is performed at 5% level of significance to determine the difference between the CKF and UKF state RMSE means.

6.1.1 Excessive sensor noise

Both filters are used to reconstruct the states of the aircraft in the presence of 0%, 2%, 5% and 10% sensor error. The flight path reconstruction results for a GTM T2 UAV experiencing both the wind disturbance and 5% sensor error are shown in Figure 25.

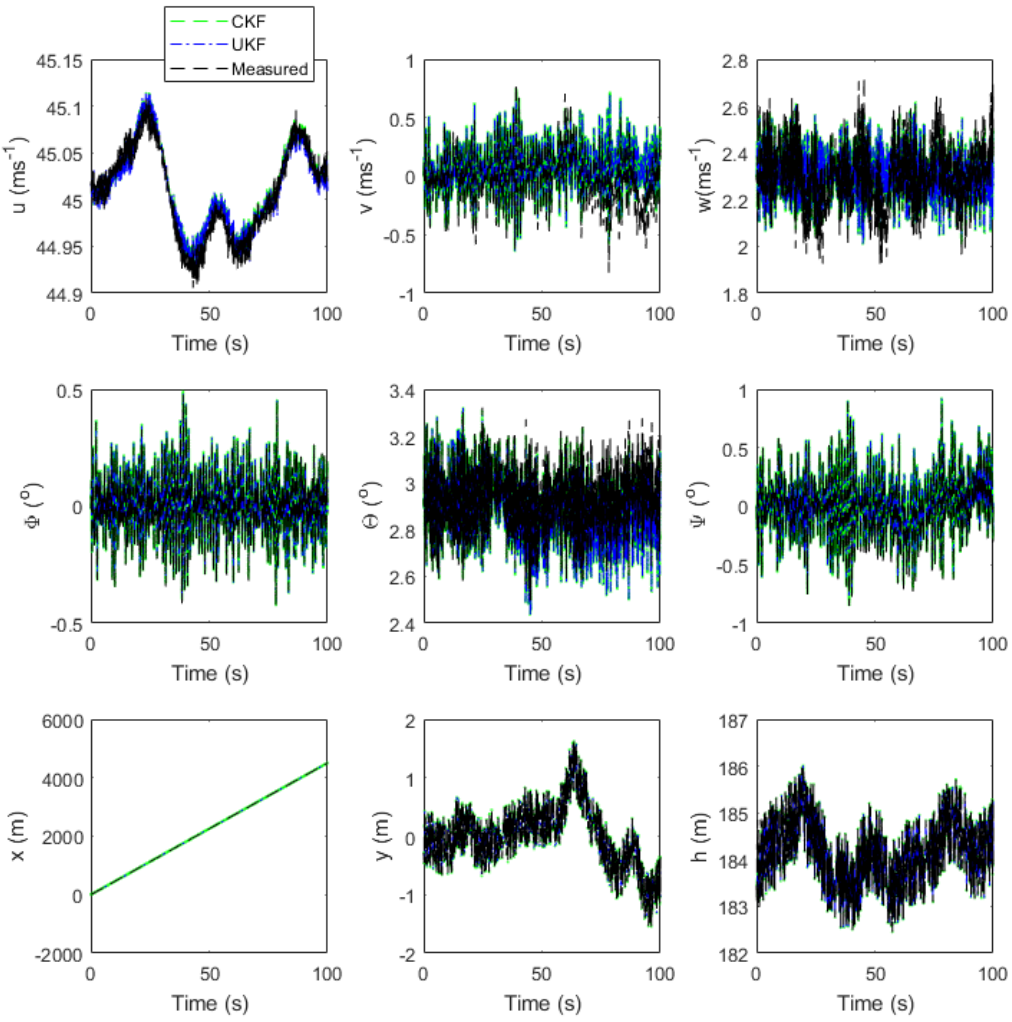

Figure 25: FPR results for GTM T2 UAV with wind disturbance and a 5% sensor error.

The two filters adequately reconstructed the flight parameters, however significant variations are observed in the reconstructed states. The UKF and CKF transmitted the sensor noise observed in the measured data to the estimated states, this has been observed by other researchers [73, 74, 75]. Zarchan and Musoff [75] showed that higher-order filters, like the CKF and UKF provide improved estimates, however, they are prone to noise transmission. Furthermore, the addition of process noise, w, to Kalman filter algorithms results in noisier estimates. The use of process noise in the filtering framework can not be entirely eliminated because process noise accounts for unmodelled imperfections in the kinematic equations used in filtering. Including process noise in filtering algorithms improves estimating capabilities and eliminates the drifting of residual errors from zero and filter lag [75]. As such, though process noise results in noisier estimates it improves the overall quality of the estimate [75].

In order to quantify the overall performance of the two filters their individual ARMSEs are calculated for the different sensor error budgets. Figure 26 shows the ARMSEs values for fifty and one hundred independent Monte Carlo runs with random noise functions w and v, and 0%, 2%, 5% and 10% sensor errors. The measurement resolutions used to obtain 0%, 2%, 5% and 10% error are discussed in Section 3.4.

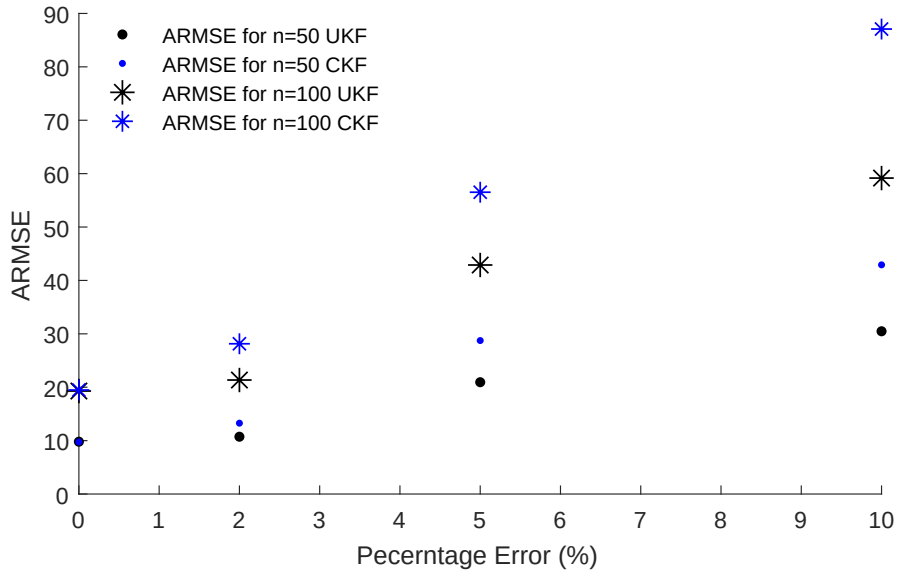

Figure 26: ARMSE for different n number of independent Monte Carlo runs with random noise functions, w and v at 0%, 2%, 5% and 10% sensor error budgets.

The two Kalman filters successfully reconstruct the sensor readings regardless of the noise level imposed. The difference in ARMSEs of the CKF and UKF is not significant for a 0% sensor error however, as the percentage sensor error increases the ARMSE of the CKF becomes much larger than that of the UKF. The UKF provides better estimations at excessive noise levels, this is consistent with the study carried out by Teixeira et al., [43]. These results show that the performance of the CKF is sensitive to large measurement error.

Table 11 shows the UKF and CKF ARMSEs values calculated for fifty and one hundred Monte Carlo runs. The ARMSE values for fifty Monte Carlo runs are about half of the corresponding one hundred Monte Carlo run for all percentage errors. Given that the ARMSEs values over fifty Monte Carlo runs can be scaled by a factor of two to get ARMSE values for one hundred independent runs indicates consistency in the performance of the filters. It also shows that same conclusions can be drawn when one analyses either fifty or one hundred Monte Carlo runs. It follows that for further analysis the use of fifty Monte Carlo runs is sufficient.

Table 11: ARMSEs for n=50 and n=100 independent Monte Carlo runs for the GTM T2 UAV experiencing 0%, 2%, 5% and 10% sensor errors.

Sensor error budget	0%	2%	5%	10%
ARMSE UKF (n=50)	9.80	10.73	20.94	30.48
ARMSE CKF (n=50)	9.75	13.27	28.74	42.92
ARMSE UKF (n=100)	19.29	21.73	42.89	59.17
ARMSE CKF (n=100)	19.48	28.14	56.52	87.08

The time history of the root mean square error (RMSE) of each of the state variables is calculated and plotted in Figure 27 for a 5% sensor error budget.

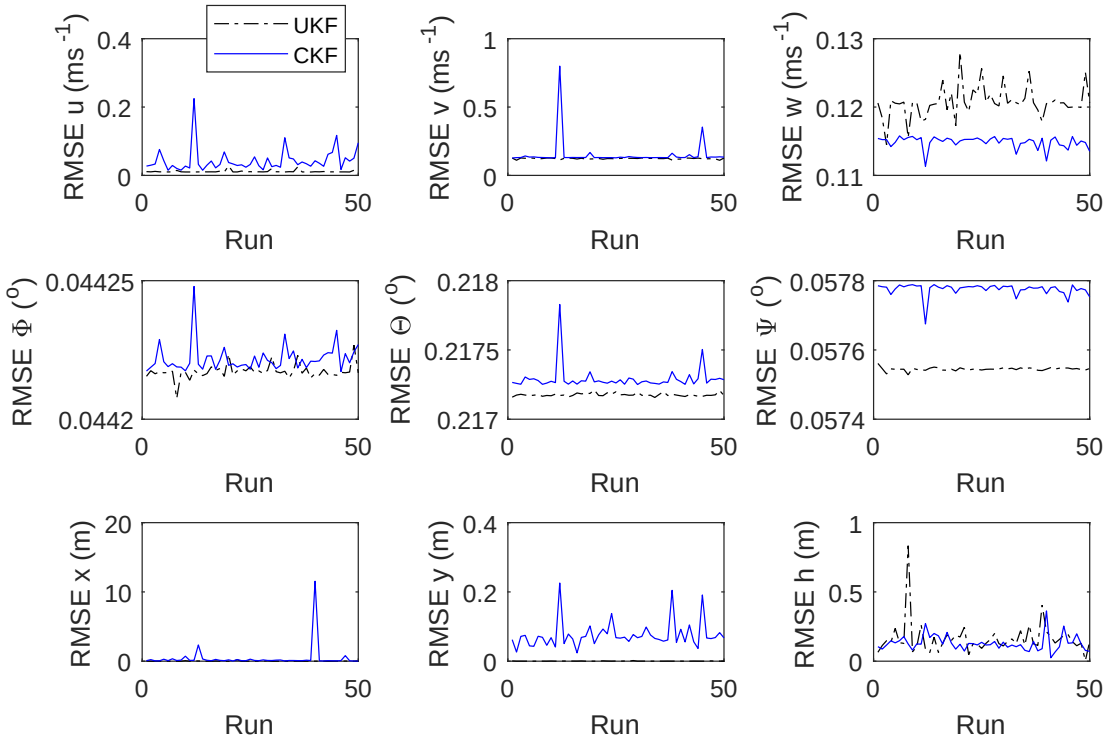

Figure 27: The RMSE values for fifty Monte Carlo runs with random noise functions w and v, and 5% sensor error budget.

Wilcoxon two-sample rank-sum hypothesis testing is performed at 5% level of significance to compare the performance of the CKF and UKF. Results from the hypothesis tests are presented in Table 12. Hypothesis testing at 5% level of significance, show that the overall performance of the UKF is significantly superior to that of the CKF for excessive sensor noise. The CKF only outperforms the UKF in reconstructing the w state. The combination of ARMSE, RMSE data and hypothesis test results indicate that the UKF exhibits superior performance to the CKF. The UKF utilises statistical linearisation to capture the true mean and covariance through the use of sigma-points that are propagated on the unscented transform. This captures the true posterior distribution. On the other hand, the CKF follows the Bayer filter theory that is strongly dependent on the assumption that the noise and measurement probability densities follow a normal distribution. This was not the case for the sensor error and noise probability densities imposed on the GTM T2 UAV model, this may be the reason behind the degraded performance of the CKF at excessive sensor noise. Yang et al., [76] showed that the CKF provides satisfactory results in Gaussian systems, however performance is degraded for non-Gaussian systems.

Table 12: Hypothesis tests comparing UKF and CKF performance over fifty Monte Carlo runs for 5% sensor noise.

$H_\circ$: $\bar{x}_{CKF} = \bar{x}_{UKF}$

H_1: $\bar{x}_{CKF} < \bar{x}_{UKF}$ and $\bar{x}_{CKF} > \bar{x}_{UKF}$ for w state only

Level of significance: 5%, $\alpha = 0.05$

Z-score = 1.645, reject $H_\circ$ if Test score > Z-score, otherwise accept $H_\circ$

State	$\Sigma RMSE_{CKF}$	$\Sigma RMSE_{UKF}$	Test score	Decision
u $(m.s^{-1})$	2.88	0.54	8.39	Reject H_o, $\bar{x}_{uCKF} > \bar{x}_{uUKF}$
v $(m.s^{-1})$	7.07	6.15	8.5794	Reject H_o, $\bar{x}_{vCKF} > \bar{x}_{vUKF}$
w $(m.s^{-1})$	5.73	6.07	-8.2347	Reject H_o, $\bar{x}_{wCKF} < \bar{x}_{wUKF}$
ϕ $(^\circ)$	2.22	2.21	6.6008	Reject H_o, $\bar{x}_{\phi CKF} > \bar{x}_{\phi UKF}$
θ $(^\circ)$	10.84	10.85	8.6138	Reject H_o, $\bar{x}_{\theta CKF} > \bar{x}_{\theta UKF}$
ψ $(^\circ)$	2.89	2.87	8.2691	Reject H_o, $\bar{x}_{\psi CKF} > \bar{x}_{\psi UKF}$
x (m)	9.58	0.50	7.9727	Reject H_o, $\bar{x}_{xCKF} > \bar{x}u_{xUKF}$
y (m)	3.69	0.015	8.6138	Reject H_o, $\bar{x}_{yCKF} > \bar{x}_{yUKF}$
z (m)	6.69	7.50	0.5136	Accept H_o, $\bar{x}_{zCKF} = \bar{x}_{zUKF}$

Additionally, the CKF uses cubature numerical integration to capture the posterior distribution [44]. The deterministic approach requires that the initial value of the covariance be accurately chosen, incorrect initial conditions result in an accumulation of error in the estimated state [44, 77]. The error accumulates, especially for errors associated with accelerometer measurements that are integrated twice to give position [77]. The developer of the CKF, Arasaratnam [42] noted that the CKF is susceptible to errors in the covariance matrix. He identified the following numerical operations in the CKF algorithm, presented in Section 4.4, that compound the error:

- Matrix square rooting in Equation (4.31).
- Matrix inversion in Equations (4.38) and (4.44).
- Matrix squaring which amplifies errors in Equations (4.38) and (4.44).
- Subtraction of two matrices that have a covariance error Equations (4.37), (4.42) and (4.43).

The CKF degraded performance under excessive error observed in Figure 26 is not unique to the UAV parameter identification application. Matzuka et al., [44] used the UKF and CKF to reconstruct the states in an autoregulation model. This model describes cerebral blood flow; it involves high non-linearities, error and oscillatory inputs. The UKF managed to estimate a majority of states; however, the CKF failed to estimate any of the parameters due to the large numerical errors. Matzuka et al., [44] confirmed that this degraded performance is due to the covariance estimation step of filtering. They stated that errors accumulate, causing divergence in the state estimate. This is more prominent for the CKF because of its sensitivity to error [44]. Teixeira et al., [43] showed that the UKF filter provided adequate state and parameter estimation results for exercises with large initialisation errors, hence providing superior results to the CKF.

6.1.2 Sensor bias

Sensor bias occurs when there is an average displacement from the true sensor measurement. A $0.01^o s^{-1}$ sensor bias is applied to the trimmed value of the measured pitch rate, q. This pitch rate sensor bias is shown in Figure 28. The $0.01^o s^{-1}$ sensor bias was applied to the measurement pitch rate to simulate sensor bias; the results obtained from the flight path reconstruction exercise are shown in Figure 29.

The two filters successfully track all the states except for the pitch angle θ and vertical velocity component w. There is a progressive drift in the estimation of the two states. The

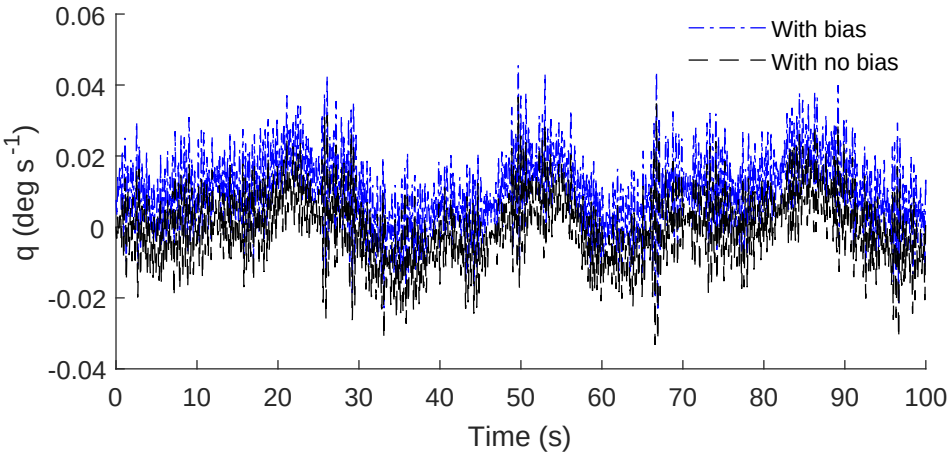

Figure 28: Measured pitch rate with and without $0.01^o s^{-1}$ sensor bias.

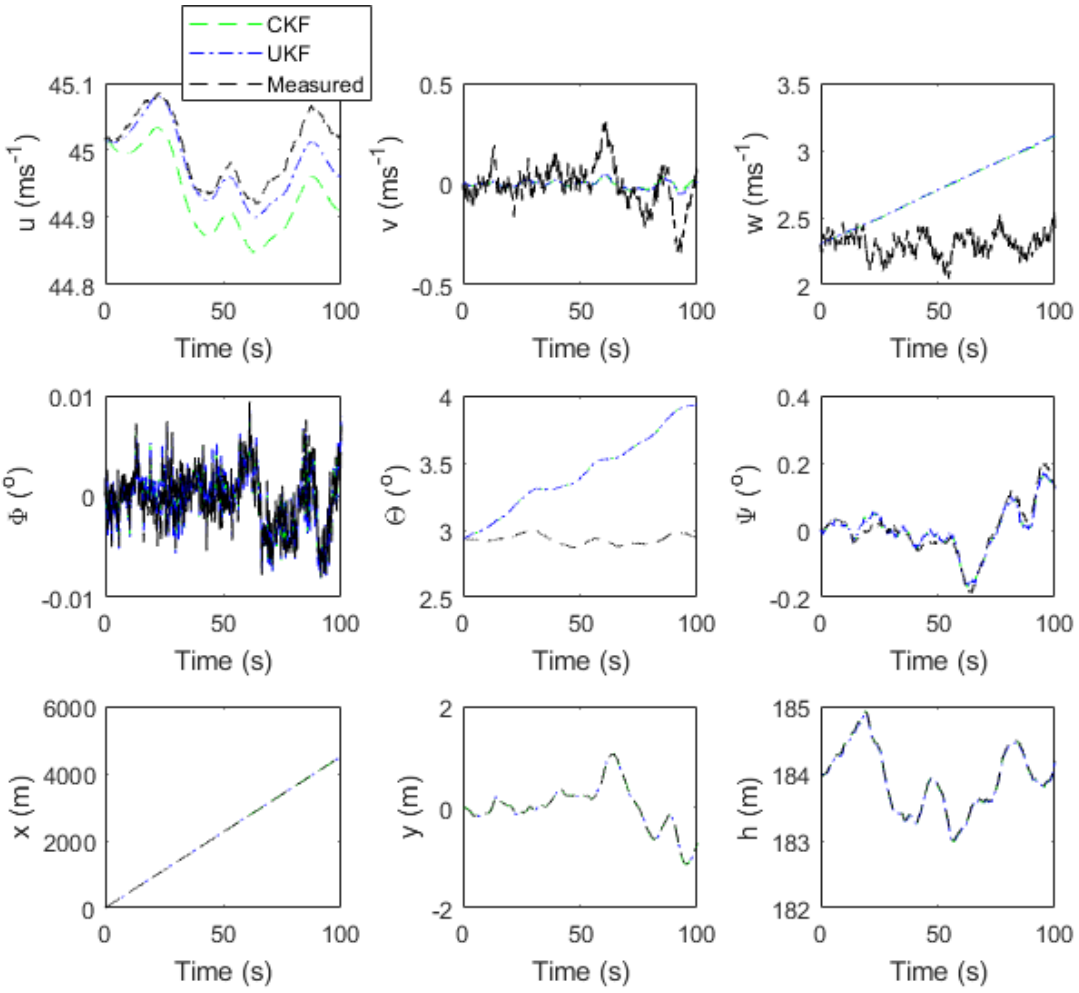

Figure 29: Flight path reconstruction results for a GTM experiencing a $0.01^o s^{-1}$ sensor bias in the pitch rate measurement.

noted drift in the pitch angle, θ and the vertical velocity component, w is caused by the bias in the sensor measurement of the pitch rate, q. This adversely impacts the reconstruction

of the two states. This is consistent with results obtained by Klein and Morelli [62] who performed flight path reconstruction under sensor bias. The researchers showed that a bias in the vertical acceleration measurement caused a drift in the velocity component, w state and degraded the estimated velocity state.

The root mean square errors (RMSE) for each state variable are calculated over fifty independent Monte Carlo runs with random process and measurement errors, w and v. The RMSE values observed are shown in Figure 30. In addition to the RMSE values, the accumulated root mean square errors (ARMSE) of the UKF and CKF are used to compare the performance of the two filters. The ARMSE is calculated over fifty and one hundred independent Monte Carlo runs and the results are given in Table 13.

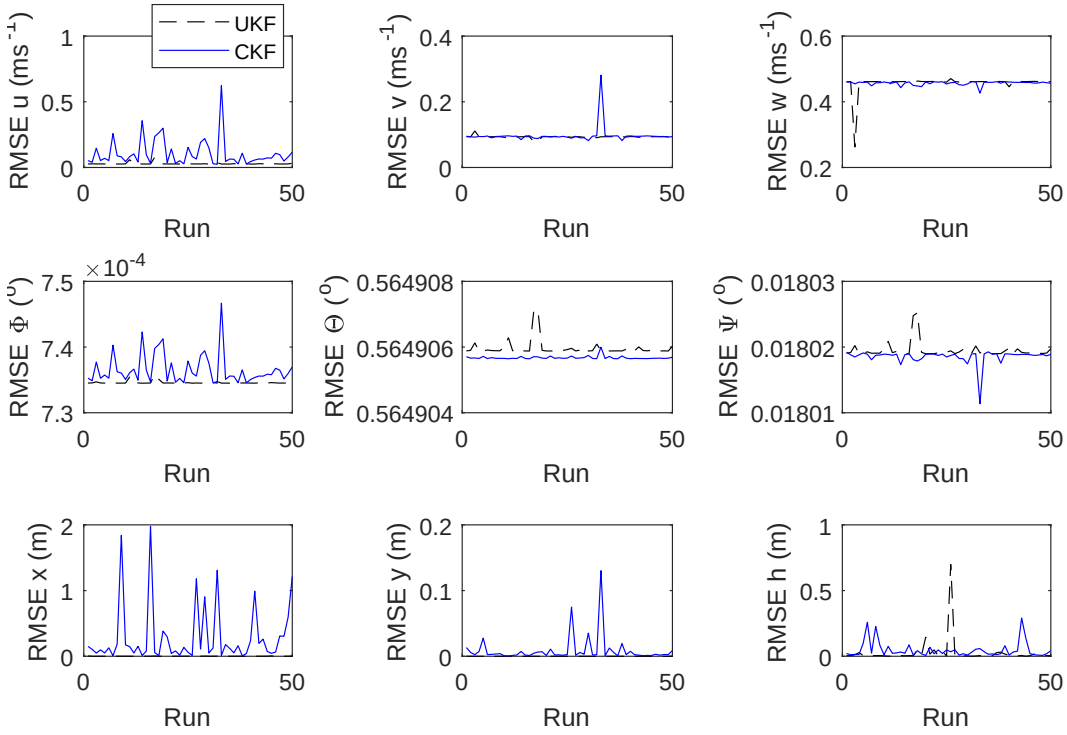

Figure 30: The RMSE for fifty Monte Carlo runs with random noise functions w and v, and a $0.01^o s^{-1}$ pitch rate bias.

Table 13: ARMSEs for n=50 and n=100 independent Monte Carlo runs for a GTM UAV with sensor bias.

Sensor bias mean value = $0.01 degs^{-1}$	
ARMSE UKF (n=50)	31.03
ARMSE CKF (n=50)	50.75
ARMSE UKF (n=100)	60.56
ARMSE CKF (n=100)	108.50

Both the RMSE and ARMSE values show that the overall performance of the UKF is better than that of the CKF. In order to quantify the performance of the filters in reconstructing the individual states, hypothesis testing is used to determine if there is a notable difference between the UKF and CKF at 5% level of significance. Table 14 shows the results obtained from the hypothesis testing.

Table 14: Hypothesis tests comparing UKF and CKF performance over fifty Monte Carlo runs for sensor bias.

$H_\circ$: $\bar{x}_{CKF} = \bar{x}_{UKF}$

H_1: $\bar{x}_{CKF} > \bar{x}_{UKF}$ and $\bar{x}_{UKF} > \bar{x}_{CKF}$ for w state only

Level of significance: 5%, $\alpha = 0.05$

Z-score = 1.645, reject $H_\circ$ if Test score > Z-score, otherwise accept $H_\circ$

State	$\Sigma RMSE_{CKF}$	$\Sigma RMSE_{UKF}$	Test score	Decision
u $(m.s^{-1})$	8.78	1.38	7.3523	Reject H_o, $\bar{x}_{uCKF} > \bar{x}_{uUKF}$
v $(m.s^{-1})$	4.63	4.06	3.5813	Reject H_o, $\bar{x}_{vCKF} > \bar{x}_{vUKF}$
w $(m.s^{-1})$	22.64	23.08	-6.6905	Reject H_o, $\bar{x}_{wCKF} < \bar{x}_{wUKF}$
ϕ $(^\circ)$	0.0369	0.0367	7.6487	Reject H_o, $\bar{x}_{\phi CKF} > \bar{x}_{\phi UKF}$
θ $(^\circ)$	28.24	28.24	8.6207	Reject H_o, $\bar{x}_{\theta CKF} > \bar{x}_{\theta UKF}$
ψ $(^\circ)$	0.901	0.900	8.4966	Reject H_o, $\bar{x}_{\psi CKF} > \bar{x}_{\psi UKF}$
x (m)	11.89	0.056	8.6138	Reject H_o, $\bar{x}_{xCKF} > \bar{x}_{xUKF}$
y (m)	0.90	$2.53\times10^{-}4$	8.6138	Reject H_o, $\bar{x}_{yCKF} > \bar{x}_{yUKF}$
z (m)	1.84	1.30	6.8421	Reject H_o, $\bar{x}_{zCKF} > \bar{x}_{zUKF}$

The hypothesis testing confirms that at a 5% level of significance, UKF consistently performed better than the CKF in reconstructing all states, except the vertical velocity w. Numerous high picks in the x and y RMSE graphs show that at certain w and v noise levels, the CKF exhibits degraded performance in reconstructing the x and y states. Results from the hypothesis test concur, the UKF performance in reconstructing these states is superior to that of the CKF. All these factors indicate that the CKF is vulnerable to noise levels. Though there is no significant difference in most of the reconstructed states, the UKF has a lower ARMSE value than that of the CKF. This shows that overall the UKF performance under sensor bias is better than that of the CKF. Teixeira et al., [43] used the UKF and concluded that the filter provided adequate state and parameter estimation results for exercises with large initialisation errors. All in all, the UKF exhibits marginally better performance when compared to the CKF and is more robust in the presence of poor state initial conditions.

6.1.3 Sensor blackout

Sensor outages occur when a sensor stops recording data, this typically happens to GPS sensors. GPS signal disruption may occur for a UAV flying between buildings, terrain or in thick vegetation. The sensor blackout is modelled as a $50s$ long GPS outage of the position and velocity states x, y, h and V. The blackout region is between $t = 40s$ and $t = 90s$. The reconstructed states of the GTM are shown in Figure 31.

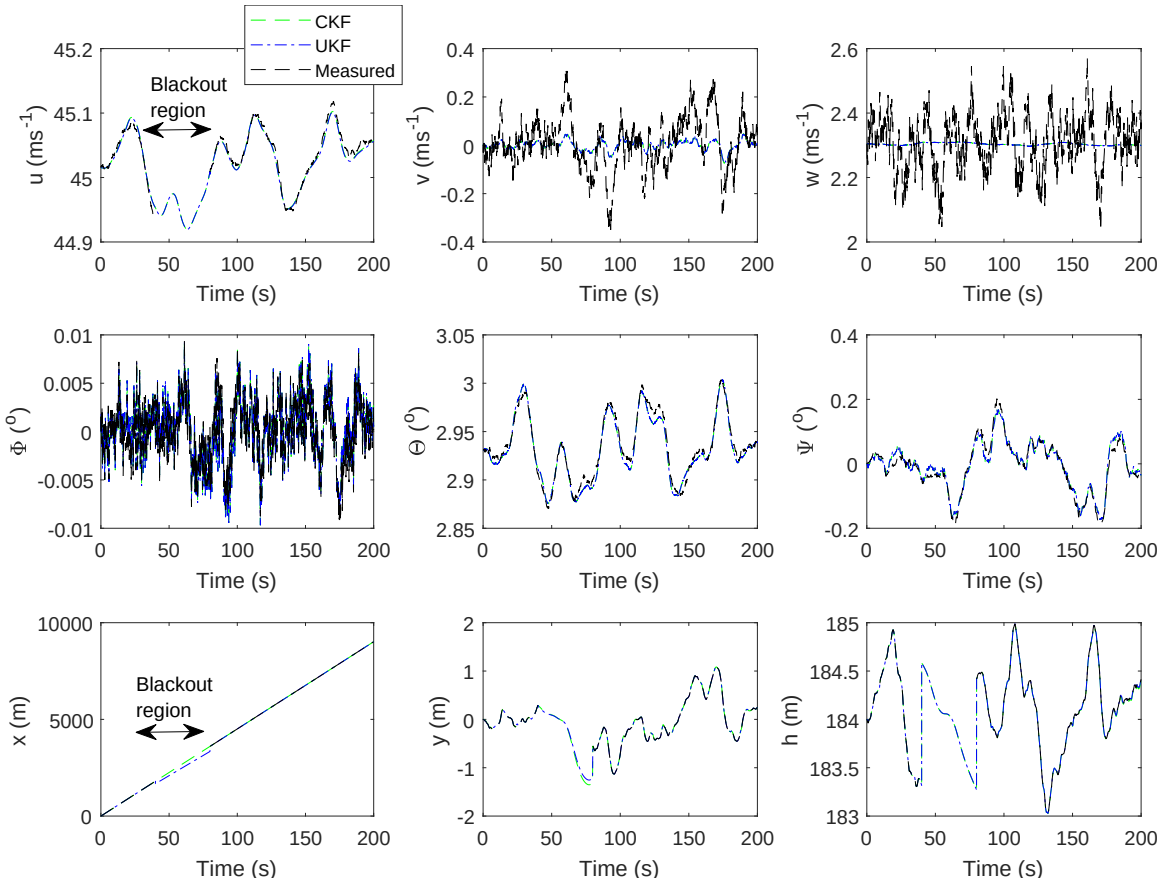

Figure 31: FPR for an aircraft experiencing a GPS outage between $t = 40s$ and $t = 90s$.

The flight path reconstruction results show that both the CKF and UKF continue to track the states during periods of GPS sensor blackout, however there is an offset noted for the x state. The reconstructed results of the x state are shown in Figure 32.

The state RMSE values obtained from the UKF and CKF are shown in Figure 33 and the results gathered from a comparison of the RMSE mean values through hypothesis testing are presented in Table 15.

Reconstruction results concur with the RMSE values and hypothesis test results for the x state obtained; the highest RMSE is recorded on the state position, x as seen in Figure 33. RMSE results show that the performance of the UKF is consistently inferior to that of the

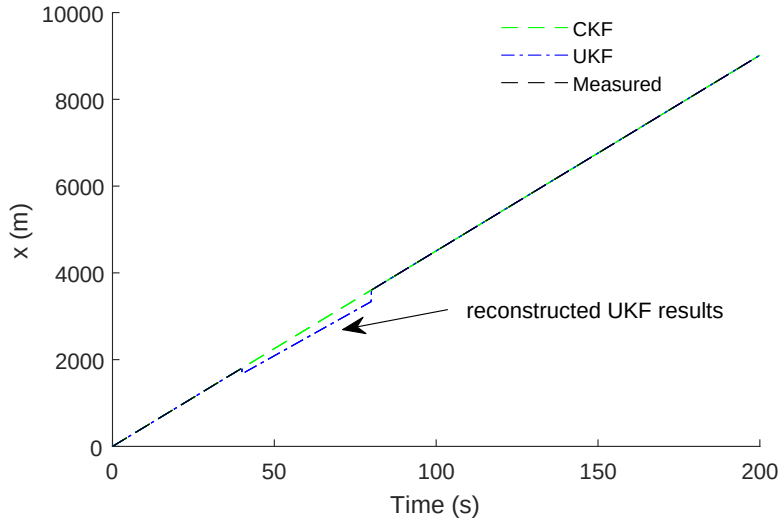

Figure 32: The reconstructed results for the x state.

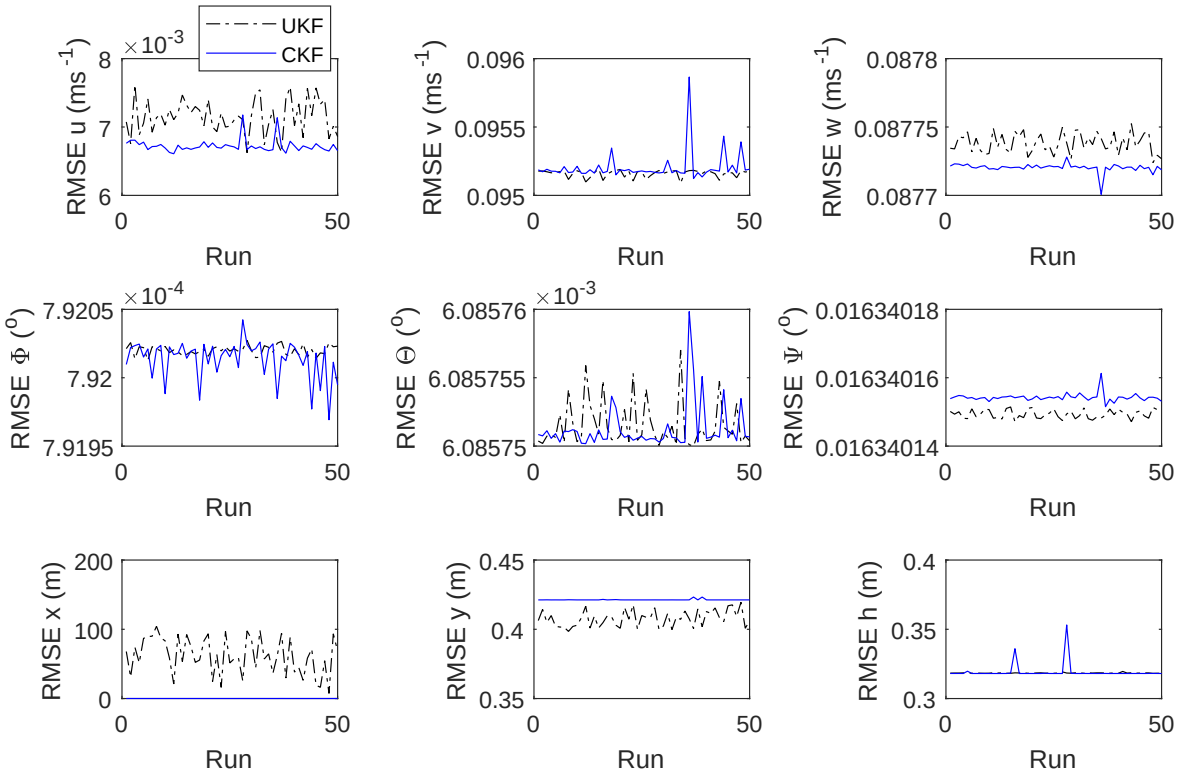

Figure 33: The state RMSE values for the GTM T2 UAV experiencing sensor blackout.

CKF when reconstructing the x position state. High RMSE picks and hypothesis testing also reveal that under certain process and measurement noise variations the UKF exhibits degraded performance in reconstructing the w state. The CKF outperforms the UKF when tracking the x states during a sensor outage. During the GPS sensor blackout there are four fewer known states in the observation matrix. An increase in the number of unknown states reduces the ability for UKF to reconstruct states [78]; a result of this is a gradual divergence from the true state as the blackout time increases [19, 78, 79]. This is visible in

Table 15: Hypothesis tests comparing UKF and CKF performance over fifty Monte Carlo runs for sensor blackout.

$H_\circ$: $\bar{x}_{CKF} = \bar{x}_{UKF}$

H_1: $\bar{x}_{CKF} > \bar{x}_{UKF}$ and $\bar{x}_{UKF} > \bar{x}_{CKF}$ for u, w, ϕ, x and z states

Level of significance: 5%, $\alpha = 0.05$

Z-score = 1.645, reject $H_\circ$ if Test score > Z-score, otherwise accept $H_\circ$

State	$\Sigma RMSE_{CKF}$	$\Sigma RMSE_{UKF}$	Test score	Decision
u $(m.s^{-1})$	0.33	0.35	-2.85	Reject H_o, $\bar{x}_{uCKF} < \bar{x}_{uUKF}$
v $(m.s^{-1})$	4.76	4.76	1.37	Accept H_o, $\bar{x}_{vCKF} = \bar{x}_{vUKF}$
w $(m.s^{-1})$	4.386	4.387	-7.08	Reject H_o, $\bar{x}_{wCKF} < \bar{x}_{wUKF}$
ϕ $(^\circ)$	0.0396	0.0396	-4.58	Reject H_o, $\bar{x}_{\phi CKF} < \bar{x}_{\phi UKF}$
θ $(^\circ)$	0.3043	0.3043	1.35	Accept H_o, $\bar{x}_{\theta CKF} = \bar{x}_{\theta UKF}$
ψ $(^\circ)$	0.817	0.817	3.95	Reject H_o, $\bar{x}_{\psi CKF} > \bar{x}_{\psi UKF}$
x (m)	3.78	3.11×10^3	-8.62	Reject H_o, $\bar{x}_{xCKF} < \bar{x}_{xUKF}$
y (m)	21.06	20.38	8.61	Reject H_o, $\bar{x}_{yCKF} > \bar{x}_{yUKF}$
z (m)	15.93	15.91	-2.65	Accept H_o, $\bar{x}_{zCKF} < \bar{x}_{zUKF}$

the reconstruction of the position x shown in Figure 32, the reconstructed position gradually deviates from the true state as the blackout time increases.

Similar results are obtained by Zhang et al., [80]. Optimal performance of the UKF is achieved when the observation matrix is of full rank, missing states from the observation matrix degrade UKF performance [19]. The initial conditions are accurate, as a result the CKF continues to accurately track the state during the sensor blackout. CKF exhibits filter stability when there are missing states. Fifty and one hundred Monte Carlo runs with random noise functions are used to calculate the ARMSE. The ARMSE values obtained are given in Table 16; these values affirm that the CKF outperforms the UKF for sensor blackout.

Table 16: ARMSEs for n=50 and n=100 independent Monte Carlo runs for a GTM UAV experiencing GPS sensor blackout

Sensor blackout: $V, x, y, h = 0$	
ARMSE UKF (n=50)	2892
ARMSE CKF (n=50)	50.40
ARMSE UKF (n=100)	5694
ARMSE CKF (n=100)	102.58

6.2 Induced Control Surface Failure

In this section, fifty Monte Carol runs in conjunction with the ARMSE and RMSE, are used to measure the performance of the CKF and UKF when reconstructing states in the presence of control surface failure. The mean and standard deviation RMSE values of the UKF and CKF are used to compare the performance of the two filters. It should be noted that the PID controller was active during all disturbances, resulting in corrective response to the upsets.

6.2.1 Jammed control surface

A positive step surface deflection of 10° is applied to the elevator, rudder and aileron control inputs at t=20s. The time response and the reconstructed position obtained for a 10° jammed rudder control input are shown in Figures 34 and 35 respectively.

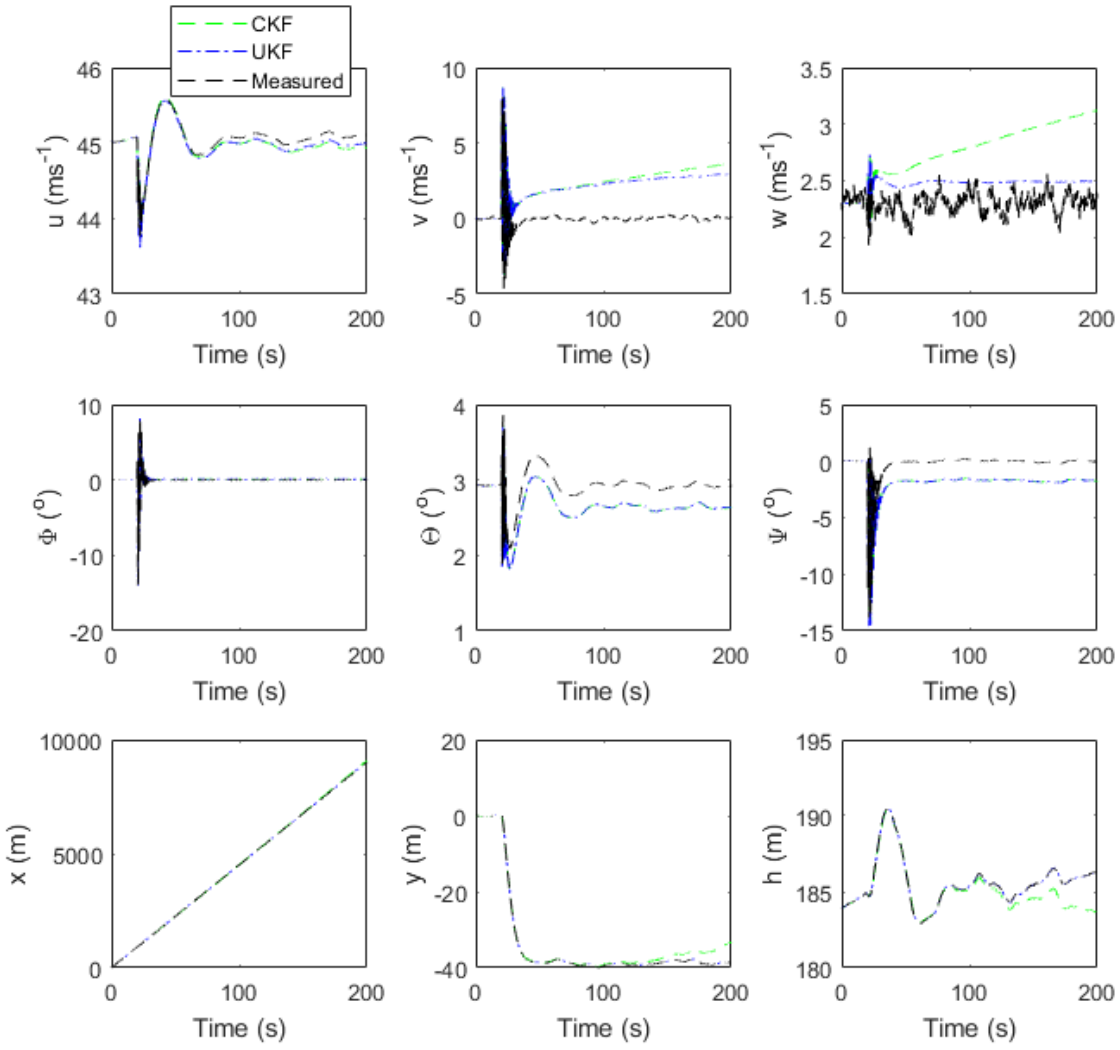

Figure 34: FPR results for a UAV experiencing a $\delta_r = 10^o$ rudder deflection at time t= 20s

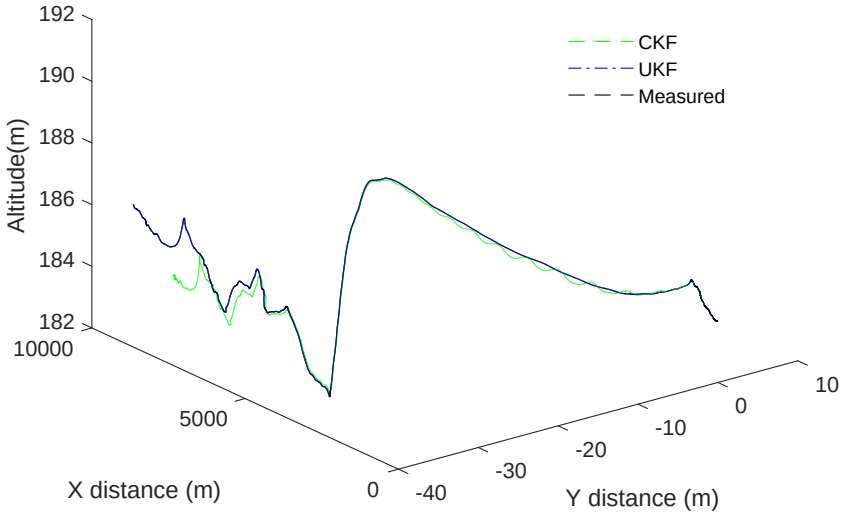

Figure 35: Reconstruction of the position of a UAV experiencing a $\delta_r = 10^o$ rudder deflection.

The adverse sideslip position, abnormal roll and yaw angle perturbation indicate strongly non-linear motion. The flight path reconstruction results show that both the CKF and UKF continue to track the states after LOC is induced, however there is an offset noted for the pitch and yaw angles, θ and ψ, and a gradual deviation in the velocity components, v and w. Additionally, the height state estimate reconstructed by the CKF gradually diverges. The mean and standard deviation values of the ranked state RMSE values presented in Figure 36, are used to compare the performance of the CFK and UKF at 5% level of significance through hypothesis testing. Results from this test are presented in Table 17.

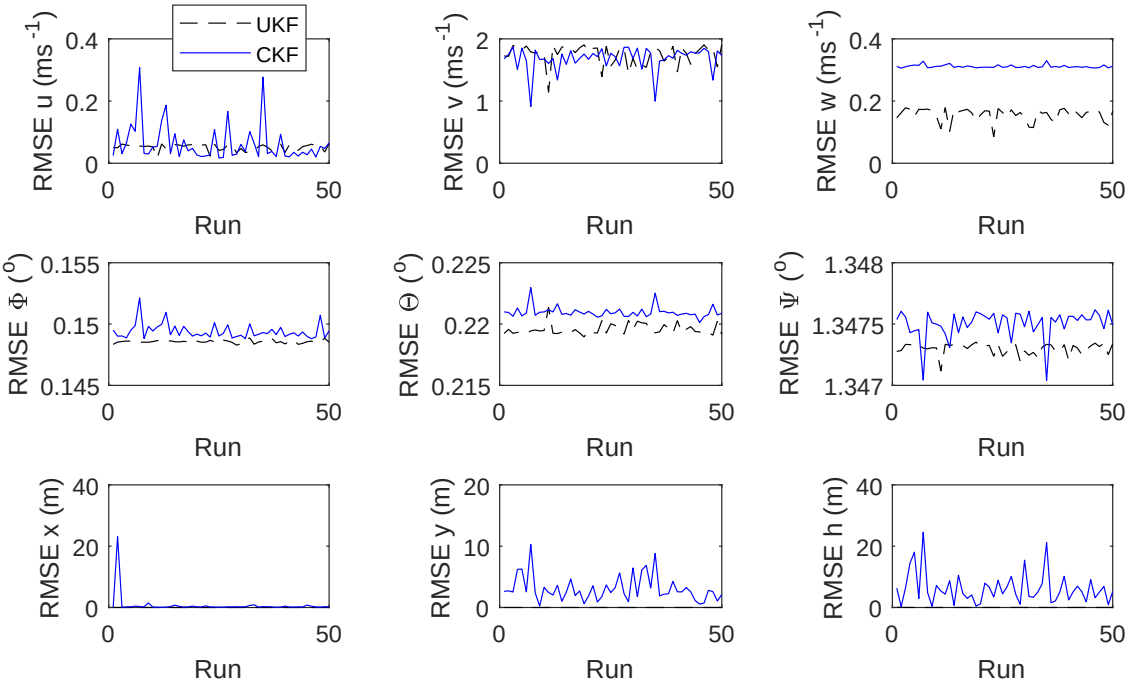

Figure 36: RMSE values for the GTM T2 UAV experiencing a a $\delta_r = 10^o$ rudder deflection.

Table 17: Hypothesis tests comparing UKF and CKF performance over fifty Monte Carlo runs for a jammed rudder deflection of 10%.

$H_\circ$: $\bar{x}_{CKF} = \bar{x}_{UKF}$

H_1: $\bar{x}_{CKF} > \bar{x}_{UKF}$

Level of significance: 5%, $\alpha = 0.05$

Z-score = 1.645, reject $H_\circ$ if Test score > Z-score, otherwise accept $H_\circ$

State	$\Sigma RMSE_{CKF}$	$\Sigma RMSE_{UKF}$	Test score	Decision
u $(m.s^{-1})$	5.38	1.48	1.61	Accept H_o, $\bar{x}_{uCKF} = \bar{x}_{uUKF}$
v $(m.s^{-1})$	4.85	4.65	2.59	Accept H_o, $\bar{x}_{vCKF} > \bar{x}_{vUKF}$
w $(m.s^{-1})$	22.83	22.84	8.6138	Reject H_o, $\bar{x}_{wCKF} > \bar{x}_{wUKF}$
ϕ $(^\circ)$	0.0368	0.0367	7.9038	Reject H_o, $\bar{x}_{\phi CKF} > \bar{x}_{\phi UKF}$
θ $(^\circ)$	28.24	28.24	7.2351	Reject H_o, $\bar{x}_{\theta CKF} > \bar{x}_{\theta UKF}$
ψ $(^\circ)$	0.901	0.901	5.9666	Reject H_o, $\bar{x}_{\psi CKF} > \bar{x}_{\psi UKF}$
x (m)	15.06	0.05	8.6138	Reject H_o, $\bar{x}_{xCKF} > \bar{x}_{xUKF}$
y (m)	0.45	1.44×10^{-4}	8.6138	Reject H_o, $\bar{x}_{yCKF} > \bar{x}_{yUKF}$
z (m)	2.36	1.27	8.6207	Reject H_o, $\bar{x}_{zCKF} > \bar{x}_{zUKF}$

Hypothesis testing shows that there is little difference in the performance of the CKF and UKF in reconstructing the velocity states u only. It also indicates that the gradual deviation observed in the w and h states significantly deteriorates the CKF results. These results imply that the UKF outperforms the UKF at 5% level of significance. In addition to the RMSE and hypothesis testing, the ARMSE obtained from the UKF and CKF flight path reconstruction exercise of a 10° control input elevator, rudder and aileron deflection are given in Table 18.

Table 18: ARMSEs for fifty Monte Carlo runs for a jammed surface deflection of 10°

Control input	ARMSE	Value
$\delta_e = 10^o$	ARMSE UKF (n=50)	23.81
	ARMSE CKF (n=50)	4320
$\delta_a = 10^o$	ARMSE UKF (n=50)	10.68
	ARMSE CKF (n=50)	13.58
$\delta_r = 10^o$	ARMSE UKF (n=50)	120.76
	ARMSE CKF (n=50)	1305

Results presented in this section show that the CKF has poor performance in strongly non-linear conditions, specifically for jammed elevator and rudder. The CKF ARMSE for a 10° elevator jam is 4320, whereas the ARMSE for the UKF is 23.81 under the same conditions;

this shows superior UKF performance. This is consistent with results obtained by Yang et al., [76]. These researchers concluded that the quality of results obtained by the CKF deteriorates for strongly non-linear systems. Matzuka et al., [44] also applied the UKF and CKF to estimate the HIV model. This model is highly non-linear and has varying orders of error. They determined that UKF accurately tracked the states of the strongly non-linear system and the CKF did not. Matzuka et al., [44] concluded that the CKF is more likely to diverge under non-linear conditions, whilst the UKF successfully tracked the states. This divergence is observed in the vertical velocity state, w, and UAV position, x, y and z, reconstructed in this section.

6.2.2 Control surface hard-over

A maximum positive surface deflection of 20°, 20° and 30° is applied to the elevator, aileron and rudder control inputs respectively. The reconstructed time response for a 20° elevator hardover is shown in Figure 37.

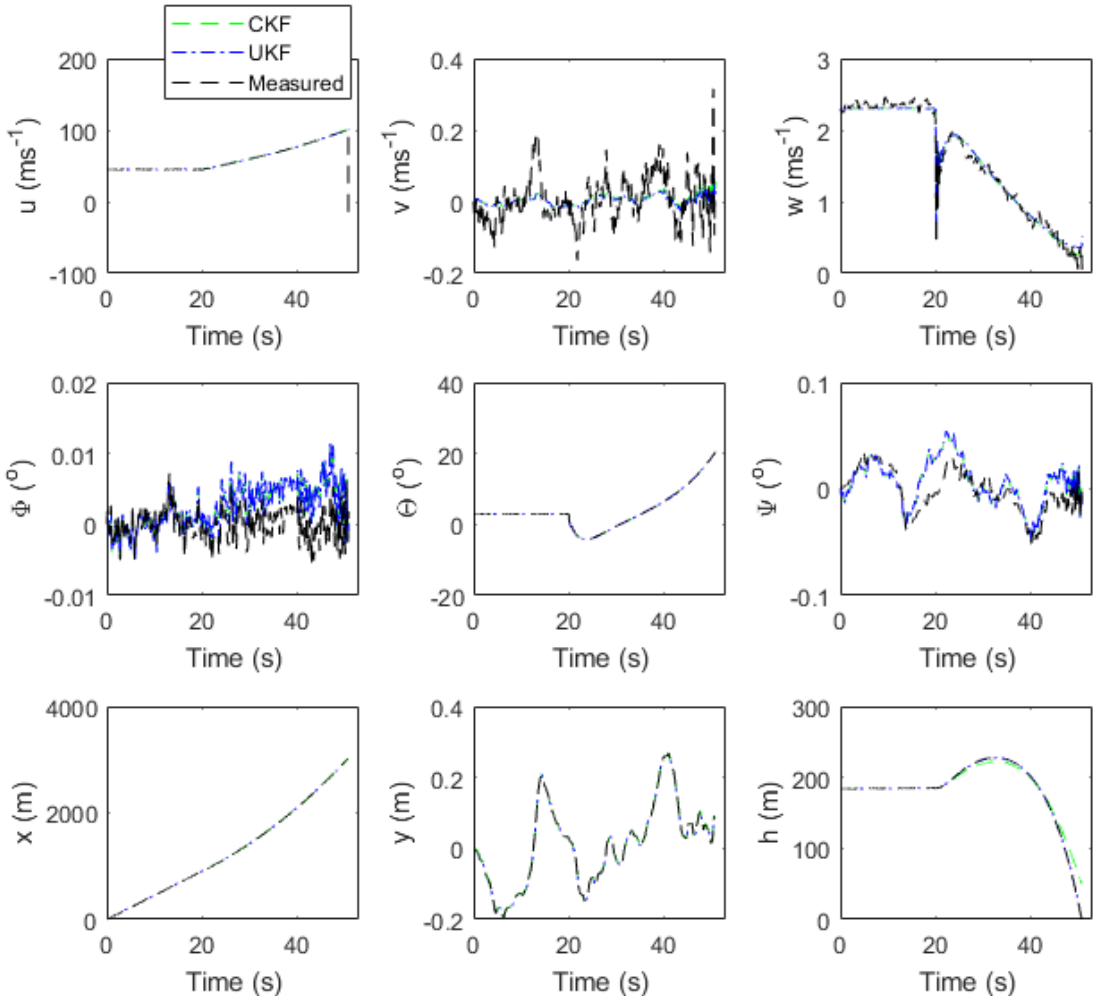

Figure 37: Flight path reconstruction for an aircraft experiencing a 20° elevator hardover.

A similar exercise was performed for the aileron and rudder control inputs. After the positive 20° elevator hardover was applied, the aircraft velocity increased to the maximum velocity, $73ms^{-1}$ and it stalled, while losing altitude and crashed at t=$52s$, as a result the simulation terminated at this point. A similar response is documented in the work done by Padayachee [25]. In this work, he noted that a large elevator command implemented over a long period resulted in aircraft stall in a flight test. RMSE values obtained from fifty Monte Carlo runs for a 20° elevator hardover are presented in Figure 38.

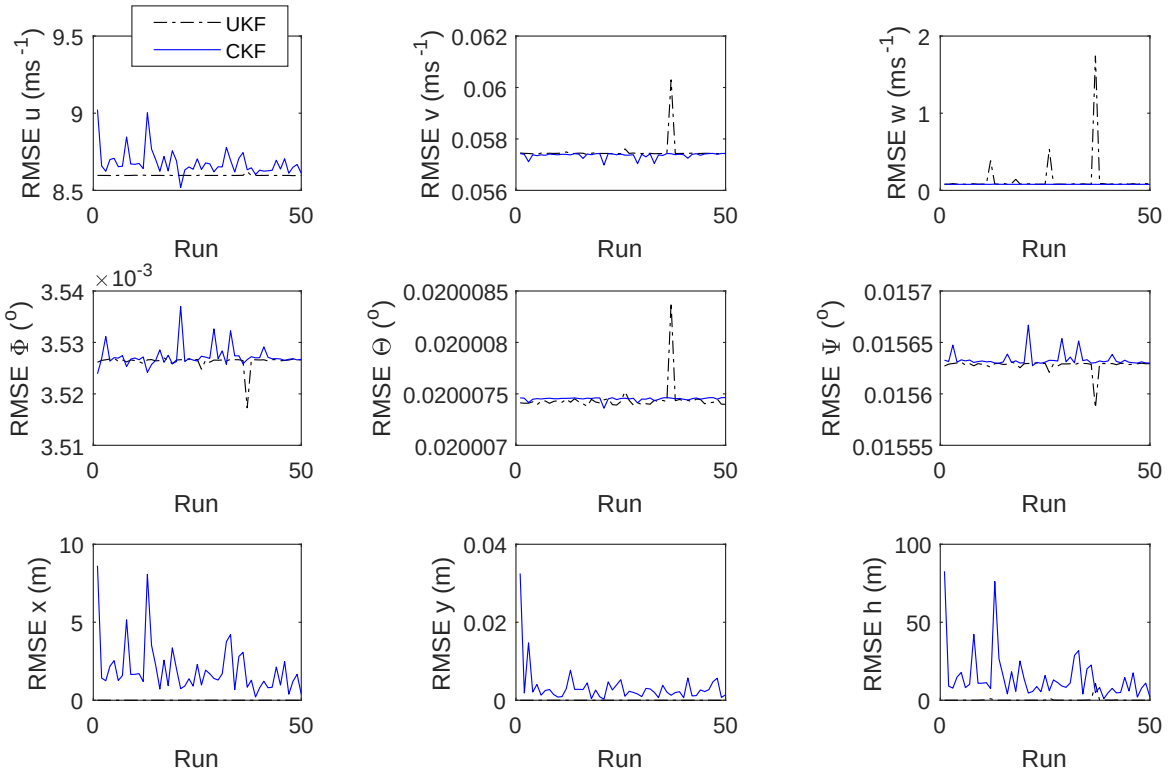

Figure 38: RMSE values for a GTM T2 UAV experiencing 20% elevator hardover.

The results from the flight path reconstruction exercise show that both the CKF and UKF adequately tracked the states, however the quality of the reconstructed results deteriorated slightly closer to stall. This is especially visible for the ϕ and h states. This is consistent with work done by Chauhan and Singh [37], they determined that Kalman filter performance degraded near stall conditions. The means and standard deviation of the ranked RMSE values obtained from fifty independent Monte Carlo runs are used in Wilcoxon two-sample rank-sum hypothesis testing to compare the performance of the UKF and CKF. Results obtained from this testing are presented in Table 19.

The UKF outperformed the CKF in reconstructing all states at a 5% level of significance except w and θ. The difference in UKF and CKF is more significant in predicting the UAV position. For example the sum of the RMSE values in the position state x produced by the CKF is 46.16 whilst the corresponding value of 0.057 for the UKF. This indicates the superior

Table 19: Hypothesis tests comparing UKF and CKF performance over fifty Monte Carlo runs for an elevator hardover of 20%.

$H_\circ$: $\bar{x}_{CKF} = \bar{x}_{UKF}$

H_1: $\bar{x}_{CKF} > \bar{x}_{UKF}$ and $\bar{x}_{UKF} > \bar{x}_{CKF}$ for w and θ states only

Level of significance: 5%, $\alpha = 0.05$

Z-score = 1.645, reject $H_\circ$ if Test score > Z-score, otherwise accept $H_\circ$

State	$\Sigma RMSE_{CKF}$	$\Sigma RMSE_{UKF}$	Test score	Decision
u $(m.s^{-1})$	456	443	2.08	Reject H_o, $\bar{x}_{uCKF} > \bar{x}_{uUKF}$
v $(m.s^{-1})$	67.85	65.32	8.21	Reject H_o, $\bar{x}_{vCKF} > \bar{x}_{vUKF}$
w $(m.s^{-1})$	17.54	24.36	-7.04	Reject H_o, $\bar{x}_{wCKF} < \bar{x}_{wUKF}$
ϕ $(^\circ)$	9.64	9.55	4.68	Reject H_o, $\bar{x}_{\phi CKF} > \mu_{\phi UKF}$
θ $(^\circ)$	2.23	2.36	-5.35	Reject H_o, $\bar{x}_{\theta CKF} < \bar{x}_{\theta UKF}$
ψ $(^\circ)$	14.76	14.50	2.69	Reject H_o, $\bar{x}_{\psi CKF} > \bar{x}_{\psi UKF}$
x (m)	46.16	0.057	8.72	Reject H_o, $\bar{x}_{xCKF} > \bar{x}_{xUKF}$
y (m)	5.77	1.28×10^{-4}	8.61	Reject H_o, $\bar{x}_{yCKF} > \bar{x}_{yUKF}$
z (m)	562	23	8.39	Reject H_o, $\bar{x}_{zCKF} > \bar{x}_{zUKF}$

performance of the UKF in highly unsteady conditions. Chauhan and Singh [37] identified that the UKF provided satisfactory results for high angles of attack and unsteady conditions, similar to stall conditions. The CKF performance degraded close to the point of stall, which is largely non-linear. This is consistent with work done by Matzuka et al., [44], who noted that the quality of CKF performance reduced in non-linear conditions.

The ARMSEs obtained from the UKF and CKF flight path reconstruction exercise of 20°, 20° and 30° elevator, aileron and rudder control inputs respectively are given in Table 20. The simulated motion of the GTM for elevator and rudder hardover is strongly non-linear. The ARMSE values presented follow a similar trend to those obtained for flight path reconstruction associated with jammed control surface in Section 6.2.1. The ARMSE values show that the UKF outperforms the CKF for the state estimations of all control inputs. This may be because the performance of the CKF degrades for strongly non-linear systems.

The ARMSE values for the elevator and rudder hardover are very large, however the ARMSE obtained from the aileron hardover remain relatively small. This is because of the inherent ability of aircraft to maintain wings levels in the presence of an aileron disturbance. When an aileron disturbance is applied, the aircraft begins to roll, however an increase in incidence angle produces a differential in lift. This differential in lift from the wings produces a restoring

Table 20: ARMSEs for n=50 independent Monte Carlo runs for control surface hardover.

Control input	ARMSE	Value
$\delta_e = 20^o$	ARMSE UKF (n=50)	688.32
	ARMSE CKF (n=50)	14487
$\delta_a = 20^o$	ARMSE UKF (n=50)	17.78
	ARMSE CKF (n=50)	27.39
$\delta_r = 30^o$	ARMSE UKF (n=50)	397.78
	ARMSE CKF (n=50)	22133

rolling moment that balances the induced disturbance [81]. As a result the aircraft regains steady state after an aileron disturbance, this motion is not strongly non-linear. This may be the reason why the ARMSE values of aileron disturbance are small for both CKF and UKF state estimations.

6.2.3 Control surface float

A system failure, in either hydraulics or severing or loosening of cables may result in free oscillations of control surfaces, also known as control surface float. This will initially start as a wiggle that will turn into a limit-cycle oscillation [81]. This failure mode is induced in the GTM T2 UAV simulation and the flight path reconstruction results obtained through the CKF and UKF are presented in this section. The control input disturbance applied to the elevator, aileron, and ruder is shown in Figure 39.

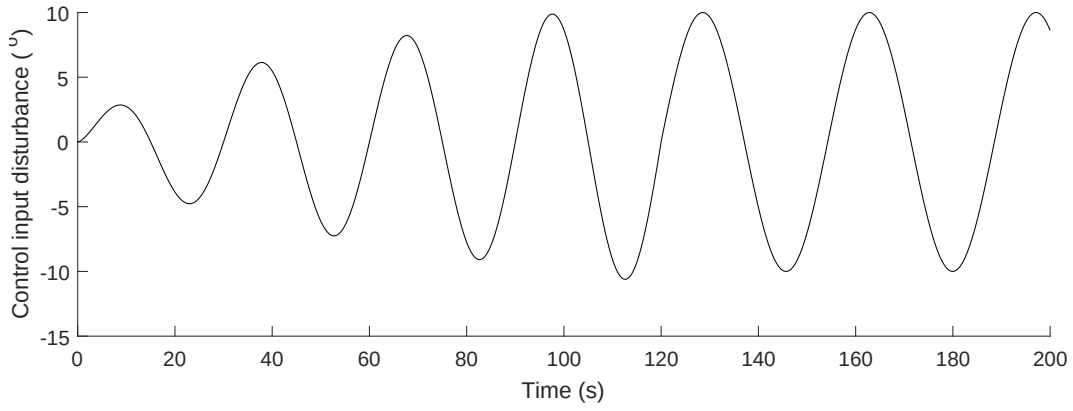

Figure 39: Elevator, aileron, and ruder input disturbance applied in the simulation model.

The control input shown in Figure 39 is applied separately as elevator, aileron and rudder inputs. Only the state time history obtained for rudder float is presented in this section. Though the control disturbance is imposed on the rudder control only, the aileron also shows an upset, this is yaw and roll coupling. Similar results were obtained by Stengel [81], he

applied a sinusoidal float disturbance to the rudder and it excited aileron inputs. The coupled rudder and the induced aileron surface deflection obtained from applying the rudder control input upset is shown in Figure 40, the reconstructed response is presented in Figure 41.

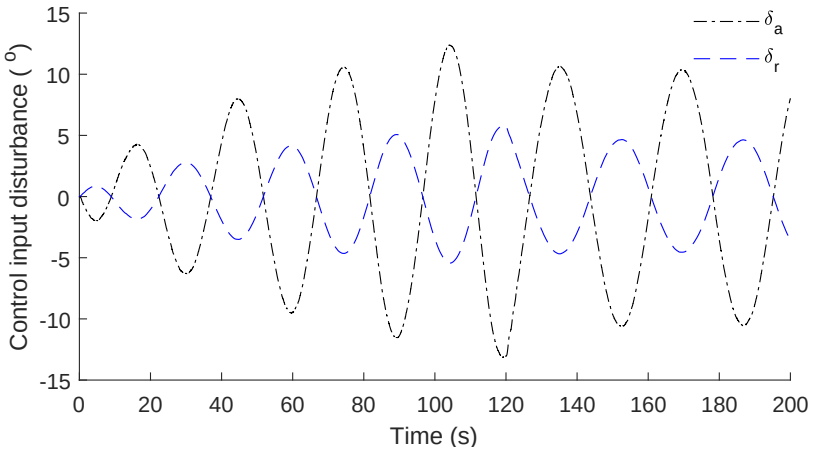

Figure 40: Coupled rudder and aileron surface deflection resulting from a rudder float.

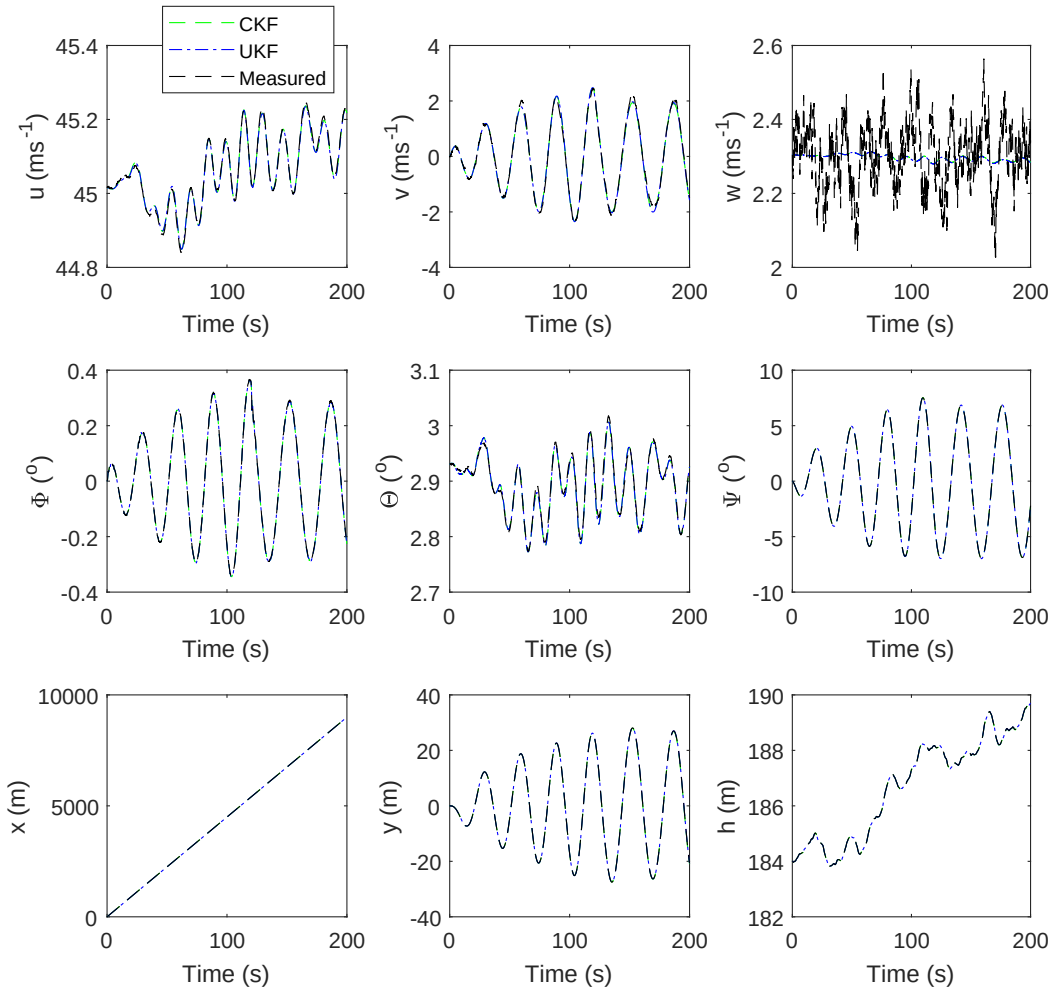

Figure 41: FPR results for a GTM T2 UAV experiencing wind disturbance and a rudder float with a maximum amplitude of 10°.

The control disturbance resulted in oscillatory motion, this is visible in the GTM T2 UAV position plot shown in Figure 42.

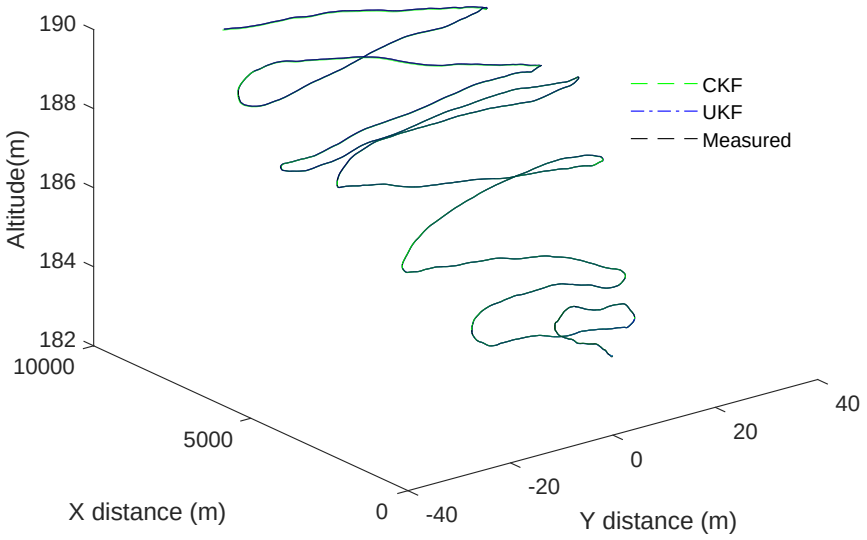

Figure 42: Position of the GTM T2 UAV experiencing wind disturbance and a rudder float with a maximum amplitude of 10°.

Both Kalman filters successfully reconstructed all the states. The ARMSE values obtained from fifty Monte Carlo runs with random v and w noise values are presented in Table 21. The trend of ARMSE values presented in this table resembles that of the other control surface input upsets. The UKF produced better results than the CKF, especially for the reconstruction of the elevator float.

Table 21: ARMSEs for n=50 independent Monte Carlo runs for floating control inputs δ_e, δ_a and δ_r

Control input	ARMSE	Value
Max amplitude $\delta_e = 10^o$	ARMSE UKF (n=50)	20.64
	ARMSE CKF (n=50)	934.8
Max amplitude $\delta_a = 10^o$	ARMSE UKF (n=50)	9.76
	ARMSE CKF (n=50)	11.66
Max amplitude $\delta_r = 10^o$	ARMSE UKF (n=50)	10.01
	ARMSE CKF (n=50)	25.59

In a nutshell, the UKF outperforms the CKF under strongly non-linear conditions and in environments with excessive noise or large initial errors. This is consistent with results obtained in a number of studies. Matzuka et al., [44] observed reconstructed data obtained for different parameter estimation applications using several Kalman filtering methodologies, amongst these identification techniques was the UKF and CKF. This extensive exercise showed that the UKF and CKF produced equivalent results in most cases, however the CKF failed in a

majority of cases where the UKF succeeded [44]. More specifically, the CKF failed in conditions that are highly non-linear or exhibit large noises. Matzuka et al, [44] applied the UKF and CKF on the Lorenz equations, these equations are highly non-linear and chaotic. When the researchers used UKF and CKF to predict the parameters in the chaotic regime the CKF failed to track the state and increasingly deviated from the true state, whilst the UKF successfully estimated the parameters. This is consistent with the ARMSE observations for applications involving loss of control induced by control surface failure in this study.

6.3 Control Surface Deflection Estimation

The aerodynamic force and moment coefficient equations (2.8) to (2.13) are used to establish how flight path reconstruction results obtained in Sections 6.2.1, 6.2.2 and 6.2.3 can be used to give insight on reasons behind the loss of control or the upset. The reconstructed time history of the following states; u, v, w, ϕ, θ and ψ, and measured data, $p_{measured}$, $q_{measured}$ and $r_{measured}$ are used to solve the aerodynamic equations simultaneously. The aerodynamic coefficients and control surface deflections obtained from this exercise are presented in this section and the likelihood that these can be used to infer the cause of loss of control induced in the GTM T2 UAV simulation discussed.

6.3.1 Jammed rudder control surface

In this section, the MATLAB Simulink GTM T2 UAV model simulated a jammed rudder surface deflection of 10° that resulted in non-linear behaviour. The flight path reconstruction results for this exercise are presented in Section 6.2.1. The lateral aerodynamic equations are used to determine if reconstructed states can be used to adequately determine the control inputs responsible for the aircraft upset. The control inputs are calculated by solving the force and moment coefficients equations simultaneously. Figures 43 and 44 show the force and moment coefficients and the surface deflections responsible for the non-linear simulation response respectively.

The reconstructed states used to predict force and moment coefficients produced adequate aerodynamic coefficient values for both before and after the control upset at $20s$. There is little notable difference between the elevator deflection calculated from the UKF reconstructed states and the true deflection. However, the elevator deflection calculated from the CKF reconstructed states gradually deviates from the true value after the 10° rudder jam is applied. This may be because the CKF has degraded performance in non-linear environments [44]. There is a deviation in the aileron and rudder filter solutions as well, for both filters. The deviation in the rudder deflection solution may be explained by the offset in the reconstructed

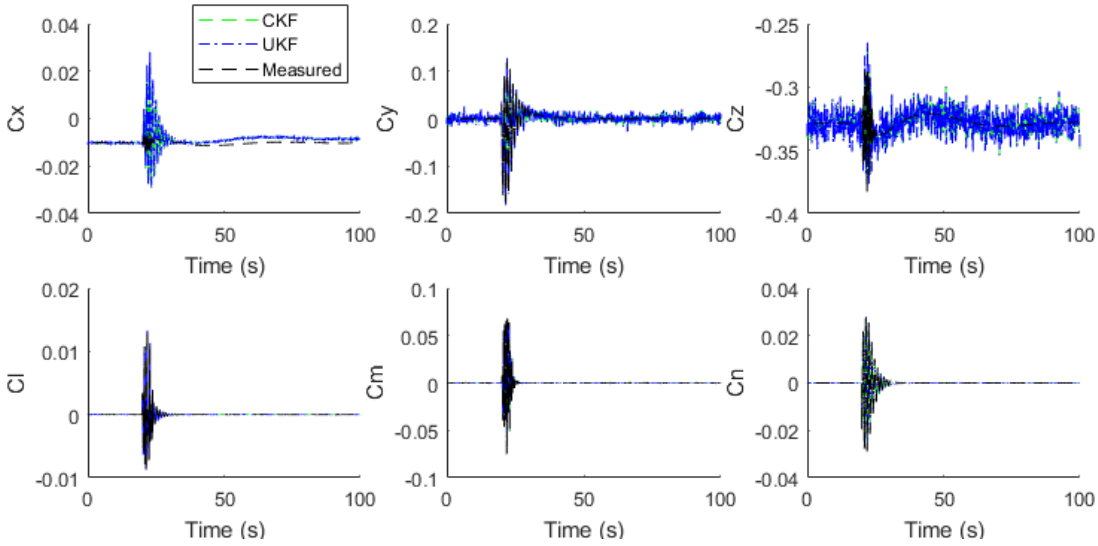

Figure 43: Force and moment coefficients in the body-axes frame for a 10° rudder deflection.

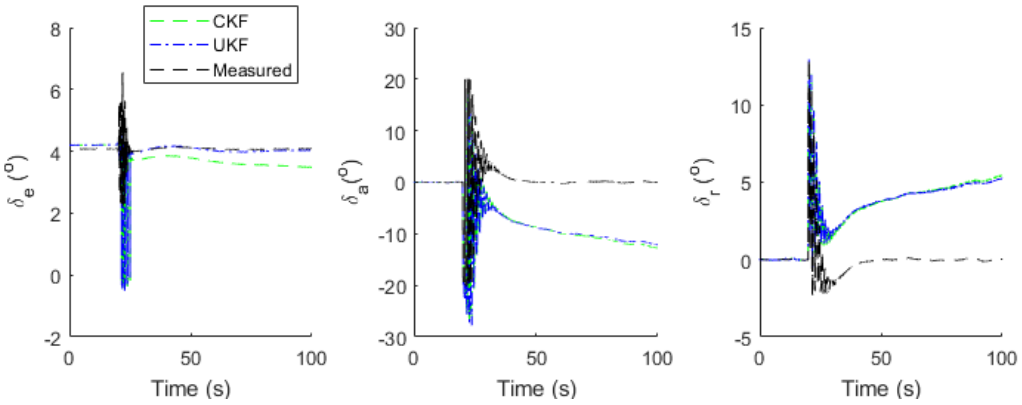

Figure 44: Control inputs for a 10° rudder deflection.

yaw angle, ψ, presented in Figure 34. Whilst the error in the aileron control input value may be because of yaw and roll coupling [81]; given that δ_a and δ_r variables are solved simultaneously, the error in ψ is likely propagated to δ_a. Coupling of yaw and roll motion makes it difficult to distinguish between the aileron and rudder input being the origin of the upset causing loss of control. Coupling of the lateral equations makes roll input values susceptible to errors in the yaw states. All this makes it difficult to establish the reason behind the aircraft loss of control. In contrast, this does not seem to be the same in the case of an aileron upset. Figure 45 shows control deflections calculated from reconstructed states of a GTM T2 UAV experiencing a 10° aileron jam at t= 20s.

A deflection in the aileron control surface does not result in a notable deviation in the rudder deflection, as such any aileron deflection can be clearly identified as the reason behind the upset. The maximum aileron deflection observed in the figure is 10°, this is consistent with the actual applied aileron deflection.

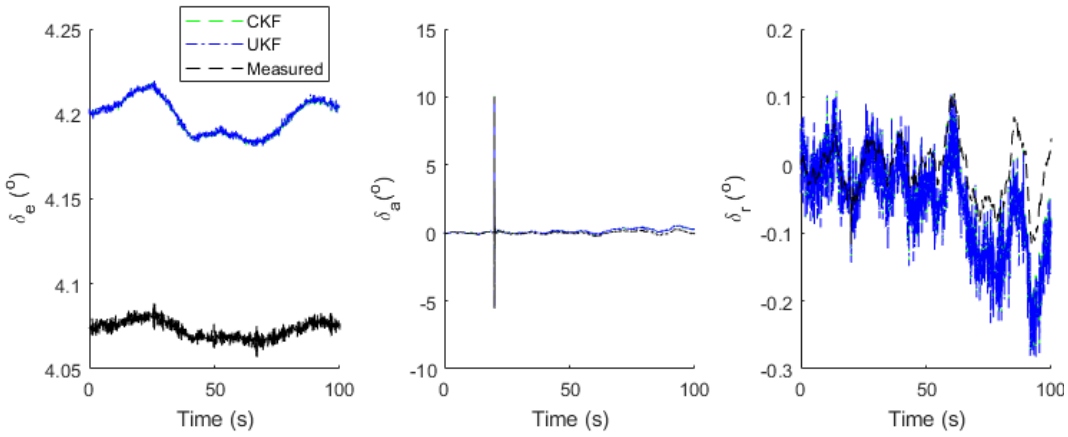

Figure 45: Control inputs for a 10° jammed aileron input.

6.3.2 Elevator control surface hardover

The force and moment coefficients, C_x, C_y, C_z, C_l, C_m and C_n, and the estimated control surface deflections, δ_e, δ_a and δ_r, are calculated by solving aerodynamic coefficient equations simultaneously. These calculations are performed for an elevator hardover of 20° that caused stall and the termination of the simulation. The reconstructed states used for this calculation are presented in Section 6.2.2. Figures 46 and 47 show the aerodynamic coefficients and the reconstructed control inputs for a 20° elevator hardover respectively.

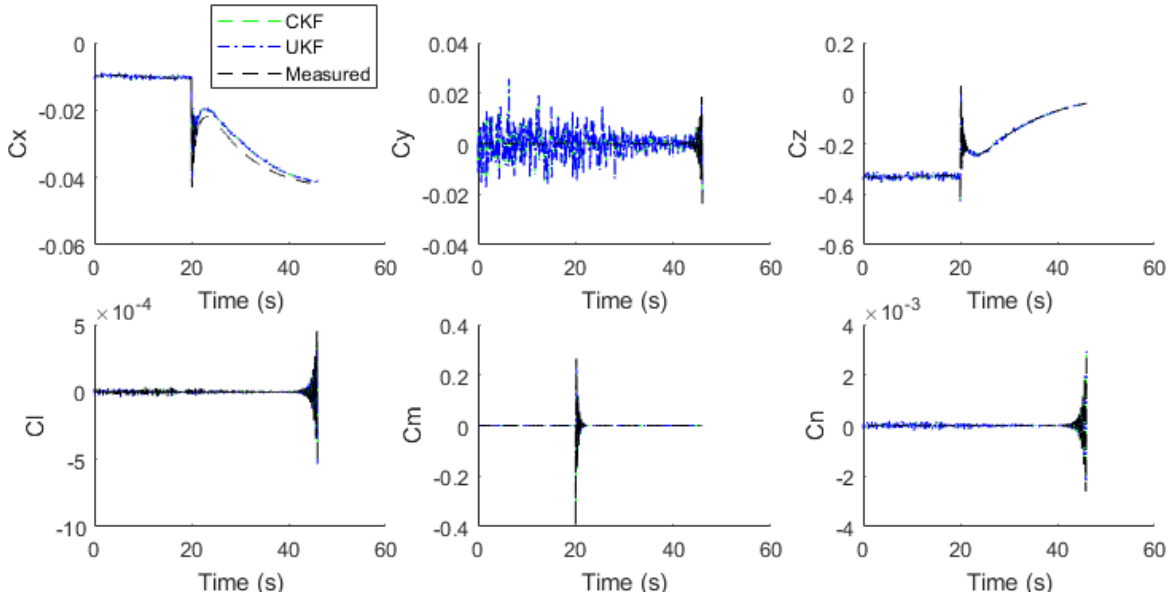

Figure 46: Force and moment coefficients in the body-axes frame for a 20° elevator hardover.

The reconstructed states from both filters sufficiently estimated all the aerodynamic coefficients. The longitudinal aerodynamic coefficients C_x, C_z and C_m show a disturbance at the time t=20s when the 20° elevator hardover is imposed. On the other hand, the lateral

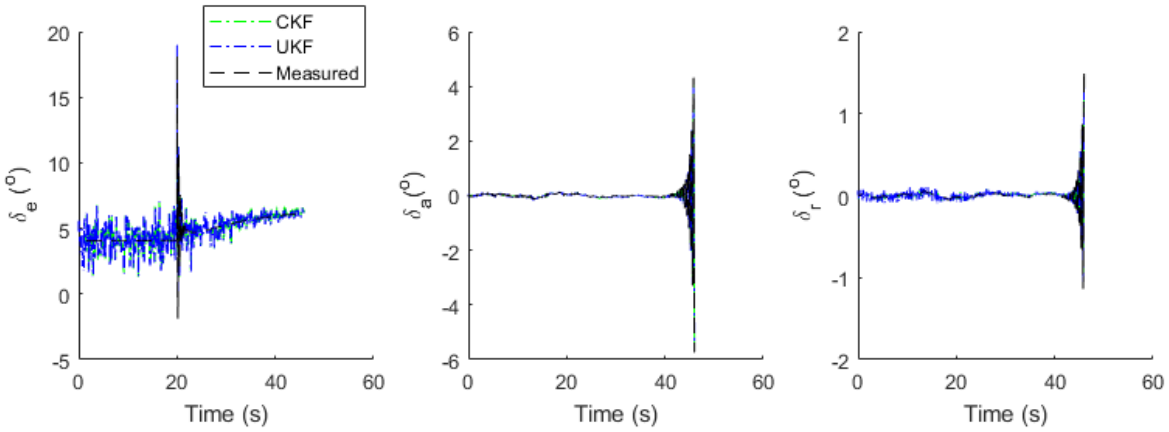

Figure 47: Control inputs for a 20° elevator hardover.

aerodynamic coefficients C_y, C_l and C_n remain constant during this period. This response suggests that the longitudinal control input, δ_e, is behind the stall that causes the termination of the flight. The maximum elevator deflection recorded in Figure 47 is about 20°. The reconstructed states, force and moment coefficients and control deflections make it possible for one to infer that the GTM T2 UAV stall is caused by an elevator hardover.

6.3.3 Rudder control surface float

The aerodynamic coefficients and control inputs for rudder float are calculated using reconstructed states from both filters provided in Section 6.2.3. The force and moment coefficients and control inputs for a rudder float input are presented in Figures 48 and 49 respectively.

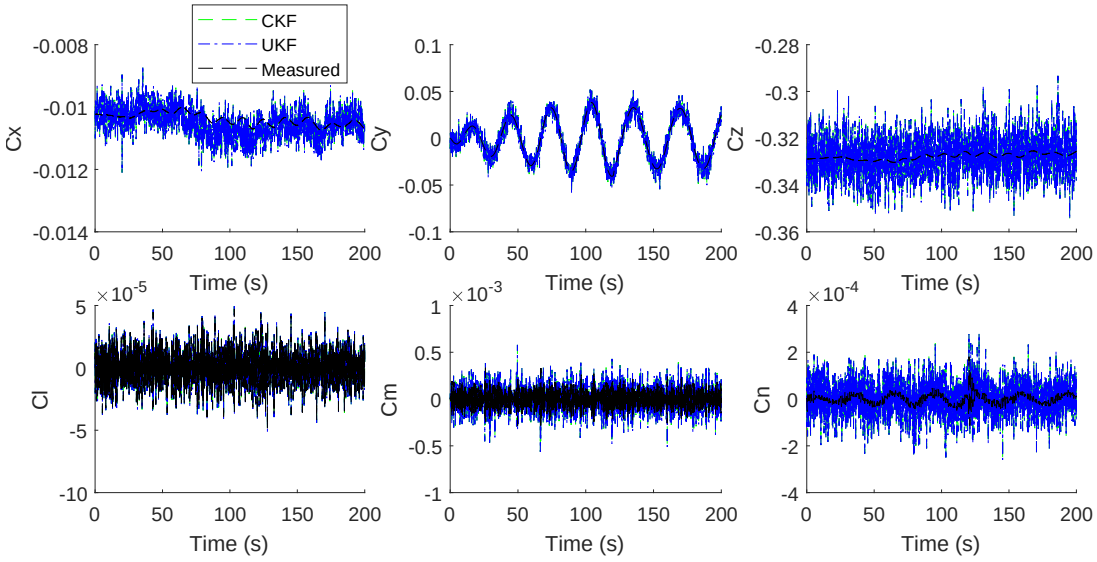

Figure 48: Force and moment aerodynamic coefficients in the body-axes frame for rudder float.

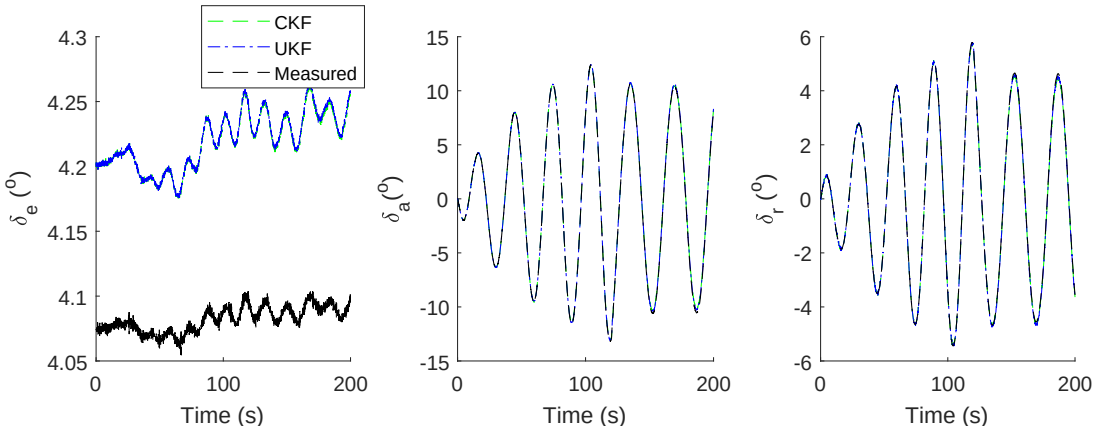

Figure 49: Control inputs for rudder float.

The reconstructed states from both filters adequately determined aerodynamic coefficient values. Solutions from the force and moment coefficients equations sufficiently tracked the δ_e, δ_a and δ_r control inputs. A rudder disturbance caused an upset in the aileron input, resulting from yaw and roll coupling. The C_y and C_n force and moment coefficients responsible for yawing motion show a sinusoidal pattern. When combined with the FPR results, one can infer that the reason behind the LOC is a sinusoidal rudder control input. The difference in performance of the CKF and the UKF is indistinguishable.

7 Conclusions and Recommendations

7.1 Conclusions

The following conclusions are made in this study:

a. A comparison of the ability of the unscented Kalman filter and the cubature Kalman filter to reconstruct the flight path of a UAV experiencing an upset or loss of control caused by sensor and control surface failure was done and the following was observed;

- Induced sensor failure:
  - Sensor noise: Both filters successfully reconstructed the states of a UAV experiencing excessive noise. The UKF and CKF exhibited similar performance at low noise levels, however, the UKF provided better estimations at excessively high noise levels.
  - Sensor bias: The UKF and CKF failed to reconstruct the pitch angle and vertical velocity in the case of a $0.01°.s^{-1}$ sensor bias applied to the pitch rate. The UKF performed slightly better than the CKF in tracking states of a UAV experiencing sensor bias.
  - Sensor blackout: The performance of the UKF was significantly degraded for the u, w, ϕ, and x states in the case of a GPS sensor blackout. It indicates that the CKF outperformed the UKF when there is a reduced number of known states.
- Induced control surface failure:
  - Jammed control surface: There was a notable error in the reconstruction of yaw states in the case of a 10° jammed rudder. Though both filters displayed errors, the errors produced by the CKF were higher than those obtained from the UKF. As a result, the UKF performs better than the CKF in tracking the states of a UAV experiencing LOC caused by a jammed rudder. Similar results were observed for a UAV experiencing 10° jammed aileron and elevator.
  - Control surface hard-over: Both filters sufficiently reconstructed the states of a UAV experiencing a 20° elevator hard-over. The UKF consistently produced significantly better results for all types of control surface hard-over.
  - Control surface float: The difference in filter performance between UKF and CKF in reconstructing states of a UAV experiencing rudder and aileron float was marginal. However, the UKF significantly outperformed the CKF in the case of elevator float.

b. The flight path reconstruction results were used to provide insight on reasons behind the loss of control and the following was determined;

- The reconstructed states obtained from both the UKF and CKF managed to adequately produce all aerodynamic coefficients for a 10° jammed rudder. The UKF successfully tracked the aircraft elevator deflection before and after LOC, whilst elevator deflection obtained using CKF flight path reconstruction results gradually deviated from the true value. Errors in the reconstructed lateral directional states were propagated to the aileron and rudder deflection estimations, making inferring the reason behind LOC difficult. A 10° jammed aileron response showed that it is possible to distinguish between a rudder upset and an aileron disturbance. An aileron disturbance did not result in any rudder response. This was observed for all control surface failure modes. As a result, it is possible to distinguish between rudder and aileron upsets.
- The force and moment aerodynamic coefficients were sufficiently reconstructed, so were all the control surface deflections for 20° elevator hard-over. The maximum elevator deflection estimated was about 20°, recorded at the point of LOC. These results can be used to infer that the elevator deflection is the reason behind the loss of control.
- The control surface deflections calculated using the reconstructed states from both the UKF and CKF tracked the true elevator, aileron and rudder surface deflections for rudder float. The rudder float disturbance resulted in a coupled response in the aileron controls. This response is behind the highly non-linear oscillatory motion exhibited by the UAV, as such in this case, these results can be used to give an indication of the reasons behind the loss of control.

c. Assessing the stability and performance of the parameter identification techniques:

- The unscented Kalman filter provides better estimations at excessive noise levels and in highly non-linear environments such as control surface hard-over, jammed control surfaces and float. The UKF reconstructed states however deviate from the true value in the case of sensor blackout.
- The performance of the cubature Kalman filter degraded as the magnitude of sensor noise increased. This shows that the CKF has poor performance when reconstructing states in the presence of poor measurement data. Furthermore, though the CKF managed to reconstruct the UAV states for induced control surface failure, the CKF diverged in highly non-linear environments for certain estimated process and measurement noise functions, w and v. CKF stability decreases in situations with excessive noise as well as in highly non-linear environments.

7.2 Recommendations

The following recommendations are made for future work:

1. The performance of the CKF and UKF in other failure modes such as structural failure, microbust windshear and loss of effectiveness must be investigated.
2. Further work must be done to explore how sampling time in the sensor data affects the performance of these filters.
3. There are recent publications that have investigated the use of several variations of the CKF and UKF. The performance of these alternate algorithms must be investigated.
4. The use of different single objective or multi-objective algorithms such as genetic algorithms (GA), differential evolution (DE) algorithms, and particle swarm optimisation (PSO) to select the UKF and CKF parameters, initial covariance estimates, as well as the controller gains used to stabilise the UAV in the presence of atmospheric disturbance must be investigated.

Appendices

Appendix 1

Table 22 shows the values of a_n, b_n, c_n, d_n, e_n, f_n used in the calculation of the force and moment coefficients.

Table 22: Trim states used for the model verification process

n	C_x	C_y	C_z	C_l	C_m	C_n
	a_n	b_n	c_n	d_n	e_n	f_n
0	0.0390905	1.0499	0.0261857	0.126318	0.181738	0.202546
1	0.35218	0.254159	5.38662	0.22119	1.10553	0.143331
2	5.36708	0.765433	0.339087	0.255338	15.1134	0.379639
3	23.1537	0.10909	28.0138	0.191268	47.6756	0.205145
4	26.2264	0.553414	23.0418	0.0608527	69.4945	0.937344
5	109.938	1.22326	12.8899	0.730792	308.277	0.00731187
6	2.46995	1.26322	28.2259	2.90179	1.76253	0.45033
7	24.4028	39.4599	62.5918	0.414849	0.920542	0.724553
8	58.4581	0.175591	460.84	0.325859	1.35544	16.4433
9	0.125409		0.445354	6.67529		0.112626
10	0.0857469		0.0972682	125.613		0.000470559
11	0.00961977		0.0347678	0.0247139		
12	0.0811392		0.0811392	0.0193176		
13	0.0405696		0.0135232			
14	0.0033808		0.00067616			
15	0.389796		0.389796			
16	0.064966		0.194898			
17	0.0032483		0.0162415			

References

[1] Żugaj M, Bibik P, Jacewicz M. UAV Aircraft Model for Control System Failures Analysis, *Journal of Theoretical and Applied Mechanics*. 2016; 54(4), pp. 1405-1415.

[2] Williams KW. A Summary of Unmanned Aircraft Accident/ Incident Data: Human factors Implications. Federal Aviation Administration Oklahoma City OK Civil Aeromedical Inst. No. DOT/FAA/AM -04/24. 2004 Dec.

[3] Ingham LA. Considerations for a Roadmap for the Operation of Unmanned Aerial Vehicles (UAV) in South African Airspace, 2008, PhD Thesis, Stellenbosch University, Stellenbosch.

[4] Nesbit PR, Barchyn TE, Hugenholtz CH, Cripps S, Kucharczyk M. Reported UAV Incidents in Canada: Analysis and Potential Solutions. *Journal of Unmanned Vehicle Systems*. 2017, 5(2), pp. 51-61.

[5] Wild G, Murray J, Baxter G. Exploring Civil Drone Accidents and Incidents to Help Prevent Potential Air Disasters. *Aerospace*. 2016, 3(3):22, pp. 1-11.

[6] Roder A, Choo KK, Le-Khac NA. Unmanned aerial vehicle forensic investigation process: Dji phantom 3 drone as a case study. arXiv preprint arXiv:1804.08649. 2018 Apr 23.

[7] McAteer IN, Hannay P, Malik MI, Baig Z. Forensic analysis of a crash-damaged Cheerson Cx-20 auto pathfinder drone. *Journal of Digital Forensics, Security and Law*. 2018, 13(4), pp. 5-19.

[8] Ouellette JA. Flight Dynamics and Maneuver Loads on a Commercial Aircraft with Discrete-Source Damage, 2010, Masters Dissertation, Virginia Polytechnic Institute and State University, Virginia.

[9] Belcastro CM. Loss of Control Prevention and Recovery: Onboard Guidance, Control, and Systems Technologies. In AIAA Guidance, Navigation, and Control Conference. Minneapolis, Minnesota 2012 Aug 13, pp. 4762-4777.

[10] Frink NT, Murphy PC, Atkins HL, Viken SA, Petrilli JL, Gopalarathnam A, Paul RC. Status of Computational Aerodynamic Modelling Tools for Aircraft Loss-of-Control. In AIAA Atmospheric Flight Mechanics Conference. San Diego, California 2016, pp. 1041-1066.

[11] Belcastro CM, Foster JV, Shah GH, Gregory IM, Cox DE, Crider DA, Groff L, Newman RL, and Klyde DH. Aircraft Loss of Control Problem Analysis and Research Toward a Holistic Solution, *Journal of Guidance, Control, and Dynamics*. 2017, 40(4), pp. 733-775.

[12] Rafi M, Steck JE, Chakravarthy A, Yucelen T. Approaches to Real-Time Predictive Estimation of Loss-of-Control Events and Boundaries on Transport Aircraft. In AIAA Guidance, Navigation, and Control Conference. Grapevine, Texas 2017, pp. 1716-1741.

[13] Mulder JA, Chu QP, Sridhar JK, Breeman JH, Leban M. Non-linear Aircraft Flight Path Reconstruction: Review and New Advances, *Progress in Aerospace Sciences*. 1999, 33(7), pp. 673-726.

[14] Qing W, Kaiyuan W, Tianjiao Z, Yi'nan K., Weiqi Q. Aerodynamic Modelling and Parameter Estimation from QAR Data of an Airplane Approaching a High-Altitude Airport. *Chinese Journal of Aeronautics*. 2012, 25(3), pp. 361-371.

[15] Pispitsos SP, Napolitano MR, Seanor B. Developing Tools for Reconstructing Control Signals for Crash Investigations. *Aircraft Design*. 2000, 3(3), pp. 175-203.

[16] Langelaan JW. State Estimation for Autonomous Flight in Cluttered Environments, 2006, PhD Thesis, Stanford University, Stanford.

[17] Kada B, Munawar K, Shaikh MS, Hussaini MA, Al-Saggaf UM. UAV Attitude Estimation Using Non-linear Filtering and Low-Cost MEMS Sensors. International Federation of Automatic Control Online Papers. 2016, 49(21), pp. 521-528.

[18] Caliskan F, Hajiyev C. Active Fault-Tolerant Control of UAV Dynamics Against Sensor-Actuator Failures. *Journal of Aerospace Engineering*. 2016, 29(4), pp. 1-17.

[19] Vepa R. *Non-linear Control of Robots and Unmanned Aerial Vehicles: An Integrated Approach*. Boca Raton, CRC Press. 2017 pp. 458.

[20] de Oliveira Maciel BC, Sandoval Góes LC, Hemerly EM, Salis N. Flight Path Reconstruction and Parameter Estimation Using Output-Error Method. *Shock and Vibration*. 2006, 13(4,5), pp. 379-392.

[21] Vissiere D, Bristeau PJ, Martin AP, Petit N. Experimental Autonomous Flight of a Small-scaled Helicopter Using Accurate Dynamics Model and Low-Cost Sensors. IFAC Proceedings Volumes. 2008, 41(2), pp. 14642-14650.

[22] Opromolla R. Magnetometer Calibration for Small Unmanned Aerial Vehicles Using Cooperative Flight Data. Sensors. 2020, 20(2), pp. 538.

[23] Yang Y, Zhou J, Loffeld O. Quaternion-based Kalman Filtering on INS/GPS. In Information Fusion (FUSION) International Conference. Singapore, 2012, pp. 511-518.

[24] Eulrich BJ, Rynaski EG. Identification of Non-Linear and Control Parameters at High Angles of Attack. In Parameter Estimation Techniques and Applications in Aircraft Flight Testing: A Symposium Held at Flight Research Centre, Edwards, California. 1974, pp. 189-204.

[25] Padayachee K. Aerodynamic Parameter Identification for an Unmanned Aerial Vehicle, 2016, Masters Dissertation, University of the Witwatersrand, Johannesburg.

[26] Borup KT, Fossen TI, Johansen TA, A Nonlinear Model-Based Wind Velocity Observer for Unmanned Aerial Vehicles. International Federation of Automatic Control Papers Online. 2016, 49(18), pp. 276-283.

[27] Belcastro CM, Newman RL, Crider DA, Kylde DH, Foster JV, Groff L, Aircraft Loss of Control: Problem Analysis for the Development and Validation of Technology Solutions. In AIAA Guidance, Navigation, and Control Conference. San Diego, California, USA 2016, pp. 0092-00104.

[28] Mora-Camio F, Cuncha SS, Doncescu A. Aircraft Flight Management with Actuator Major Failure. In Control and Decision Conference. China 2011, pp. 4311-4316.

[29] Wilborn J, Foster J. Defining commercial transport loss-of-control: A quantitative approach. In AIAA Atmospheric Flight Mechanics Conference and Exhibit. Providence, Rhode Island 2004 Aug 16, pp. 4811-4822.

[30] Kwatny HG, Dongmo JE, Chang BC, Bajpai G, Yasar M, Belcastro C. Nonlinear Analysis of Aircraft Loss of Control. *Journal of Guidance, Control, and Dynamics*. 2012, 36(1), pp. 149-162.

[31] Murch A, Foster J. Recent NASA Research on Aerodynamic Modeling of Post-Stall and Spin Dynamics of Large Transport Airplanes. In 45th AIAA Aerospace Sciences Meeting and Exhibit. Reno, Nevada 2007 Jan 1, pp. 463-483.

[32] Chang BC, Kwatny H, Belcastro C, Belcastro C. Aircraft Loss-of-Control Accident Prevention: Switching Control of the GTM Aircraft with Elevator Jam Failures. In AIAA Guidance, Navigation and Control Conference and Exhibit. Honolulu, Hawaii 2008, pp. 6507-6522.

[33] Jordan T, Langford W, Belcastro C, Foster J, Shah G, Howland G, Kidd R. Development of a Dynamically Scaled Generic Transport Model Testbed for Flight Research Experiments. NASA Document ID 20040085988, 2004.

[34] Ma L, Zhang Y. Fault Detection and Diagnosis for GTM UAV with Dual Unscented Kalman Filter. In AIAA Guidance, Navigation, and Control Conference. Toronto 2010, pp. 7884-7896.

[35] Péni T, Vanek B, Szabó Z, Gáspár P, Bokor J. Supervisory Fault Tolerant Control of the GTM UAV using LPV Methods. *International Journal of Applied Mathematics and Computer Science*. 2015, 25 (1), pp. 117-131.

[36] Gill SJ, Lowenberg MH, Neild SA, Krauskopf B, Puyou G, Coetzee E. Upset Dynamics of an Airliner Model: a Nonlinear Bifurcation Analysis. *Journal of Aircraft*. 2013 Aug 2, 50(6), pp. 1832-1842.

[37] Chauhan RK, Singh S. Review of Aerodynamic Parameter Estimation Techniques. In Infocom Technologies and Unmanned Systems (Trends and Future Directions)(ICTUS) International Conference. United Arab Emirates 2017 Dec 18, pp. 864-869.

[38] Hemerly EM, Mendoça CB. Equation Error Method for Aircraft Parameter Estimation. In 19th International Mechanical Engineering Conference. Brasilia-DF, Brazil 2007 Nov 5, pp. 336-341.

[39] Jonkers HL. Application of the Kalman Filter to Flight Path Reconstruction from Flight Data Including Estimation of Instrumental Bias Error Corrections, 1976, PhD Thesis, Delft University of Technology, Netherlands.

[40] Chowdhary G, Jategaonkar R. Aerodynamic Parameter Estimation from Flight Data Applying Extended and Unscented Kalman Filter. *Aerospace Science Technology*. 2010, 14(2), pp. 106-117.

[41] Rigatos GG. Non-linear Kalman Filters and Particle Filters for Integrated Navigation of Unmanned Aerial Vehicles, *Robotics and Autonomous Systems*. 2012, 60(7), pp. 987-995.

[42] Arasaratnam I. Cubature Kalman Filtering, Theory and Applications, 2009, PhD Thesis, McMaster University, Canada.

[43] Teixeira BOS, Tôrres LAB, Oliveira PHIA, Aguirre LA. Flight Path Reconstruction Using the Unscented Kalman Filter Algorithm. In International Congress of Mechanical Engineering. Ouro Preto 2005 Nov 6, pp. 610-618.

[44] Matzuka B, Aoi M, Attarian A, Tran HT. Nonlinear Filtering Methodologies for Parameter Estimation. North Carolina State University. Center for Research in Scientific Computation, 2012.

[45] Lord FM. Maximum Likelihood and Bayesian Parameter Estimation in Item Response Theory. ETS Research Report Series. RR-84-30-ONR, 1984(2).

[46] Hodge WF, Bryant WH. Monte Carlo Analysis of Inaccuracies in Estimated Aircraft Parameters Caused by Unmodeled Flight Instrumentation Errors. NASA TN D-7712, 1975.

[47] Arruda M. Dynamic Inverse Resilient Control for Damage Asymmetric Aircraft: Modelling and Simulation, 2009, Masters Dissertation, Graduate School of Wichita State University, Kansas.

[48] Nguyen N, Krishnakumar K, Kaneshige J, Nespeca P. Dynamics and Adaptive Control of Stability Recovery of Damaged Asymmetric Aircraft. In AIAA Guidance, Navigation, and Control Conference and Exhibit. Keystone, Colorado, 2006, pp. 6049-6073.

[49] Cunningham K, Foster J, Murch A, Morelli E. Practical Application of a Subscale Transport Aircraft for Flight Research in Control Upset and Failure Conditions. In AIAA Atmospheric Flight Mechanics Conference and Exhibit. Honolulu, Hawaii 2008 Aug 18, pp. 6200-6214.

[50] Hu X, Chen X, Parks GT, Yao W. Review of Improved Monte Carlo Methods in Uncertainty Based Design Optimisation for Aerospace Vehicles, *Progress in Aerospace Sciences.* 2016, 86, pp. 20-27.

[51] Särkkä S, Solin A. On Continuous-Discrete Cubature Kalman Filtering. International Federation of Automatic Control Proceedings. 2012, 45 (16), pp. 1221-1226.

[52] Kulikov GY, Kulikov MV. Do the Cubature and Unscented Kalman Filtering Methods Outperform Always the Extended Kalman Filter? International Federation of Automatic Control Online Papers. 2017, 50(1), pp. 3762-3769.

[53] Etkin B, Reid LD. *Dynamics of Flight: Stability and Control.* 3rd ed. New York: Wiley; 1996 Jan, pp. 104

[54] Panday A. NDI-Based Neurocontroller for Unmanned Combat Aerial Vehicles during Aerial Refuelling, 2010, Masters Dissertation, University of the Witwatersrand, Johannesburg.

[55] Vepa R. *Flight Dynamics, Simulation, and Control: For Rigid and Flexible Aircraft.* New York CRC Press; 2014 Aug 18, pp. 135.

[56] Brossard M, Condomines JP, Bonnabel S. Tightly Coupled Navigation and Wind estimation for Mini UAVs. In AIAA Guidance, Navigation, and Control Conference. Kissimmee, Florida 2018, pp. 1843-1862.

[57] Rauw MO. FDC 1.2-A Simulink Toolbox for Flight Dynamics and Control Analysis. Zeist, The Netherlands. 2001 May 10; 1(99):7.

[58] Hakim TM, Arifianto O. Implementation of Dryden Continuous Turbulence Model into Simulink for LSA-02 Flight Test Simulation. In Journal of Physics: Conference Series. Medan, Indonesia 2018 Apr, Vol. 1005, No. 1, pp. 12017-12027. IOP Publishing.

[59] Gage S. Creating a Unified Graphical Wind Turbulence Model from Multiple Specifications. In AIAA Modelling and Simulation Technologies Conference and Exhibit. Austin, Texas 2003, pp. 5529 - 5539.

[60] Grauer JA, Morelli EA. Dependence of Dynamic Modelling Accuracy on Sensor Measurements, Mass Properties, and Aircraft Geometry. NASA Document ID 2014003885, 2013

[61] Kalantar-Zaden K. Sensors: An Introductory Course. Springer Science and Business Media New York; 2013 March.

[62] Klein V, Morelli EA. *Aircraft System Identification: Theory and Practice.* Reston, VA: American Institute of Aeronautics and Astronautics; 2006 Aug.

[63] Rhudy M, Gu Y, Gross J, Gururajan S, Napolitano MR. Sensitivity Analysis of Extended and Unscented Kalman Filters for Attitude Estimation. *Journal of Aerospace Information Systems.* 2013 Mar, 10(3), pp. 131-143.

[64] Julier SJ, Uhlmann JK. New Extension of the Kalman Filter to Nonlinear Systems. In Signal Processing, Sensor Fusion, and Target Recognition VI. International Society for Optics and Photonics. 1997 Jul 28, Vol. 3068, pp. 182-194.

[65] Straka O, Duník J, Šimandl M. Unscented Kalman Filter with Controlled Adaptation. IFAC Proceedings Volumes. 2012 Jul 1, 45(16), pp. 906-911.

[66] Rhudy MB, Salguero RA, Holappa K. A Kalman Filtering Tutorial For Undergraduate Students. International Journal of Computer Science and Engineering Survey (IJCSES). 2017, 8(1), pp. 1-18

[67] Arasaratnam I, Haykin S. Cubature Kalman Filtering: A Powerful New Tool for Aerospace Applications. International Radar Conference 2009. Bordeaux, France 2009 Oct.

[68] Wang D, Lv H, Wu J. Augmented Cubature Kalman filter for Nonlinear RTK/MIMU Integrated Navigation with Non-additive Noise. *Measurement.* 2017 Feb 1, 97, pp. 111-125.

[69] Arasaratnam I, Haykin S, Hurd TR. Cubature Kalman Filtering for Continuous-Discrete Systems: Theory and Simulations. IEEE Transactions on Signal Processing. 2010 Oct, 58(10), pp. 4977-93.

[70] Jia B, Xin M, Cheng Y. High-degree Cubature Kalman Filter. *Automatica.* 2013 Feb 1, 49(2), pp. 510-518.

[71] Sinha NK, Ananthkrishnan N. Advanced Flight Dynamics with Elements of Flight Control. CRC Press Great Britain; 2017 Jun 27.

[72] Ledolter J, Robert V. *Applied Statistics for Engineers.* Macmillan Publishing Company New York. 1992.

[73] Sun Y, Chen Q. Joint Estimation of States and Parameters of Vehicle Model Using Cubature Kalman Filter. In 2016 IEEE International Conference on Systems, Man, and Cybernetics (SMC). Budapest 2016 October 9, pp. 977-982. IEEE.

[74] Wei Z, Wei W, Gannan Y. Improved Cubature Kalman Filtering for Tightly Coupled GPS/SINS Integrated Navigation System. In 2016 IEEE International Conference on Mechatronics and Automation. Harbin, China 2016 August 7, pp. 983-987. IEEE.

[75] Zarchan P, Musoff H. *Fundamentals of Kalman Filtering: A Practical Approach*. 2nd ed. American Insitute of Aeronautics and Astronautics Reston, Virginia. 2013 pp. 183-303.

[76] Yang F, Luo Y, Zheng L. Double-Layer Cubature Kalman Filter for Nonlinear Estimation. *Sensors*. 2019 Jan, 19(5), pp. 986-1001.

[77] Klavins E, Zagursky V. Unmanned Aerial Vehicle Movement Trajectory Detection in Open Environment. *Procedia Computer Science*. 2017 Jan 1, 104, pp. 400-407.

[78] Kooshkbaghi M, Marquez HJ. Event-Triggered State Estimation of High Dimensional Nonlinear Systems With Highly Nonlinear State Space Model Using Cubature Kalman Filter. In 2019 IEEE Canadian Conference of Electrical and Computer Engineering (CCECE). Edmonton, AB, Canada 2019 May 5, pp. 1-4. IEEE.

[79] Zhao X, Li J, Yan X, Ji S. Robust Adaptive Cubature Kalman Filter and its Application to Ultra-Tightly Coupled SINS/GPS Navigation System. *Sensors*. 2018 Jul, 18(7), pp. 2352-2371.

[80] Zhang B, Chu H, Sun T, Jia H, Guo L, Zhang Y. Error Prediction for SINS/GPS after GPS Outage Based on Hybrid KF-UKF. *Mathematical Problems in Engineering*. 2015, Online Article ID 239426.

[81] Stengel RF. Flight Dynamics. Princeton University Press New Jersey; 2015 Jan 27.